Earthquake Ground Motion Estimation

Daniel R. H. O'Connell and Jon P. Ake

U.S. Bureau of Reclamation, P.O. Box 25007 D-8330, Denver, CO 80225, USA; geomagic@seismo.usbr.gov

INTRODUCTION

A primary goal of seismology is to estimate how the ground moves in response to an earthquake at specific locations of interest. When a building is subjected to ground shaking from an earthquake, elastic waves travel through the structure and the building begins to vibrate at various frequencies characteristic of the stiffness and shape of the building. Earthquakes generate ground motions over a wide range of frequencies, from static displacements to tens of cycles per second [Hertz (Hz)]. Most structures have resonant vibration frequencies in the 0.1 Hz to 10 Hz range. A structure is most sensitive to ground motions with frequencies near its natural resonant frequency. Damage to a building thus depends on its properties and the character of the earthquake ground motions, such as peak acceleration and velocity, duration, frequency content, kinetic energy, phasing, and spatial coherence. Realistic ground motion time histories are needed for nonlinear dynamic analysis of structures to engineer earthquake-resistant buildings and critical structures, such as dams, bridges, and lifelines.

Ground motion estimation is predicated on the availability of detailed geological and geophysical information about locations, geometries, and rupture characteristics of earthquake faults. Such information is often not readily available. One most recognize that uncertainties about tectonics and the location and activity rates of faults is the dominant contribution to uncertainty in ground motion estimation. Lettis et al. (1997) showed that intraplate blind thrust earthquakes with moment magnitudes (**M**) up to 7 have occurred in intraplate regions and often there was no direct surface evidence to suggest the existence of the buried faults. Geodetic measurements of regional deformation rates provide some indication of the likely rate of earthquakes occurrence in a region, but without information about where that deformation localizes into fault displacement, ground motion estimation uncertainties in such a region are still large. It is important to recognize that the locations and geometries of the faults associated with the 1983 **M** 6.4 Coalinga, 1986 **M** 6.0 Whittier Narrows, 1989 **M** 6.6 Sierra Madre, 1989 **M** 7.0 Loma Prieta, 1992 **M** 7.3 Landers, 1994 **M** 6.7 Northridge, 1999 **M** 7.6 Chi-Chi Taiwan, and 2001 **M** 7.7 Bhuj India earthquakes were not know prior to the occurrence of these earthquakes.

Strong ground motion estimation is a relatively new science. Virtually every new **M** > 6 earthquake in the past 25 years that provided new strong ground motion recordings produced a paradigm shift in strong motion seismology. The 1979 **M** 6.9 Imperial Valley, California, earthquake showed that rupture velocities could exceed shear-wave velocities over a significant portion of a fault, and produced a peak vertical acceleration > 1500 cm/s^2 (Spudich and Cranswick, 1984; Archuleta; 1984). The 1983 **M** 6.5 Coalinga, California, earthquake revealed a new class of seismic sources, blind thrust faults (Stein and. Ekström, 1992). The 1985 **M** 6.9 Nahanni earthquake produced horizontal accelerations of 1200 cm/s^2 and a peak vertical

acceleration > 2000 cm/s^2 (Weichert et al., 1986). The 1989 **M** 7.0 Loma Prieta, California, earthquake occurred on an unidentified steeply-dipping fault adjacent to the San Andreas fault, with reverse-slip on half of the fault (Hanks and Krawinkler, 1991), and produced significant damage > 100 km away related to critical reflections of shear-waves of the Moho (Somerville and Yoshimura, 1990; Catchings and Kohler, 1996). The 1992 **M** 7.0 Petrolia, California, earthquake produced peak horizontal accelerations > 1400 cm/s^2 (Oglesby and Archuleta, 1997). The 1992 **M** 7.3 Landers, California, earthquake demonstrated that multi-segment fault rupture could occur on fault segments with substantially different orientations that are separated by several km (Li et al., 1994). The 1994 **M** 6.7 Northridge, California, earthquake produced a world-record peak horizontal velocity (> 180 cm/s) associated with rupture directivity (O'Connell, 1999a), widespread nonlinear soil responses (Field et al., 1997; Cultera et al., 1999), and resulted in substantial revision of existing ground motion-attenuation relationships (Abrahamson and Shedlock, 1997). The 1995 **M** 6.9 Hyogo-ken Nanbu (Kobe) earthquake revealed that basin-edge generated waves can strongly amplify strong ground motions (Kawase, 1996; Pitarka et al., 1998) and provided ground motion recordings demonstrating time-dependent nonlinear soil responses that amplified and extended the durations of strong ground motions (Archuleta et al., 2000) The 1999 **M** > 7.3 Turkey earthquakes produced asymmetric rupture velocities, including rupture velocities ~40% faster than shear-wave velocities, which may be associated with a strong velocity contrast across the faults (Bouchon et al., 2001). The 1999 **M** 7.6 Chi-Chi, Taiwan, earthquake produced a world-record peak velocity > 300 cm/s with unusually low peak accelerations (Shin et al., 2000). The 2001 **M** 7.7 Bhuj India demonstrated that **M** > 7.5 blind thrust earthquakes can occur in intraplate regions. This progressive sequence of ground motion surprises suggest that the current state of knowledge in strong motion seismology is probably not adequate to make unequivocal strong ground motion predictions. However, with these caveats in mind, strong ground motion estimation has substantial value in developing estimates of seismic hazards and reducing risks associated with earthquakes and engineered structures.

In this paper we illustrate some of the uncertainties in ground motion estimation and discuss future directions in areas of investigation related to strong motion estimation. Most ground motion observations are recorded at distances > 30 km from faults, simply because near-fault regions comprise only a small area relative to total area that is typically subjected to strong ground shaking, which can extend several hundred kilometers from earthquake faults. Consequently, ground motion estimation becomes progressively less difficult and uncertain as sites are located at increasing distances from faults because we have more ground motion experience and ground motion physics uncertainties are reduced at sites located several rupture dimensions removed from faults. In this paper, we focus primarily on the ground motion estimation problem close to faults. The largest peak ground motions, which most substantially stress engineered structures, generally occur with several tens of kilometers of earthquake faults.

GROUND MOTION ESTIMATES BASED ON EMPIRICAL OBSERVATIONS

Ground motion observations are the result of a long history of instrument development and deployment, instigated primarily by earthquake engineers, to acquire data to develop an empirical foundation to understand and predict earthquake ground motions for use in the design of engineered structures. Strong motion instruments usually produce time histories of ground acceleration that can be post-processed to estimate ground velocities and displacements. A

particularly useful derived quantity for engineering analyses are response spectra which are the maximum amplitudes of modestly damped resonant responses of single-degree-of-freedom oscillators (an idealization of simple building responses) to a particular ground motion time history as a function of natural period or natural frequency. While peak accelerations are always of concern for engineering analyses, peak ground velocity is now recognized as a better indicator of damage potential for large structures than is peak ground acceleration (EERI, 1994). Engineering analyses often consist of linear approaches to determine if structures reach the linear strength limits. Ground motion estimation quantities required for linear analyses are peak accelerations and velocities and associated response spectra. Nonlinear engineering analyses require estimates of acceleration time histories. The discussion presented in this section focuses on empirical ground motion parameter estimation methods. Ground motion estimation methods required for nonlinear engineering analyses are presented in subsequent sections.

Historically the estimation of ground motion parameters such as peak acceleration and velocity, response spectral ordinates, and duration has been based on regression relationships developed using strong motion observations. These techniques are still widely used in conventional engineering practice. In their simplest form, these empirical ground motion models predict peak ground motions using amplitude-attenuation models. In general, observed ground motion amplitudes increase with increasing magnitude and decrease with increasing distance from the earthquake fault. These models relate specific ground motion parameters to earthquake magnitude, reduction (attenuation) of ground motion amplitudes with increasing distance from the fault (geometric spreading), and local site characteristics using site classification schemes. Recent attenuation models account for these ground motion factors using the general form:

$$lnY = A_1 + A_2 \cdot \mathbf{M} + A_3 \cdot (\mathbf{M}_{max} - \mathbf{M})^{A_4} + A_5 \cdot ln\{r + A_6 \cdot \exp(A_7 \cdot \mathbf{M})\} + A_8 \cdot r + F^{source} + F^{site} \quad (1)$$

and

$$\sigma_{lnY} = A_9 \quad (2)$$

where Y is the ground motion parameter of interest (peak acceleration, velocity, response spectral ordinate, etc.), **M** is magnitude, r is a distance measure, the $F^{[source,\ site]}$ are indicator variables of site and source type, and the A_i are coefficients to be determined by the regression. The σ_{lnY} term represents the estimate of the standard deviation in the parameter Y at the magnitude and distance of interest.

Moment magnitude has been adopted as the most appropriate measure of earthquake size since it is directly related to the seismic moment of the earthquake (average slip times fault area). Virtually all of the attenuation models currently in use employ moment magnitude as the measure of earthquake size. To first order, lnY is directly proportional to magnitude ($lnY \propto A_2\mathbf{M}$). However, recent relationships all suggest a magnitude "saturation" effect. Specifically, the ground motions increase more slowly with magnitude for larger magnitudes. Most researchers also include a second, higher order, period dependent term to address this observation (the $(\mathbf{M}_{max} - \mathbf{M})^n$ term in equation 1).

The source to site distance measure, *r*, has been defined in a variety of ways by different researchers (Abrahamson and Shedlock, 1997). Early methods which used epicentral distance as a measure have been superseded by those which characterize distance using closest distance to the seismogenic rupture surface (Campbell, 1997), closest distance to the rupture surface (Abrahamson and Silva, 1997) or closest distance to the vertical projection of the rupture to the ground surface (Boore et al., 1997). At distances greater than ~25 km and for most cases, the results predicted by the widely cited relationships are generally comparable (Figure 1a). However, for sites close to the fault surface, the results can vary widely due to the ambiguity in the distance measure and potential rupture directivity effects (Somerville, 1998). As with magnitude effects, there appears to be a distance saturation effect (as shown in Figure 1a), where the slope of the attenuation function decreases for small distances, especially for high frequencies. This observation reflects the fact the earthquake source has finite size and is usually accommodated by a magnitude dependent slope to the log-distance term (a magnitude dependent effective distance of $r + A_6 \cdot e^{A_7 \cdot M}$ in (1) for example) (Idriss, 1993; Abrahamson and Silva, 1997). Anelastic attenuation along the travel path is modeled by a term similar to $A_8 r$ in equation 1.

Site categories are based on either geological criteria (deep soft soil vs. rock for example) or by estimates of average shear wave velocity (usually over the first 30 m, $V_S{}^{30}$). Site classification based on shear wave velocity is generally preferred as it is a quantitative, objective measure and characterizes the site properties in a way that can be related to physical modeling. The site factor attempts to reflect the observation that for small to moderate ground motion levels, all other factors being equal, the motions observed at soil sites are larger than those at rock sites. However, it is becoming more apparent that somewhat deeper geological structures such as laterally varying velocities and sub-basins may significantly affect observed ground motions. (Graves et al., 1998; Stephenson et al., 2000; Boore et al., 1997). This is particularly true for longer period motions (>0.5 sec). The upper 30 m has the most significant effect on the higher frequency ground motions (periods < ~0.4 sec).

Over the past decade the number of strong motion recordings available has increased substantially, resulting in the development of new and more refined attenuation models. In addition to magnitude, distance, and site type, recent attenuation models have attempted to incorporate the influence of regional crustal attenuation (Central and Eastern United States vs. Western United States for example), type of faulting (strike-slip, normal or thrust) and tectonic setting (shallow crustal vs. shallow plate interface and deep intra-plate events). Recent empirical models have also been augmented to include factors that attempt to account for high-frequency hanging wall-footwall geometric considerations (Abrahamson and Silva, 1997) and longer periods (> 0.6 s) near-fault directivity effects (Somerville et al., 1997), the effect of critical Moho reflections and crustal waveguide effects (Somerville et al., 1994; Boore et el., 1997), and the distance dependent transition from body wave dominated attenuation ($1/r$) to surface wave dominated attenuation ($1/\sqrt{r}$) (Abrahamson and Silva, 1997).

The intrinsic variability in earthquake ground motions between sites located < 1 km apart and between ground motions produced at the same site by different earthquakes has long been recognized. Recent research into the origins of this variability may allow a more appropriate characterization of the uncertainty in the estimation of ground motions for engineering

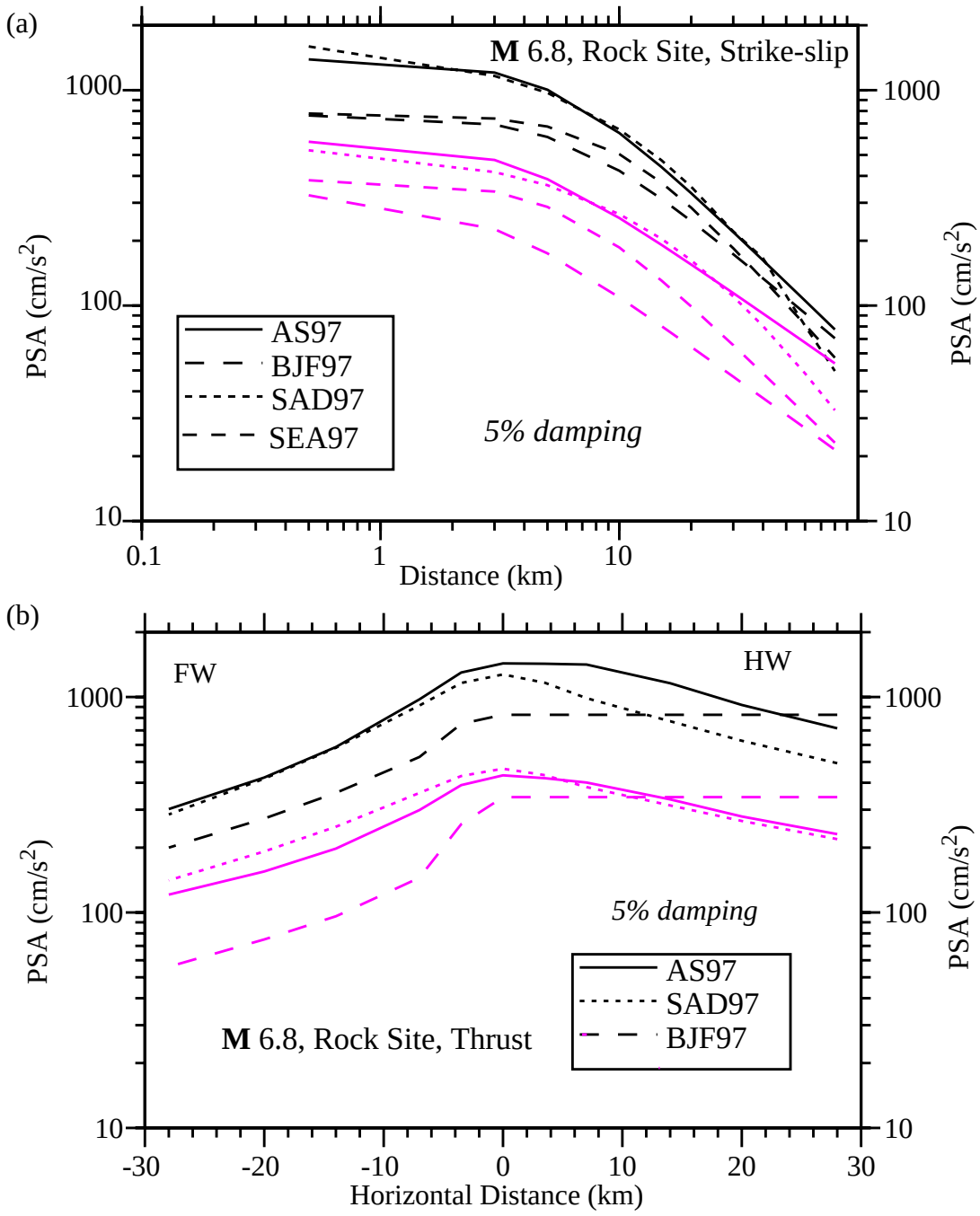

Figure 1. Comparison of pseudo-acceleration response spectral (PSA) attenuation functions of Abrahamson and Silva (1997), AS97, Boore et al. (1997), BJF97, Sadigh et al. (1997), SAD97, , and Spudich et al. (1997), SEA97, for **M** 6.8, vertical strike-slip faulting scenario for rock site conditions (a). Median results for 0.1 sec acceleration spectral response shown in *black*, and for 1.0 sec response in *magenta*. Notice the period-independent, distance saturation effect for source-site distances less than ~10 km. Comparison of PSA attenuation functions from AS97, BJF97, and SAD97 for **M** 6.8, 30-degree dipping concealed thrust scenario. Fault dips to the right and upper tip of fault is 4 km deep at zero distance on the *x* axis (b). Median results for 0.1 sec acceleration spectral response shown in *black*, and 1.0 sec response in *magenta*. Notice difference in hanging wall effect between AS97 and SAD97 for the two spectral periods in (b).

applications. Abrahamson and Youngs (1992) have applied the random effects model to the strong motion data base to separately quantify two sources of variability: the variation in the average ground motions from one earthquake to the next, and the variability in ground motions from one site to another at the same distance from a given earthquake. This is similar to the two-stage regression procedure of Joyner and Boore (1988; 1993). In general, it has been noted that the average ground motions vary little from earthquake to earthquake compared with the variability from one location to another at the same distance from a given earthquake.This variability is inferred to be a function of the earthquake source process, wave propagation through the crust between source and site, and the strongly heterogeneous velocity and geological structure near the earth's surface. In probabilistic seismic hazard analyses, the σ_{lnY} term is used to address the aleatory (inherent natural random variability in the observations) component of uncertainty. Epistemic (modeling) uncertainty is usually addressed by incorporating the results from several attenuation functions.

For some situations and regions there is still a severe shortage of available strong ground motion data however (the eastern United States for example). There are relatively few strong motion recordings from sites located within 10 km of faults and the available ground motion recordings near faults indicate that extreme peak ground motions are possible (Heaton et al., 1995). There are no strong motion recordings of normal faulting earthquakes with **M** > 6 for distances < 10 km from the fault. To compensate for this shortage, a number of researchers have chosen to augment the available empirical data by using theoretically based ground motion models that incorporate specific source, path and site conditions. Synthetic seismograms developed using these procedures can then be used to complement existing empirical recordings.

Somerville et al. (1997) developed modifications to acceleration attenuation relationships to account for the amplitude effects of directivity for periods of 0.6 s and longer. They use the cosine of the angle, θ, between a site and the fault surface to develop amplitude adjustments as a function of θ. In contrast, the "hanging wall" directivity correction of Abrahamson and Silva (1997) attains maximum amplifications for frequencies > 1 Hz. The limitations of these parameterizations of the influence of directivity on ground motion estimations are discussed in the context of ground motion simulations in subsequent sections.

ESTIMATES OF GROUND MOTIONS USING SIMULATIONS

Earthquake ground motions, by definition, are always "site specific". Site responses can substantially modify ground motion amplitudes, durations, and frequency content. Site-specific factors include "large scale crustal factors" such as three-dimensional (3D) velocity, anisotropy, and attenuation structures between a site and a fault, and "local factors" such as shallow velocity structure, anisotropy, attenuation mechanisms, and local topography. Heterogeneous faulting associated with large earthquakes provides additional "site specific" ground motion effects by producing variable seismic radiation of elastic energy as a function of azimuth, takeoff-angles, and fault position relative to a site. It is impossible to deterministically account for all these factors. Consequently, stochastic simulation approaches that incorporate statistical variations of faulting and elastic wave propagation are used to estimate statistical distributions of site-specific ground motions. The presentation here focuses on the multitude of physical factors that complicate ground motion estimation. An elegant tool, isochrones, are used to provide intuitive

insights into factors that strong influence ground motions. Several calculations are presented to illustrate some of the challenges of ground motion estimation.

GROUND MOTION SYNTHESIS

The ground motions produced at any site by an earthquake are the result of seismic radiation associated with the dynamic faulting process and the manner in which that seismic energy propagates from positions on the fault to a site of interest. A discrete representation is used to emphasize the discrete building blocks or factors that interact to produce strong ground motions. We assume that fault rupture initiates at some point on the fault (the hypocenter) and proceeds outward along the fault surface. Using the representation theorem (Spudich and Archuleta, 1987), ground velocity, $\dot{u}_k(t)$, depends on the convolution of the time evolution of the slip-time functions, $s_{ij}(t)$, and the Green functions, $g_{kij}(t)$, the impulse responses between the fault and the site (Figure 2) as

$$\dot{u}_k(t) = \sum_{ij}^{nm} \dot{s}_{ij}(t) \otimes g_{kij}(t) \tag{3}$$

where *k* is the component of ground motion, *ij* are the indices of the discrete fault elements, *n* is the number of fault elements in the strike direction and *m* is the number of elements in dip direction (Figure 2). We use the notation $F(\omega)$ to indicate the modulus of the Fourier transform of $f(t)$. It is instructive to take the Fourier transform of (3) and pursue a discussion similar to Hutchings and Wu (1990) and Hutchings (1994) using

$$\dot{U}_k(\omega) = \sum_{ij}^{nm} \dot{S}_{ij}(\omega) e^{-i\omega\tau_{ij}(\omega)} \cdot G_{kij}(\omega) e^{-i\omega\phi_{kij}(\omega)} \tag{4}$$

where at each element *ij*, $\dot{S}_{ij}(\omega)$ is the source slip-rate amplitude spectrum, $\tau_{ij}(\omega)$ is the source phase spectrum, $G_{kij}(\omega)$ is the Green's function amplitude spectrum, and $\phi_{kij}(\omega)$ is the Green's function phase spectrum. The maximum peak ground motions are produced by a combination of factors that produce constant or linear phase variations with frequency over a large frequency band. While the relations in (3) and (4) are useful for synthesizing ground motions, they don't provide particularly intuitive physical insights into the factors that contribute to produce specific ground motion characteristic, particularly large peak accelerations, velocities, and displacements. We introduce isochrones as a fundamental forensic tool for understanding the genesis of ground motions. Isochrones are then used to provide simple geometric illustrations of how directivity varies between dipping dip-slip and vertical strike-slip faults.

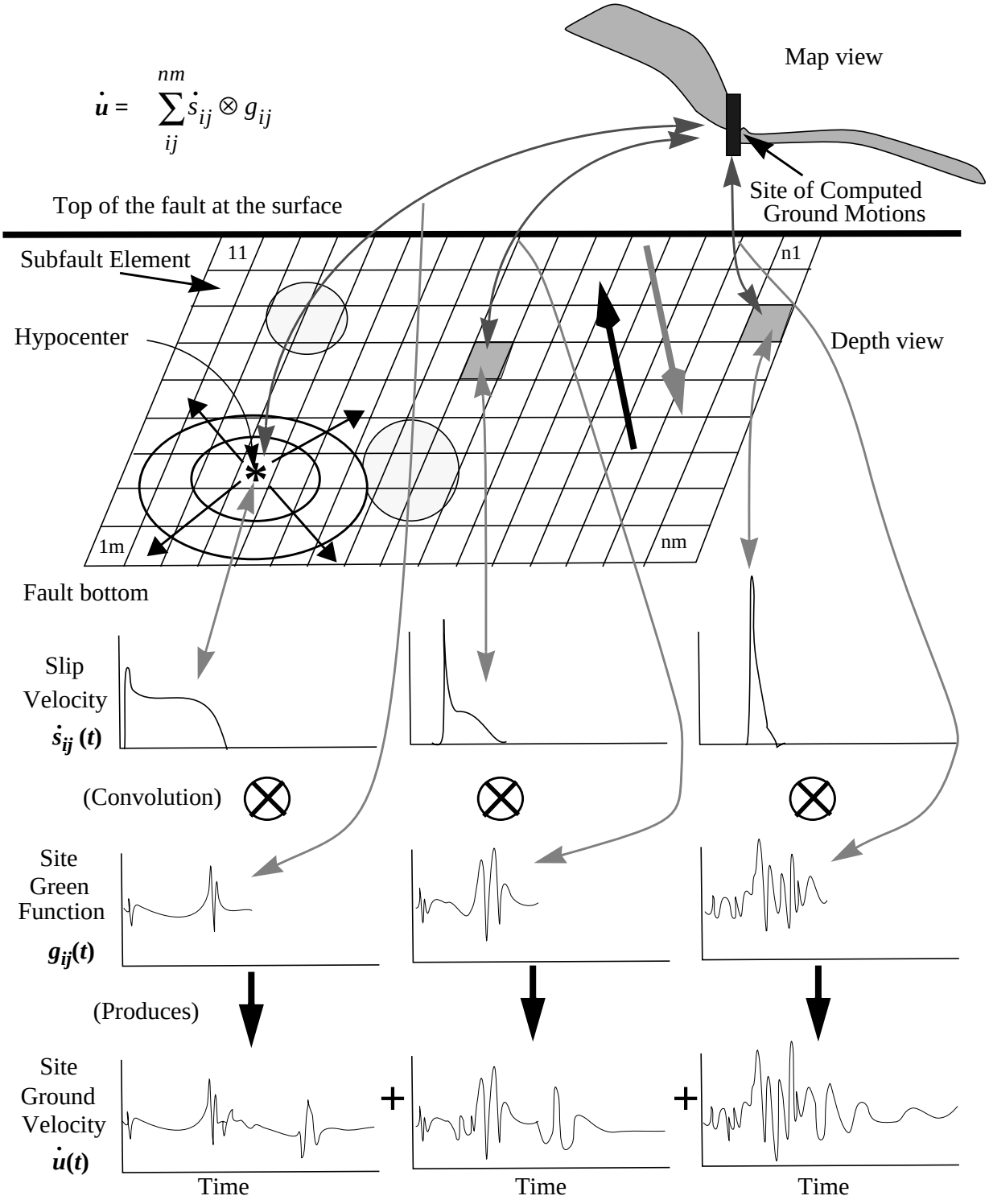

Figure 2. Schematic diagram of finite fault rupture calculation of ground motions.Three discrete subfault elements in the summation are shown. Rings and arrows emanating from the hypocenter represent the time evolution of the rupture.The Green functions actually consist of eight components of ground motion and three components of site ground velocities are calculated. Large arrows denote fault slip orientation which is shown as predominantly reverse slip with a small component of right-lateral strike slip. Stippled circles schematically represent regions of high stress drop.

Isochrones and Rupture Directivity

Bernard and Madariaga (1984) and Spudich and Frazer (1984; 1987) developed the isochrone integration method to compute near-source ground motions for finite-fault rupture models. Isochrones are all the positions on a fault that contribute seismic energy that arrives at a specific receiver at the same time. By plotting isochrones projected on a fault, times of large amplitudes in a ground motion time history can be associated with specific regions and characteristics of fault rupture and healing.

A simple and reasonable way to employ the isochrone method for sites located near faults is to assume that all significant seismic radiation from the fault consists of first shear-wave arrivals. A further simplification is to use a simple trapezoidal slip-velocity pulse. Let $f(t)$ be the slip function, For simplicity we assumed $\ddot{f}(t) = \delta(t - t_r) - \delta(t - t_h)$ where t_r is rupture time, and t_h is healing time. Then, all seismic radiation from a fault can be described with rupture and healing isochrones. Ground velocities (v) and accelerations (a) produced by rupture or healing of each point on a fault can be calculated from (Spudich and Frazer, 1984)

$$v(\boldsymbol{x}, t) = \ddot{f}(t) \otimes \int_{y(t, \boldsymbol{x})} (\boldsymbol{s} \cdot \boldsymbol{G}) c \, dl \tag{5}$$

$$a(\boldsymbol{x}, t) = \ddot{f}(t) \otimes \int_{y(t, \boldsymbol{x})} \left[c^2 \left(\frac{d\boldsymbol{s}}{dq} \cdot G \right) + c^2 \left(\frac{dG}{dq} \cdot \boldsymbol{s} \right) + \frac{dc}{dt} \cdot (\boldsymbol{s} \cdot G) \right] dl \tag{6}$$

where c is isochrone velocity, $\boldsymbol{s}$ is slip velocity (either rupture or healing), G is a ray theory Green function, $\boldsymbol{x}$ are position vectors, $y(t,\boldsymbol{x})$ are isochrones, dl denotes isochrone line integral integration increment, and dq denotes a spatial derivative.

Since isochrones are central to understanding seismograms, we provide explicit expressions for rupture and healing isochrones to illustrate how source and propagation factors can combine to affect ground motions. The arrival times of rupture at a specific receiver are

$$T_r(\boldsymbol{x}) = t_\beta(\boldsymbol{x}, \xi) + t_r(\xi) \tag{7}$$

where $\boldsymbol{x}$ is the receiver position, ξ are all fault positions, t_β are shear-wave propagation times between the receiver and all fault positions, and t_r is the rupture time at all fault positions. The arrival times of healing at a specific receiver are

$$T_h(x) = T_r(x) + R(\xi) \tag{8}$$

where R are the rise times (the durations of slip) at all fault positions.

Archuleta (1984) showed that variations in rupture velocity had pronounced effects on calculated ground motions, whereas variations in rise times and slip-rate amplitudes cause small or

predicable changes on calculated ground motions. The effect of changing slip-rate amplitudes on ground motions is strongly governed by the geometrical attenuation ($1/r$ for far-field terms). Any change in the slip rate amplitudes affects most the ground motions for sites closest to the region on the fault where large slip-rate amplitudes occurred (Spudich and Archuleta,1987). This is not the case with rupture velocity or rise time; these quantities influence ground motions at all sites. However, as Anderson and Richards (1975) showed, it takes a 300% change in rise time to compensate for a 17% change in rupture time. Spudich and Oppenheimer (1986) show why this is so. Spatial variability of rupture velocity causes the integrand in (5) to become quite rough, thereby adding considerable high-frequency energy to ground motions. The roughness of the integrand in (5) is caused by variations of isochrone velocity c, where

$$c = \left| \underline{\nabla}_s T_r \right|^{-1} \tag{9}$$

where T_r is the isochrone from (7) and $\underline{\nabla}_s$ is the surface gradient operator. Variations of T_r on the fault surface associated with supershear rupture velocities, or regions on the fault where rupture jumps discontinuously can cause larger or singular values of c, called critical points by Farra et al. (1986). Spudich and Frazer (1984) showed that the reciprocal of c, isochrone slowness is equivalent to the seismic directivity function in the two-dimensional case. Thus, by definition, critical points produce rupture directivity, and as is shown with simulations later, need not be associated strictly with forward rupture directivity, but can occur for any site located normal to a portion of a fault plane where rupture velocities are supershear.

It is useful to interpret (5) and (6) in the context of the discrete point-source summations in (3) and (4). When isochrone velocities become large on a substantial area of a fault it simply means that all the seismic energy from that portion of the fault arrives at nearly the same time at the receiver; the summation of a finite, but large number of band-limited Green's functions means that peak velocities remain finite, but potentially large. Large isochrone velocities or small isochrone slownesses over significant region of a fault are diagnostic of ground motion amplification associated with rupture directivity; the focusing of a significant fraction of the seismic energy radiated from a fault at a particular site in a short time interval. In this way isochrones are a powerful tool to dissect ground motions in relation to various characteristics of fault rupture. Times of large ground motion amplitudes can be directly associated with the regions of the fault that have corresponding large isochrone velocities or unusually large slip velocities. From (7) and (8) it is clear that both fault rupture variations, and shear-wave propagation time variations, combine to determine isochrones and isochrone velocities.

Isochrone Analysis of Directivity: Contrasts Between Strike-Slip and Dip-Slip Faulting

Joyner (1991) discussed directivity using a simple line source model. A similar approach is used here to illustrate how directivity differs between vertical strike-slip faults and dipping dip-slip faults. To focus on source effects, we consider unilateral, one-dimensional ruptures in a homogenous half-space (Figure 3). The influence of the free surface on amplitudes is ignored. The rupture velocity is set equal to the shear-wave velocity to minimize time delays and to maximize rupture directivity. To eliminate geometric spreading, stress drops increase linearly

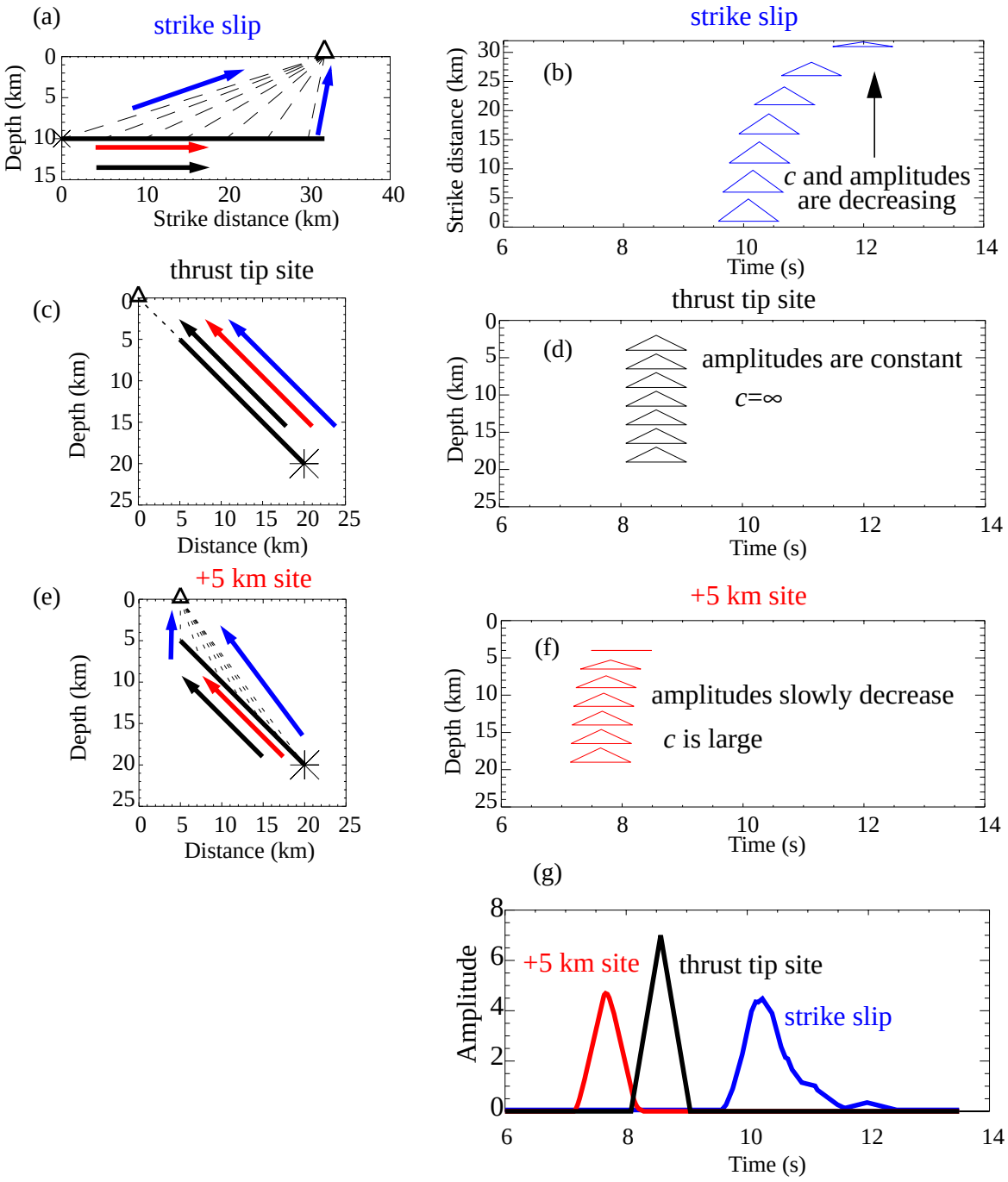

Figure 3. Schematics of line source orientations for strike-slip (a) and thrust faults (c) and (e) relative to ground motion sites (triangles). Black arrows show the orientation of the faults, red arrows show fault rupture directions, and blue arrows show S-wave propagation directions (dashed lines) to the sites. Discrete velocity contributions for seven evenly-spaced positions along the fault are shown to the right of each rupture model (b, d, f) as triangles with amplitudes (heights) scaled by the radiation pattern. The output ground motions for each fault rupture are shown in (g). Isochrone velocity, *c*, is infinity in (d), is large, but finite, in (f), and decreases as the fault nears the ground motion site in (b).

with distance from the site in a manner that produces uniform slip velocity contribution to the surface site for all points on the faults. Healing is ignored, only the rupture pulse is considered. Thrust dip-slip faulting is used to produce coincident rake and rupture directions. Seismic radiation is simplified to triangular slip-velocity pulses with widths of one second.

For the strike-slip fault, the fault orientation and rupture directional are coincident. But, as fault rupture approaches the site, takeoff angles increase, so the radiation pattern reduces amplitudes, and total propagation distances (rupture length plus propagation distance) increase to disperse shear-wave arrivals in time (Figures 3a and 3b). The surface site located along the projection of the thrust fault to the surface receives all seismic energy from the fault at the same time, and *c* is infinity because the fault orientation, rupture, and shear-wave propagation directions are all coincident for the entire length of the fault (Figures 3c and 3d). Consequently, although the strike-slip fault is 50% longer than the thrust fault, the thrust fault produces a peak amplitude 58% larger than the strike-slip fault. The thrust fault site receives maximum amplitudes over the entire radiated frequency band. The strike-slip site receives reduced high-frequency amplitudes because the increasing shear-wave propagation delays disperse the arrival times of seismic radiation from different portions of the fault, producing a broadened ground motion velocity pulse. The geometric interaction between dip-slip faults and propagation paths to surface sites located above those faults produces a kinematic recipe for maximizing both isochrone velocities and radiation patterns at surface sites that is unique to dip-slip faults.

Typically, seismic velocities increase with depth which changes positions of maximum rupture directivity compared to Figure 3. For dip-slip faults, the region of maximum directivity is moved away from the projection of the fault to the surface, toward the hanging wall. This bias is dependent on velocity gradients, and the dip and depth of the fault. For strike-slip faults, a refractor geometry can increase directivity by reducing takeoff angle deviations relative to the rupture direction for depth intervals that depend on the velocity structure and position of the surface site. We return to the issue later in the paper.

When the two-dimensional nature of finite-fault rupture is considered, rupture directivity is not as strong as suggested by this one-dimensional analysis (Bernard et al., 1996), but the distinct amplitude and frequency differences between strike-slip and dip-slip faulting directivity remain. Full two-dimensional analyses are presented in a subsequent section. A more complete discussion of source and propagation factors influencing ground motions is presented next to provide a foundation for discussion of amplification associated with rupture directivity. The approach here is to discuss ground motions separately in terms of the source and propagation and then to discuss how source and propagation can jointly interact to strongly influence ground motion behavior.

SOURCE AMPLITUDE AND PHASE FACTORS

Table 1 list factors influencing source amplitudes, $\dot{S}_{ij}(\omega)$. Table 2 lists factors influencing source phase, $\tau_{ij}(\omega)$. The flat portion of an amplitude spectrum are the frequencies less than a corner frequency, ω_c, which is defined as the intersection of low- and high-frequency asymptotes following Brune (1970). The stress drop, $\Delta\sigma$, defined as the difference between an initial stress, σ_0, minus the dynamic frictional stress, σ_f, is the stress available to drive fault slip (Aki, 1983). Rise time, t_Δ, is the duration of slip at any particular point on the fault. Rise times are

heterogeneous over a fault rupture surface. Because the radiation pattern for seismic phases such as body waves and surface waves are imposed by specification of rake (slip direction) at the source and are a function of focal mechanism, radiation pattern is included in the source discussion.

Regression between moment and fault area (Wells and Coppersmith, 1994; Somerville et al., 1999) show that uncertainties in moment magnitude and fault area are sufficient to produce moment uncertainties of 50% or more for any particular fault area. Consequently, the absolute scaling of synthesized ground motions for any faulting scenario have about factor of two uncertainties related to seismic moment (equivalently, average stress drop) uncertainties. Thus, moment-fault area uncertainties introduce a significant source of uncertainty in ground motion estimation.

Andrews (1981) and Frankel (1991) showed that correlated-random variations of stress drop over fault surfaces that produce self-similar spatial distributions of fault slip are required to explain observed ground motion frequency amplitude responses. Somerville et al. (1999) showed that a self-similar slip model can explain inferred slip distributions for many large earthquakes and they derive relations between many fault rupture parameters and seismic moment. Their results provide support for specifying fault rupture models using a stochastic spatially varying stress drop where stress drop amplitude decays as the inverse of wavenumber to produce self-similar slip distributions. They assume that mean stress drop is independent of seismic moment. Based on their analysis and assumptions Somerville et al. (1999) provide recipes for specifying fault rupture parameters such as slip, rise times, and asperity dimensions as a function of moment. Mai and Beroza (2000) showed that $5.3 < \mathbf{M} < 8.1$ magnitude range dip-slip earthquakes follow self-similar scaling as suggest by Somerville et al. (1999). However, for strike slip earthquakes, as moment increases in this magnitude range, they showed that seismic moments scale as the cube of fault length, but fault width saturates. Thus, for large strike slip earthquakes average slip increases with fault rupture length, stress drop increases with magnitude, and self-similar slip scaling does not hold. The large stress drops observed for the **M** 7.7 1999 Chi-Chi, Taiwan thrust-faulting earthquake (Oglesby et al., 2000) suggest that self-similar slip scaling relations may also break-down at larger moments for dip-slip events. Oglesby et al. (1998; 2000) showed that stress drop behaviors are fundamentally different between dipping reverse and normal faults. These results suggest that stress drop may be focal mechanism and magnitude dependent. There are still significant uncertainties as to the appropriate specifications of fault rupture parameters to simulate strong ground motions, particularly for larger magnitude earthquakes. Thus, the details of appropriate spatial specification of stress drops and/or slip velocities as a function of focal mechanism and magnitude are yet to be fully resolved.

Day (1982) showed that intersonic rupture velocities ($\beta < V_r < \alpha$) can occur during earthquakes, particularly in regions of high prestress (asperities), and the peak slip velocity is strongly coupled to rupture velocity for nonuniform prestresses. While average rupture velocities typically remain subshear, high-stress asperities can produce local regions of supershear rupture combined with high slip velocities. Supershear rupture velocities have been observed or inferred to have occurred during several earthquakes, including the **M** 6.9 1979 Imperial Valley strike-slip earthquake (Olson and Apsel, 1982; Spudich and Cranswick, 1984; Archuleta, 1984), the **M** 6.9 1980 Irpinia normal-faulting earthquake (Belardinelli et al., 1999), the **M** 7.0 1992 Petrolia thrust-faulting

earthquake (Oglesby and Archuleta, 1997), the **M** 7.3 Landers strike-slip earthquake (Olsen et al., 1997; Bouchon et al., 1998; Hernandez et al., 1999) the **M** 6.7 1994 Northridge thrust-faulting earthquake (O'Connell, 1999b), and the 1999 **M** 7.5 Izmit and Duzce Turkey strike-slip earthquakes (Bouchon et al., 2001).

Harris and Day (1997) show that rupture velocities and slip-velocity functions can be significantly modified when a fault bisects a low-velocity zone. The low-velocity zone can produce asymmetry of rupture velocity and slip velocity. This type of velocity heterogeneity produces an asymmetry in seismic radiation pattern and abrupt and/or systematic spatial variations in rupture velocity. These differences are most significant in regions subject to rupture directivity, and may lead to substantially different peak ground motions occurring at either end of a strike slip fault (Bouchon et al., 2001). Thus, position of a site relative to the fast and slow sides of a fault and rupture direction may be significant in terms of the dynamic stress drops and rupture velocities that are attainable in the direction of the site. Observations and numerical modeling show that the details of stress distribution on the fault can produce complex rupture velocity distributions and even discontinuous rupture, factors not typically accounted for a kinematic rupture models used to predict ground motions (e.g. Somerville et al., 1991; Schneider et al., 1993; Hutchings, 1994; Tumarkin et al., 1994; Zeng et al., 1994; Berensev and Atkinson, 1997; O'Connell, 1999c). Even if only smooth variations of subshear rupture velocities are considered ($0.6*\beta < V_r < 1.0*\beta$), rupture velocity variability introduces ground motion estimation uncertainties of at least a factor of two (Berensev and Atkinson, 1997), and larger uncertainties for sites subject to directivity.

Rupture direction may change due to strength or stress heterogeneities on a fault. Beroza and Spudich (1988) inferred that rupture was delayed and then progressed back toward the hypocenter during the **M** 6.2 1984 Morgan Hill earthquake. Oglesby and Archuleta (1997) inferred that arcuate rupture of an asperity may have produced accelerations > 1400 cm/s^2 at Cape Mendocino during the **M** 7.0 1992 Petrolia earthquake. These results are compatible with numerical simulations of fault rupture on a heterogeneous fault plane. Das and Aki (1977) modeled rupture for a fault plane with high-strength barriers and found that rupture could occur discontinuously beyond strong regions which may subsequently rupture or remain unbroken. Day (1982) found that rupture was very complex for the case of nonuniform press stress and that rupture jumped beyond some points on the fault, leaving unbroken areas behind the rupture, which subsequently ruptured. In the case of slip resistant asperity, Das and Kostrov (1983) found that when rupture began at the edge of the asperity, it proceeded first around the perimeter and then failed inward in a “double pincer movement”. Thus, even the details of rupture propagation direction are not truly specified once a hypocenter position is selected.

Guatteri and Spudich (1998) showed that time-dependent dynamic rake rotations on a fault become more likely as stress states approach low stresses on a fault when combined with a heterogeneous distributions of stress and nearly complete stress drops. Pitarka et al. (2000) found that eliminating radiation pattern coherence between 1 Hz and 3 Hz reproduced observed ground motions for the 1995 **M** 6.9 Hyogo-ken Nanbu (Kobe) earthquake. Spudich et al. (1998) used fault striations to infer that the Nojima fault slipped at low stress levels with substantial rake rotations occurring during the 1995 Hyogo-ken Nanbu earthquake. This dynamic rake rotation can reduce radiation-pattern coherence at increasing frequencies by increasingly randomizing rake directions for decreasing time intervals near the initiation of slip at each point on a fault, for

increasingly complex initial stress distributions on faults. Vidale (1989) showed that the standard double-couple radiation pattern is observable to 6 Hz based on analysis of the mainshock and an aftershock from the Whittier Narrows, California, thrust-faulting earthquake sequence. In contrast, Liu and Helmberger (1985) found that a double-couple radiation pattern was only discernible for frequencies extending to 1 Hz based on analysis the 1979 Imperial Valley earthquake and an aftershock. Bent and Helmberger (1989) estimate a $\Delta\sigma$ of 75 MPa bars for the 1987 Whittier Narrows **M** 6.1 thrust faulting earthquake, but allow for a $\Delta\sigma$ as low as 15.5 MPa. The case of high initial, nearly homogeneous stresses that minimizes rake rotations may produce high-frequency radiation pattern coherence as observed by Vidale (1989). These results suggest that there may be a correlation between the maximum frequency of radiation pattern coherence, initial stress state on a fault, focal mechanism, and stress drop.

PROPAGATION AMPLITUDE AND PHASE FACTORS

Table 3 list factors influencing propagation amplitudes, $G_{kij}(\omega)$. Table 4 lists factors influencing propagation phase, $\phi_{ij}(\omega)$.

Large-scale basin structure can substantially amplify and extend durations of strong ground motions (Frankel and Vidale, 1992; Frankel, 1993; Olsen and Archuleta, 1996; Wald and Graves; 1998; Frankel and Stephenson, 2000; Koketsu and Kikuchi, 2000; Frankel et al., 2001). Basin-edge waves can substantially amplify strong ground motions in basins (Liu and Heaton, 1984; Frankel et al., 1991; Phillips et al., 1993; Spudich and Iada, 1993; Kawase, 1996; Pitarka et al., 1998, Frankel et al., 2001). This is a particular concern for fault-bounded basins were rupture directivity can constructively interact with basin-edge waves to produce extended zones of extreme ground motions (Kawase, 1996; Pitarka et al., 1998), a topic revisited later in the paper. Even smaller scale basin or lens structures on the order of several kilometers in diameter can produce substantial amplification of strong ground motions (Alex and Olsen, 1998; Graves et al., 1998; Davis et al., 2000). Basin-edge waves can be composed of both body and surface waves (Spudich and Iada, 1993; Meremonte et al., 1996; Frankel et al., 2001) which provides a rich wavefield for constructive interference phenomena over a broad frequency range.

Critical reflections off the Moho can produce amplification at distances > ~75-100 km (Somerville and Yoshimura, 1990; Catchings and Kohler, 1996). The depth to the Moho, hypocentral depth, direction of rupture (updip versus downdip), and focal mechanism determine the amplification and distance range that Moho reflections may be important. For instance, Catchings and Mooney (1992) showed that Moho reflections amplify ground motions in the > 100 km distance range in the vicinity of the New Madrid seismic zone in the central United States.

Numerous studies have demonstrated that the seismic velocities in the upper 30 to 60 m can greatly influence the amplitudes of earthquake grounds motions at the surface (e.g. Borcherdt et al., 1979; Joyner et al., 1981; Seed et al., 1988). Williams et al. (1999) showed that significant resonances can occur for impedance boundaries as shallow as 7-m depth. Boore and Joyner (1997) compared the amplification of generic rock sites with very hard rock sites for 30 m depth averaged velocities. They defined very hard rocks sites as sites have *S* velocities at the surface > 2.7 km/s and generic rock sites as sites where *S* velocities at the surface are ~0.6 km/s and increase to > 1 km/s at 30 m depth. Boore and Joyner (1997) found that amplifications on generic

rock sites can be in excess of 3.5 at high frequencies, in contrast to the amplifications of less than 1.2 on very hard rock sites. Considering the combined effect of attenuation and amplification, amplification for generic rocks sites peaks between 2 and 5 Hz at a maximum value less than 1.8 (Boore and Joyner, 1997).

A common site-response estimation method is to use horizontal-to-vertical (*H/V*) spectral ratio method with shear waves (Lermo and Chavez-Garcia, 1993) to test for site resonances at a site. The *H/V* method is similar to the receiver -function method of Langston (1979). Several investigations have shown the *H/V* approach provides robust estimates of resonant frequencies (e.g., Field and Jacob, 1995; Castro et al., 1997; Tsubio et al., 2001) although absolute amplification factors are less well resolved (Castro et al., 1997; Bonilla et al., 1997). One-dimensional site-response approaches may fail to quantify site amplification in cases when upper crustal three-dimensional velocity structure is complex. In southern California, Field (2000) found that the basin effect had a stronger influence on peak acceleration than detailed geology used to classify site responses. Hartzell et al. (2000) found that site amplification characteristics at some sites in the Seattle region cannot be explained using 1D or 2D velocity models, but that 3D velocity structure must be considered to fully explain local site responses. Chavez-Garcia et al. (1999) showed that laterally propagating basin-generated surface waves can not be differentiated from 1D sites effects using frequency domain techniques such as *H/V* ratios or reference site ratios. The ability to conduct site-specific ground motion investigations is predicated on the existence of geological, geophysical, and geotechnical engineering data to realistically characterize earthquake sources, crustal velocity structure, local site structure and conditions, and to estimate the resultant seismic responses at a site. Lack of information about 3D variations in local and crustal velocity structure are serious impediments to ground motion estimation.

It is now recognized that correlated-random 3D velocity heterogeneity is an intrinsic property of Earth's crust (see Sato and Fehler, 1998 for a discussion). Correlated-random means that random velocity fluctuations are dependent on surrounding velocities with the dependence being inversely proportional to distance. Weak (standard deviation, ε, of ~5%), random fractal crustal velocity variations are required to explain observed short-period ($T < 1\ s$) body-wave travel time variations, coda amplitudes, and coda durations for ground motions recorded over length scales of tens of kilometers to tens of meters. (Frankel and Clayton, 1986), most well-log data (Sato and Fehler, 1998), the frequency dependence of shear-wave attenuation (Sato and Fehler, 1998), and envelope broadening of shear waves with distance (Sato and Fehler, 1998). As a natural consequence of energy conservation, the excitation of coda waves in the crust means that direct waves (particularly direct shear waves that dominate peak ground motions) that propagate along the minimum travel-time path from the source to the receiver lose energy with increasing propagation distance as a result of the dispersion of energy in time and space.

Following Frankel and Clayton (1986) fractal, self-similar velocity fluctuations are described with an autocorrelation function, *P*, of the form

$$P(k_r) \approx \frac{a^n}{(1 + k_r a)^n} \tag{10}$$

where a is the correlation distance, k_r is radial wavenumber, n=2 in 2D, and n=3 in 3D. When n=4 an exponential power law results (Sato and Fehler, 1998). Smoothness increasing with distance as a increases in (10) and overall smoothness is proportional to n in (10). This is a more realistic model of spatial geologic material variations than completely uncorrelated, spatially independent, random velocity variations. “Correlated-random” is shortened here to “random” for brevity. Let λ denote wavelength. Forward scattering dominates when $\lambda << a$ (Sato and Fehler, 1998). The situation is complicated in self-similar fractal media when considering a broad frequency range relevant to strong motion seismology (0.1 to 10 Hz) because λ spans the range $\lambda >> a$ to $\lambda << a$ and both forward and backscattering become important, particularly as n decreases in (10). Thus, it is difficult to develop simple rigorous expressions to quantify amplitude and phase terms associated with wave propagation through the heterogeneous crust (see Sato and Fehler, 1998). O'Connell (1999a) showed that direct shear-wave scattering produced by *P-SV*-wave coupling associated with vertical velocity gradients typical of southern California, combined with 3D velocity variations with n=2 and a standard deviation of velocity variations of 5% in (10), reduce high-frequency peak ground motions for sediment sites close to earthquake faults. The most important result of O’Connell (1999a) was to show that crustal scattering could substantially influence the amplification of near-fault ground motions in areas subjected to significant directivity. Scattering also determines the propagation distances required to randomize phase as discussed later in the paper.

Dynamic reduction of soil moduli and increases in damping with increasing shear strain can substantially modify ground motion amplitudes as a function of frequency (Ishihara, 1996). While there has been evidence of nonlinear soil response in surface strong motion recordings (Field et al., 1997; Cultera et al., 1999), interpretation of these surface records solely in terms of soil nonlinearity is intrinsically non-unique (O'Connell, 1999a). In contrast, downhole strong motion arrays have provided definitive evidence of soil nonlinearity consistent with laboratory testing of soils (Chang et al., 1991; Wen et al., 1995, Ghayamghamain and Kawakami, 1996; Satoh et al, 1995, 1997, 2001).

Idriss and Seed (1968a, b) introduced the “equivalent linear method” to calculate nonlinear soil response, which is an iterative method based on the assumption that the response of soil can be approximated by the response of a linear model whose properties are selected in relation to the average strain that occurs at each depth interval in the model during excitation. Joyner and Chen (1975) used a direct nonlinear stress-strain relationship method to demonstrate that the equivalent linear method may significantly underestimate short-period motions for thick soil columns and large input motions. Archuleta et al. (2000) and Bonilla (2000) recently demonstrated that dynamic pore-pressure response can substantially modify nonlinear soil response and actually amplify and extend the durations of strong ground motions for some soil conditions. When a site is situated on soil it is critical to determine whether soil response will decrease or increase ground amplitudes and durations, and to compare the expected frequency dependence of the seismic soil responses with the resonant frequencies of the engineered structure(s). When soils are not saturated, the equivalent linear method is usually adequate with consideration of the caveats of Joyner and Chen (1975). When soils are saturated and interbedding sands and/or gravels between clay layers is prevalent, a fully nonlinear evaluation of the site that accounts for dynamic pore pressure responses may be necessary (Archuleta et al., 2000).

Lomnitz et al. (1999) showed that for the condition, $0.91\beta_1 < \alpha_0$, where β_1 is the shear wave velocity of low-velocity material beneath saturated soils, and α_0 is the acoustic (compressional-wave) velocity in the near-surface material, a coupled mode between Rayleigh waves propagating along the interface and compressional waves in the near surface material propagates with phase velocity α_0. This mode can propagate over large distances with little attenuation. Lomnitz et al. (1999) note that this set of velocity conditions provides a "recipe" for severe earthquake damage on soft ground when combined with a large contrast in Poisson's ratio between the two layers, and when the resonant frequencies of the mode and engineering structures coincide. 2D viscoelastic finite-difference are presented in a subsequent section which demonstrate the existence of this wave mode.

Anisotropy complicates polarizations of shear waves. Coutant (1996) showed that shallow (< 200 m) shear-wave anisotropy strongly influences surface polarization of shear waves for frequencies < 30 Hz. Chapman and Shearer (1989) show that quasi-shear (*qS*) wave polarizations typically twist along ray paths through gradient regions in anisotropic media, causing frequency-dependent coupling between the *qS* waves. They show that this coupling is much stronger than the analogous coupling between *P* and *SV* waves in isotropic gradients because of the small difference between the *qS*-wave velocities. Chapman and Shearer (1989) show that in some cases, far-field excitation of both quasi-shear wave and shear-wave splitting will result from an incident wave composed of only one of the quasi-shear waves. The potential for stronger coupling of quasi-shear waves suggest that the influence of anisotropy on influence shear-wave polarizations and peak ground motion may be significant in some cases. While the influence of anisotropy on strong ground motions is unknown, it is prudent to avoid suggesting that only a limited class of shear-wave polarizations are likely for a particular site based on isotropic ground motion simulations or ground motion observations at other sites.

Velocity anisotropy in the crust can substantially distort the radiation pattern of body waves with shear-wave polarization angles diverging from those in an isotropic medium by as much as 90 degrees or more near directions where group velocities of quasi-*SH* and *SV* wave deviate from corresponding phase velocities (Kawasaki and Tanimoto, 1981). Thus, anisotropy has the potential to influence radiation pattern coherence as well as ground motion polarization. A common approach is to assume the double-couple radiation pattern disappears over a transition frequency band extending from 1 Hz to 3 Hz (Pitarka et al., 2000) or to 10 Hz (Zeng and Anderson, 2000). The choice of frequency cutoff for the radiation pattern significantly influences estimates of peak response in regions prone to directivity for frequencies close to and greater than the cutoff frequency. This is a very important parameter for stiff (high-frequency) structures such as buildings that tend to have natural frequencies in the 0.5 to 5 Hz frequency band (see discussion in Frankel, 1999).

Topography can substantially influence peak ground motions. Schultz (1994) showed that an amplification factor of 2 can be easily achieved near the flank of hills relative to the flatter portions of a basin and that substantial amplification and deamplification of shear-wave energy in the 1 to 10 Hz frequency range can occur over short distances. Bouchon et al. (1996) showed that shear-wave amplifications of 50% to 100% can occur in the 1.5 Hz to 20 Hz frequency band near the tops of hills, consistent with observations from the 1994 Northridge earthquake (Spudich et al., 1996). Topography may also contribute to amplification in adjacent basins as well as the

contributing to differential ground motions with dilatational strains on the order of 0.003 (Hutchings and Jarpe, 1996).

These discussions of source and propagation influences on amplitudes and phase are necessarily abbreviated and are not complete, but do provide an indication of the challenges of ground motion estimation. Systematically evaluating all the source and wave propagation factors influencing site-specific ground motions is a daunting task, particularly since its unlikely that we know all the relevant source and propagation factors. Often, insufficient information exists to quantitatively evaluate many ground motion factors. Thus, it is useful to develop a susceptibility check list for ground motion estimation at a particular site. The list would indicate available information for each factor on scale ranging from ignorance to strong quantitative information and indicate how this state of information could influence ground motions at the site. The result of such a checklist would be a susceptibility rating for potential biases and errors for peak motion and duration estimates of site-specific ground motions.

GROUND MOTION SYNTHESIS TECHNIQUES

We now move to a discussion of ground motion synthesis approaches, starting with simplified methods, and then proceeding to discussions of the most comprehensive approaches currently in use.

Far-Field Simplified Ground Motion Synthesis

For sites located sufficiently distant from earthquake faults, it is reasonable to simplify the representation of the seismic source to a point or centroid. A definition of “sufficiently distance” is generally regarded as follows: A site should be several times a fault’s largest rupture dimension distant from a fault for confident application of the point-source approximation. This is particularly true for sites located along projections of the ends of the fault where directivity may influence peak ground motions for considerable distances. For a **M** 6.5 earthquake with a rupture length of 20 km, the point-source approximation may work well for sites located > 30 km from the fault. For a **M** 7.5 earthquake with a rupture length of 100 km, sites would need to be located > 200 km to use the point-source approximation with confidence for all periods of engineering interest and all azimuths.

The most widely used numerical ground motion method is a point source model based on the work of Hanks and McGuire (1981) and Boore (1983). This technique is referred to as the Band Limited White Noise-Random Vibration Theory (BLWN-RVT) method. The method uses a Fourier spectral representation of the seismic source spectrum specified by an idealized point source whose shape is then modified by factors which represent wave propagation effects. The technique models earthquake ground motions as a time series of band limited white noise with random phase. The BLWN-RVT technique appears to agree well with empirical observations of peak ground motions over the frequency range of 1-30 Hz (in a root-mean-square sense) and for situations where the point-source assumption is valid.

The BLWN-RVT model assumes a point source with energy distributed randomly in time over the duration of slip. The duration of slip is assumed to be equal to the inverse of the corner frequency

(Boore, 1983). The source spectrum can either be represented by a ω^{-2} Brune source model with a single corner frequency (Brune, 1970, 1971) or by a model having two corner frequencies (Atkinson, 1993). Based on Silva and Lee (1987) and assuming a Brune source model, the acceleration spectral density is given in terms of frequency, *f*, by:

$$A(f) = C \cdot \frac{f^2}{1 + (1/f_c)^2} \cdot \frac{M_o}{R} \cdot T(f) \cdot A(f) \cdot e^{\frac{-\pi \cdot f \cdot r}{\beta_{S_0} \cdot Q(f)}} \qquad (11)$$

where: M_o is seismic moment, *r* is distance to the equivalent point source, β_{so} is the shear wave velocity in the source region, *Q(f)* is a frequency dependent quality factor, *A(f)* are frequency dependent, near-surface amplification factors, *T(f)* is a high-frequency truncation filter, f_C is the source corner frequency and *C* is a constant that depends on density and shear wave velocity in the source region, shear-wave radiation averaged over a sphere (0.55) and the partition of energy into two horizontal components ($1/\sqrt{2}$). Two independent parameters must be specified to establish source scaling, seismic moment, M_o, and high-frequency stress parameter, $\Delta\sigma$. M_o is related to **M** by: $\log M_o = 1.5\ \mathbf{M} + 16.1$ (Hanks and Kanamori, 1979). The stress parameter and seismic moment are related to the corner frequency by: $f_C = \beta so\ (\Delta\sigma/8.44\ M_o)^{1/3}$ (Brune, 1970; 1971).

The acceleration spectral density appears to decay beyond some regionally specific maximum frequency. This observed truncation of the high frequency portion of the spectrum is responsible for justifying the band-limited nature of the stochastic model. Hanks (1982) referred to this site-dependent corner frequency as f_{max}. This spectral modification has generally been attributed to near-surface attenuation (Hanks, 1982; Anderson and Hough, 1984). Following Anderson and Hough (1984) the high-frequency truncation filter is represented as:

$$T(f) = e^{-\pi \cdot \kappa(r) \cdot f} \qquad (12)$$

where $\kappa(r)$ is a site specific, distance dependent parameter that represents intrinsic crustal attenuation. κ is a function not only of the distance, but of the shear-wave velocity (β) and seismic quality factor, Q_0, beneath the site. On the surface immediately above the source (zero epicentral distance), κ is given by:

$$\kappa(0) = \frac{H}{\beta_s \cdot Q_0} \qquad (13)$$

where *H* is depth beneath the station over which β_S and Q_0 are estimated. $\kappa(0)$, or simply kappa, is assumed to be directly related to attenuation in the near-surface crust directly beneath the site (Hough and Anderson, 1988). The kappa effect is interpreted to be dominated by crustal characteristics within the upper ~0.5-2.0 km (Silva and Darragh, 1995) and is site-specific and frequency independent (Hough et al., 1988).

Anelastic attenuation along the crustal travel path between the source and the near-surface is usually modeled with a frequency dependent seismic quality factor, *Q(f)*. Where:

$$Q(f) = Q_0 \cdot f^{\eta} \tag{14}$$

and Q_0 and η are region specific model parameters. Geometric attenuation is assumed to be distance dependent, $1/r$ for the near- and intermediate- distance body wave dominated regime, and $1/(\sqrt{r})$ for the more distant surface wave dominated regime.

Haddon (1995; 1996) showed that rupture directivity amplified high-frequency ground motions produced by the 1988 **M** 6.0 Saguenay earthquake for sites at distances > 100 km. Directivity was accentuated by a long-narrow rupture geometry with relatively short (~0.2 s) rise times. This type of rupture configuration produces shear-wave spectra with two corner frequencies associated with the short rise times and the longer rupture propagation duration over the entire fault (Haddon, 1996). Haddon (1996) suggests the single-corner ω^2 source spectral model may underestimate spectral amplitudes of future earthquakes in Eastern North America by as much as a factor of 6 for some frequencies. The recent discovery that rupture areas of strike-slip earthquakes on a portion of the San Andreas fault are elongated in the direction of slip (Rubin and Gillard, 2000) suggests that circular stress drop models may not adequately characterize seismic source properties for some faults.

Near-Source Ground Motion Time History Synthesis

Finite-source ground motion simulation provides a means to augment the relatively sparse set of strong motion recordings close to large earthquakes. Ground motion synthesis using finite-source modeling is necessary to determine the range of peak ground motions that could occur at sites close to faults. Finite-source modeling attempts to quantify the influence of complexities of a propagating fault rupture on near-source ground motions.

Recent near-source ground motion estimation methods fall into two classes: (1) stochastic methods, and (2) hybrid methods. All methods use stochastic specifications for some aspect of source and/or wave propagation. This is because purely deterministic methods (Aki, 1968; Haskell, 1969) fail to reproduce observed ground motion behaviors for frequencies > 1-3 Hz. Purely stochastic methods use phenomenological statistical descriptions of source and propagation processes. Hybrid methods typically partition ground motion synthesis into high- and low-frequency components and use deterministic source and/or propagation parameterizations for lower frequencies and stochastic and/or empirical approaches to specify high frequency source behavior. The transition frequency bands where source and propagation processes transform from nearly deterministic to nearly stochastic behaviors are not known, are probably region and site specific, but are generally assumed to overlap somewhere in the 1 to 10 Hz frequency band.

Source parameterization for near-source ground motion modeling approaches fall into two general classes, point-source summation (Hartzell, 1978; Irikura, 1983) and stochastic subevent summation (Silva and Lee, 1987; Schneider et al., 1993; Zeng et al., 1994; Beresnev and Atkinson; 1997). Point source summation approaches use explicit accuracy criteria to determine integration intervals as a function of frequency for the slip rate functions and Green's functions on the fault (Spudich and Archuleta, 1987, pp. 231-252). Integration grid spacing is proportional to local shear-wave and rupture velocities divided by frequency. Consequently, point-source summation becomes computationally more demanding with increasing frequency. The stochastic

subevent approach uses subevents in the $5 < \mathbf{M} < 6.5$ range to rapidly synthesize ground motions. The sub-event approximation introduces additional ground motion amplitude uncertainties associated with selection of sub-event magnitude (Beresnev and Atkinson, 1998). The composite source model of Zeng et al. (1994) consists of the superposition of circular sub-events across a fault, with sub-event radii distributed according to a power law. The sub-events are modeled as Brune pulses produced by a ω^{-2} spectra decay of the amplitude spectrum (Brune, 1970). Most point-source and subevent source models use slip models that produce self-similar spatial distributions of slip consistent with the low-frequency estimates of fault slip (Somerville et al., 1999). The source models of Silva and Lee (1987), Schneider et al. (1993), Zeng et al. (1994), and Berensev and Atkinson (1998) use constant rupture velocities. Virtually, all source models use randomized rise times. This is somewhat ironic, since ground motion amplitudes are much more sensitive to rupture velocity than rise time (Anderson and Richards, 1975; Archuleta, 1984; Spudich and Archuleta, 1987).

Wave propagation parameterization falls into four general categories: (1) Empirical Green's functions that use ground motions from small earthquakes (Hartzell, 1978; Irikura, 1983, Hutchings, 1994), (2) Hybrid methods that use long-period theoretical Green's function combined with high-frequency empirical Green's function (Heaton et al., 1995; Jarpe and Kasameyer, 1996; O'Connell, 1998; 1999a), (3) Hybrid methods that use long-period theoretical Green's functions combined with high-frequency stochastic BLWN-RVT responses (Silva and Lee, 1987; Schneider et al., 1993), and (4) Hybrid methods that use long-period theoretical Green's functions combined with theoretical scattering high-frequency responses (Zeng et al., 1994; Zeng and Anderson, 2000). Theoretical Green's functions may be calculated using 1D or 3D velocity models.

SIMULATIONS OF NEAR-SOURCE GROUND MOTIONS

It's beyond the scope of this paper to comprehensively compare and contrast all the ground motion simulation methods listed above. Instead, near-source ground motion simulations are presented here to highlight the influence of source and wave propagation properties on ground motion amplitudes and durations. Ground motion simulations are presented here to illustrate the influence of rupture directivity, focal mechanism, 3D velocity structure, and extremely low shear-wave velocity basins on ground motions.

Influence of Rupture Velocities on Ground Motions from a Blind Thrust Fault

Bouchon et al. (2001) showed that supershear rupture velocities with $v_r \approx \sqrt{2}\beta$ occurred during the 1999 **M** 7.5 Izmit and **M** 7.3 Duzce earthquakes in Turkey. Rosakis et al. (1999) first reported experimental evidence of supershear rupture velocities and found $v_r \approx \sqrt{2}\beta$ for in-plane (rupture in the direction of the applied stress) crack propagation. Fruend (1979) showed that stable growth of shear cracks at intersonic velocities, $\beta \le v_r \le \alpha$, is only possible at $v_r = \sqrt{2}\beta$; the energy flux into the crack tip, which provides the fracture energy to advance the rupture, is zero at all other intersonic velocities. Huang et al. (1999) and Gao et al. (1999) obtained the same results.

As a sensitivity exercise, supershear ground motion simulations of a **M** 6.7 blind thrust earthquake are constructed to represent an end-member, $v_r \approx \sqrt{2}\beta$, over the entire fault. Day (1982) showed that introducing stress heterogeneities on a fault tend to reduce the spatial extent of

intersonic velocities on a fault and that for antiplane mode III crack growth (rupture growth orthogonal to the applied stress) $v_r \leq \beta$. Thus, subshear simulations are constructed using $v_r \leq \beta$ with identical effective stress distributions, rupture geometries, and rise time distributions as the supershear ground motion simulations to isolate the influence of supershear rupture velocities on ground motions independent of other source factors.

The 3D elastic finite difference approach of O'Connell et al. (in press) is used to calculate hybrid scattering function-ray theory high-frequency Green's functions to incorporate first-order influences of 3D self-similar crustal velocity variations on the amplitude and phase responses of rock sites in an point-source summation valid for frequencies extending to 15 Hz. Sampling of slip and Green's functions satisfied a sampling criteria of 6 samples per wavelength (Archuleta and Spudich, 1987). The simulation geometry is shown in Figures 4a and 4b. The fault is 15 km long and ~29 km wide, dipping at 20° between depths of 8 km and 18 km. This is fault geometry represents classes of blind thrust faults that exist in southern California (Heaton et al., 1995; Shaw and Shearer, 1999). The rupture length is limited to 15 km to produce a **M** 6.7 earthquake to facilitate comparisons with **M** 6.7 strike faulting ground motions (Figure 4d). Rupture initiates at 17.8 km and 16.8 km depth near the bottom of the fault (Figure 4a) and at three strike positions (Figure 4b) to randomize rupture initiation positions.

Profiles of ground motion simulation sites were located 5 km inside the ends of the fault at 2 km intervals along the profiles (Figure 4b). Upper-crustal vertical velocity variations for the ray-theory portion of the Green's functions (Figure 4c) are typical of southern California (see Shaw and Shearer, 1999). A kinematic rupture model is used that mimics the spontaneous dynamic rupture behavior of a self-similar stress distribution model of Andrews and Boatwright (1998). The kinematic rupture model is also similar to the rupture model of Herrero and Benard (1994). A total of 50 effective stress models were used with six hypocenter randomizations to produce 300 rupture simulations for each position along the profiles shown in Figure 3b. Invoking symmetry, ground motions from the two inside profiles can be combined to produce 600 ground motions for each position along the profile (Figure 4b).

The spatial manifestations of rupture directivity on peak ground motion are substantially different between the subshear and supershear rupture velocity cases (Figures 5 and 6). Maximum amplification of peak ground motions for the subshear case occurs about 9 km in front of the fault tip (Figure 5). For subshear rupture velocities, the vertical velocity gradients (Figure 4c) refract direct shear-wave arrivals toward the hanging wall, displacing the maximum directivity position on the surface about 14 km away from surface projection of the fault (-22 km on Figure 5) toward the hanging wall and the buried fault tip. In contrast, the maximum directivity position for supershear rupture is produced several km beyond the surface projection of the fault (Figure 5). There is a ~16 km horizontal difference in the predicted positions of maximum peak ground motions between the subshear and supershear rupture velocity scenarios. Larger peak motions are predicted for sites located over the thrust fault for the supershear rupture velocity scenarios, with median supershear PSA's and PSV's consistently being about 2 to 4 times larger than for subshear velocities for sites located 5-15 km behind the fault tip on the hanging wall. Thus, predictions of the positions of large ground motions close to a buried thrust fault are strongly linked to assumed rupture velocities.

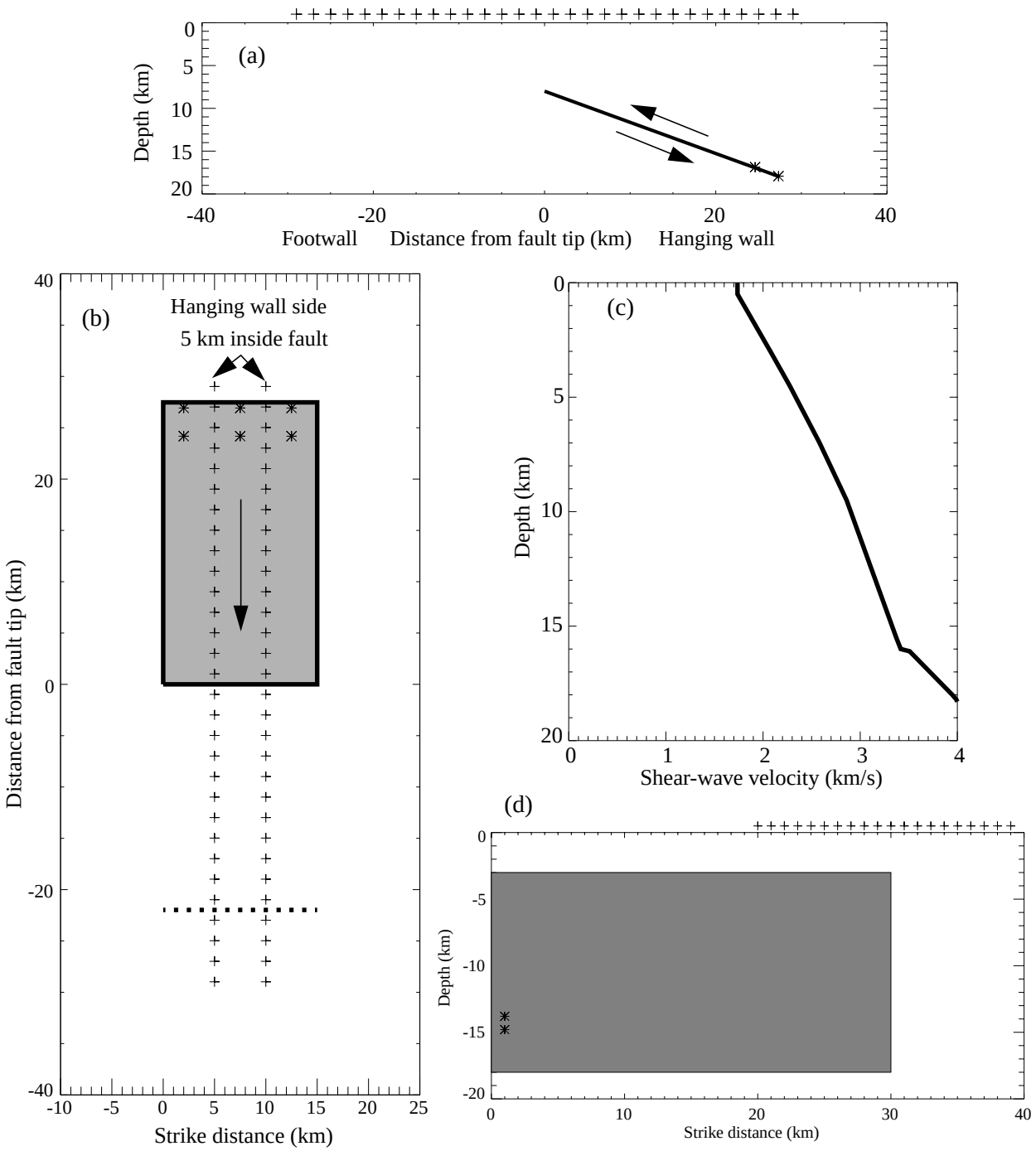

Figure 4. Cross section (a) and plan view (b) of the blind thrust fault geometry use to simulate subshear and supershear ground motions. The pluses in (a) show surface receiver site positions and stars show the two hypocenter depths used in the simulations. The shaded rectangle in (b) is the fault surface projected into plan view, stars show epicenter positions, pluses show profiles of receiver sites, for positions within the strike distance range of the fault, the arrow shows the displacement direction of the hanging wall, and the dashed lines shows where the projection of the fault intersects the free surface. The 1D shear-wave velocity structure used to calculate the ray portion of the Green's functions is shown in (c). The strike-slip rupture geometry in depth (shaded rectange), site locations along the surface above the fault (pluses), and hypocentes (stars) are shown in (d).

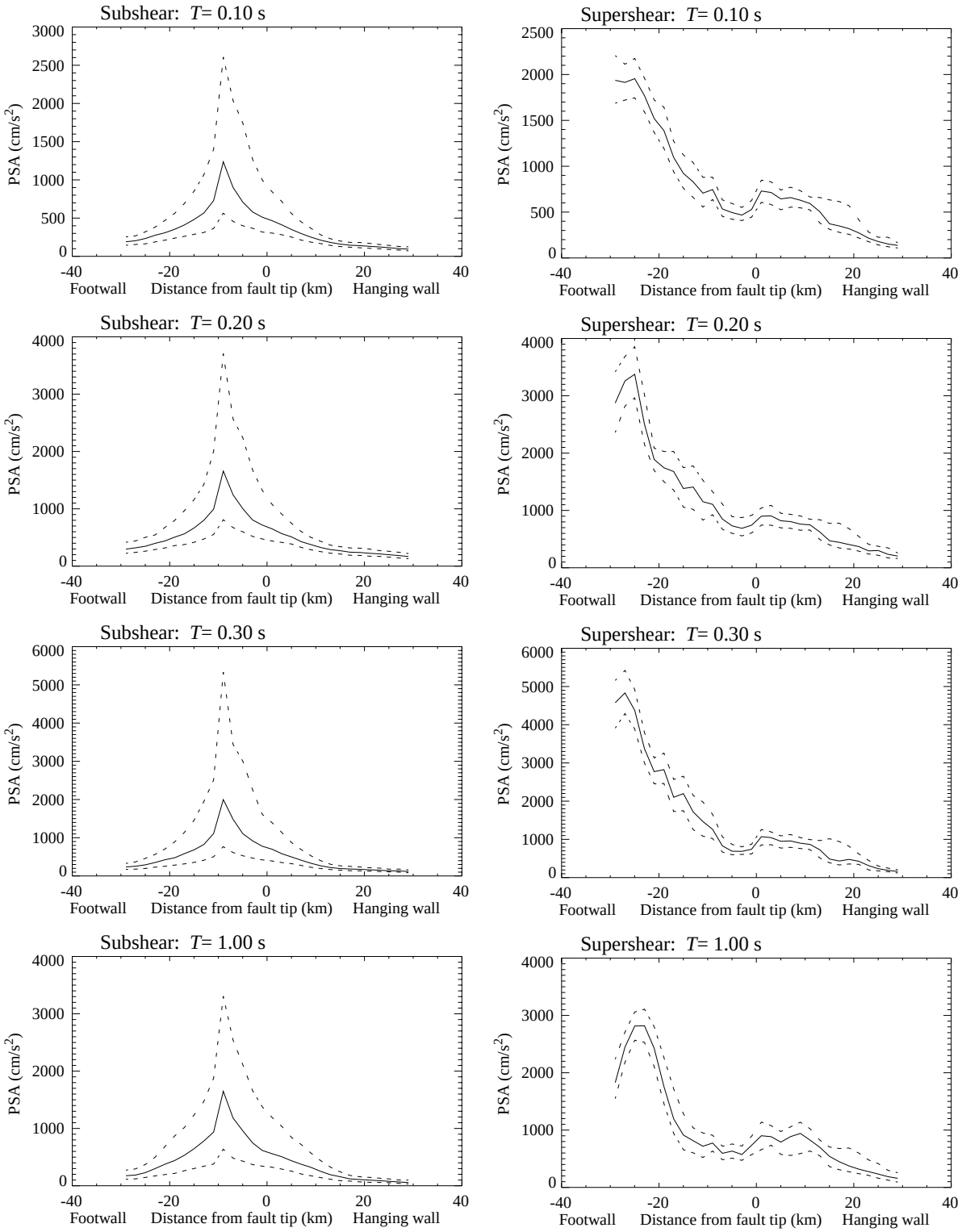

Figure 5. Thrust-faulting PSA spectra for four periods as labeled are shown at the left for subshear ruptures velocities and on the right for supershear rupture velocities for a dip profile located over the fault 5 km from the end of the thrust fault. Solid curves are median responses and dashed curves show 16% and 84% simulation quantiles.

The variability of peak ground motions is also a strong function of assumed rupture velocity. For subshear rupture velocities, the standard deviations of the natural logarithms of PSA, $ln(\sigma_{PSA})$, are maximum at the maximum directivity position (0.65 to 0.9) and decrease relatively smoothly to values of 0.25 to 0.4 for sites located more than 10 km from the maximum directivity position toward to both the footwall and hanging wall regions (Figure 6). The substantial variability of rupture directivity for subshear rupture velocities shows that peak ground motions are strongly influenced by effective stress and rupture velocity variability when rupture velocities are confined to the subshear range. Sites located in maximum directive positions aren't necessarily subjected to large peak ground motions, a confluence of factors (high subshear rupture velocities and high effective stresses located updip between hypocenters and directive sites) are required to produce maximum ground motions. Conversely, for supershear rupture velocities, peak ground motions at directive sites are relatively insensitive to effective stress and rise time characteristics, large peak ground motions are mandated by high rupture velocities between the hypocenter and maximum directive sites. Thus, for subshear rupture velocities peak ground motion variability increases with peak ground motions, while for supershear rupture velocities, peak ground motion variability is smallest for sites with the largest peak ground motions and overall peak ground motion variability is less than half of subshear variability (Figure 6). The maximum supershear $ln(\sigma_{PSA})$ values correspond to sites located over the deepest portion of the thrust fault and demonstrate a $ln(\sigma_{PSA})$ sensitivity to details of rupture initiation.

Isochrone analyses provide insights into these results. Isochrones and isochrone slownesses are shown for single realizations of subshear and supershear rupture velocity ground motion simulations for directive site positions (Figure 7). The large peak horizontal accelerations and velocities for the subshear case (Figure 7a and 7b) are produced by large isochrone velocities (> 14 km/s) in a ~40 km^2 region near the top of the fault (Figure 7c) where geometric attenuation is minimized, where $v_r \sim \beta$, and a high-effective-stresses are located. All the radiated energy from this region of the fault arrives at the site in the 15.9 to 16.3 s time window (Figures 7a to 7c). In the supershear rupture velocity case, large peak horizontal accelerations and velocities (Figure 7d and 7e) are produced by large isochrone velocities that persist over a ~100 km^2 region (Figure 7f); all the energy from the high isochrone velocity region arrives at the site in the 18.8 to 19.2 s time window (Figures 7e to 7f). While the supershear directive site is located more than twice as far from most of the fault compared to the subshear directive site and geometric spreading reduces peak amplitudes at the supershear directive site, the much larger region of high-isochrone velocities tends to counteract geometric losses to produce maximum supershear directivity-related amplification of peak ground motion comparable to the subshear directive sites (Figure 5).

For the rock site characteristics used to produce the Green's functions, directivity strongly amplifies peak ground motions to periods of 0.1 s, with strong amplification occurring for periods in the 0.2 to 0.3 s range independent of rupture velocity (Figure 5). Strong short-period directivity is, in part, a result of consistently high values of the radiation pattern between the hypocenter and the site. *SV* radiation pattern coefficients are nearly 1.0 for virtually the entire high-isochrone velocity regions independent of rupture velocity. Consequently, for thrust faulting, the shear-wave radiation pattern does not significantly diminish the total area of large isochrone velocities; for subshear rupture velocities the radiation pattern reduces the area of high isochrone velocities by < 1% and by ~2% for supershear rupture velocities. In contrast, short-period directivity is reduced

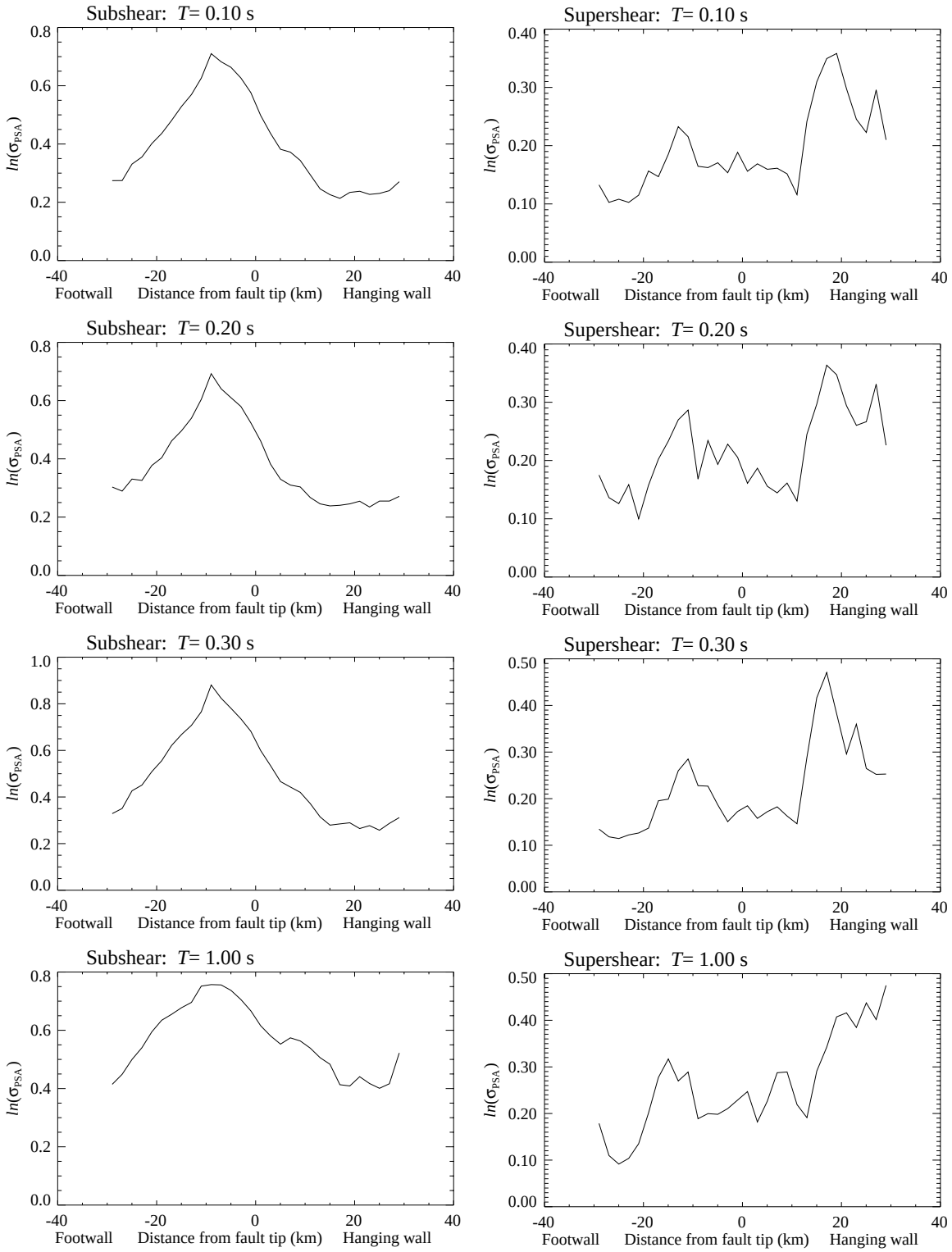

Figure 6. Thrust-faulting standard deviations of the natural logarithms of PSA are shown for subshear rupture velocities on the left and supershear rupture velocities on the right for four periods as labeled for site profiles located over the fault.

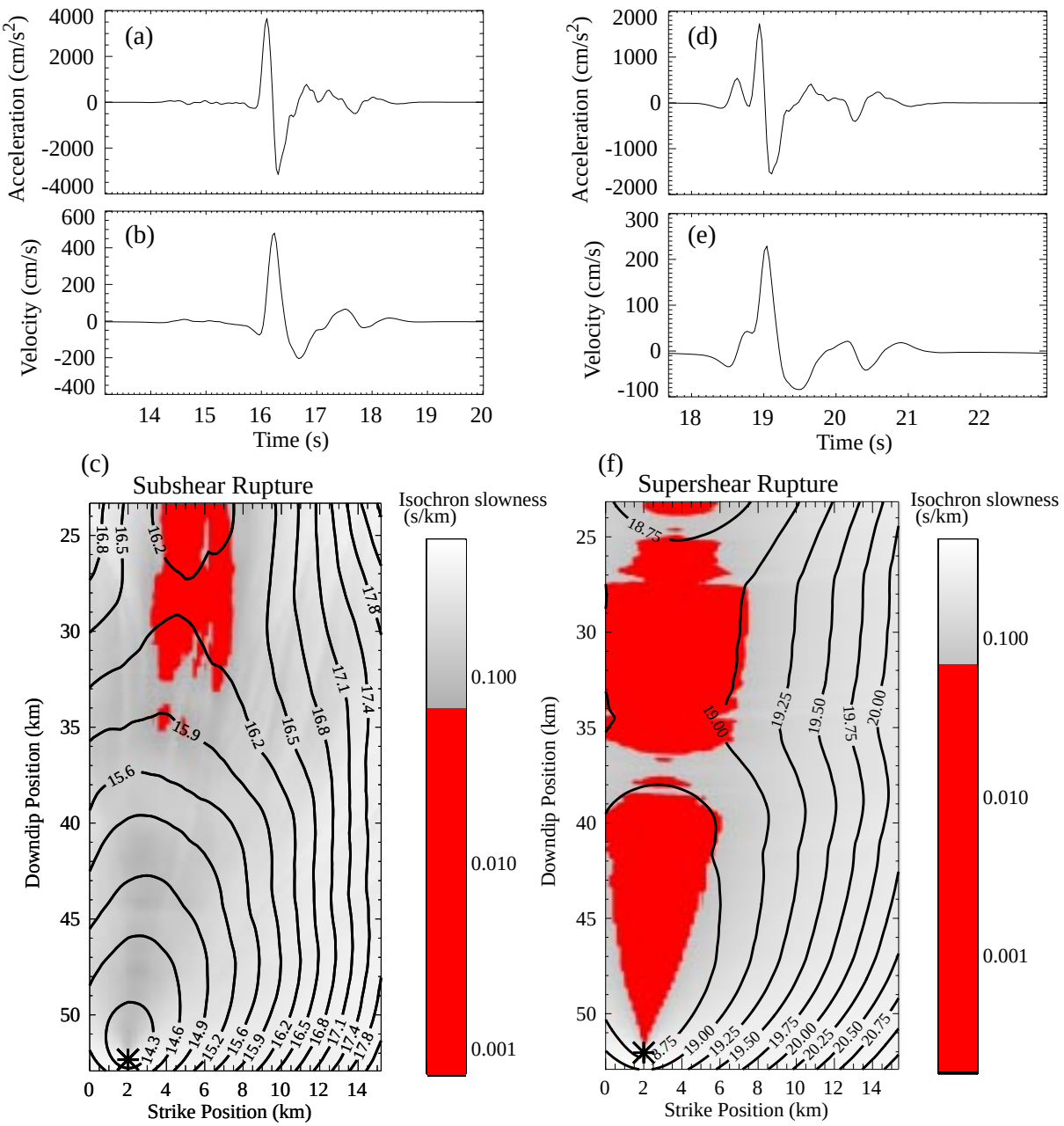

Figure 7. Subshear maximum horizontal acceleration (a) and velocity (b) time histories, and rupture isochrones (labeled contours) and gray-shaded isochrone slowness (c) for a site located 9 km in front of the fault tip. Supershear maximum horizontal acceleration (d) and velocity (e) time histories, and rupture isochrones (labeled contours) and gray-shaded isochrone slowness (f) for a site located 25 km in front of the fault tip. The same stress drop and rise time model was used for both rupture simulations. Isochrone slownesses < 0.07 s/km are shaded red to highlight the maximum isochrone velocity regions. The highest isochrone velocities are updip of the hypocenter in both cases (c,f), but in the supershear case, high isochrone velocities persist over nearly the entire region updip of the hypocenter in the direction of the site.

by the influences of shear-wave radiation patterns for vertical strike-slip faults as discussed in the next section.

The positions of maximum ground motion amplification associated with directivity are substantially different for a 20°-dipping fault relative to faults with dips of 30° and 45° for a buried fault with the fault tip at a 8-km depth. Considering only the case of subshear rupture velocities, for a thrust fault dipping 30°, maximum directivity is produced over a region extending several kilometers toward the footwall side of the fault tip. For the same thrust fault and a dip of 45°, the region of maximum directivity is located several km toward the hanging wall side of the fault tip.

Motivated by large near-fault peak ground motions associated with the 1994 Northridge blind thrust-faulting earthquake, Abrahamson and Silva (1997) produced modified ground motion-attenuation relationships which accounted for thrust-faulting-directivity by introducing a "hanging wall" correction factor and modifying distance definitions to a fault as a function of site position over the surface of a buried fault. Since the Northridge ground motion data are the dominant source of near-fault blind thrust fault ground motion data for M > 6.5 earthquakes used in the development of the Abrahamson and Silva (1997) ground motion relationships, these directivity-related modifications reproduce the observed peak ground motion patterns from the Northridge earthquake quite well. However, the Abrahamson and Silva (1997) "hanging wall" and distance definitions do a poor job of predicting the locations of maximum peak ground motions associated with directivity for a 20°-dipping, blind thrust fault. The problem is that for a 45°-dipping buried fault (similar to Northridge), upper crustal velocity gradients refract direct shear waves that produce maximum directivity toward the hanging-wall-side of the fault tip, but for a 20°-dipping buried fault with the fault tip at depth of 8 km, the region of maximum directivity is located 10 km toward the footwall side of the fault tip. The "hanging wall" correction of Abrahamson and Silva (1997) always predicts that the maximum directivity region will be biased slightly to the hanging wall side of the fault tip. The directivity corrections of Abrahamson and Silva (1997) only really work for buried thrust faults with dips and depths to the top of the fault comparable to the Northridge earthquake. Similarly, the directivity corrections of Somerville et al. (1997) that are based on the cosine of the angle between a fault plane and a site, are not well-suited to account for directivity associated with buried, dipping faults.

Differences Between Dip-Slip and Strike-Slip Directivity: Ground Motion Simulations

We use the thrust-faulting geometry of the previous section and also consider a **M** 6.7 strike-slip earthquake on a vertical fault with rupture occurring between 3 km and 18 km depth for a rupture length of 30 km (Figure 4d). Sensitivity analyses were conducted to find the hypocentral depth ranges that maximized peak ground motions. As a result, hypocenters at depths of 13.8 and 14.8 km where placed 1 km from one end of the fault to maximize peak ground motions. Ground motions were calculated at surface sites located above the fault at distances of 20 km to 39 km along strike to encompass the region of maximum directivity (Figure 4d). At total of 50 effective stress models where combined with the 4 hypocenter positions to generate 100 rupture models and to produce a total of 200 strike-slip faulting ground motions for each position along strike. Only subshear rupture velocity scenarios were considered.

Median peak acceleration and velocity responses of the strike-slip ground motions where about half the median thrust faulting responses for the maximum directivity site positions for the 0.1 to 1.0 s period range (Figure 8). Similar results are obtained for the 84% quantiles; thrust-faulting amplitudes are 2.0 to 2.5 times larger than strike-slip amplitudes (Figure 8). The width of the regions where thrust faulting amplitudes exceed strike-slip responses averaged about 10 km. For a 15 km-long thrust fault, there exists at least a 150 km^2 region were peak ground motions are likely to be substantially larger than maximum strike-slip ground motions. Strike-slip directivity is nearly independent of period for periods < 1 s and produces little amplification of peak ground motions for periods < 1 s (Figure 8) in stark contrast to the strong amplification of peak thrust-faulting ground motions for periods < 1 s (Figure 8).

Isochrone analyses illustrate sources of directivity differences between thrust-faulting and strike-slip faulting ground motions. Large horizontal accelerations and velocities associated with a single strike-slip rupture are shown in Figures 9a and 9b. A long region of high isochrone velocities extends from near the hypocenter to the top of the fault, corresponding to the region of the fault that contributes most of the energy that arrives at the site between 11.8 and 12 s (Figure 9c). For strike-slip faults directivity the *SH* radiation pattern reduces the area of the high-isochrone velocity by 10%, with most of the reduced isochrone velocities concentrated from the upper portions of the fault (Figure 9d). The radiation pattern does not significantly diminish directivity for the thrust faulting simulations. Maximum radiation pattern extending to the top of the thrust faults allows directivity to approach the free surface as discussed in O'Connell (1999c), or to the top of the fault for buried faults (Figure 7). This means that strike-slip directivity is limited by geometric spreading. Consequently, a shallow hypocenter and large shallow-slip velocities are required to maximize strike-slip directivity.

The systematic differences in peak ground motions between strike-slip and thrust faults can also be attributed to the difference in aspect ratios and dimensions of the high isochrone velocity regions between strike-slip and dip slip faults. Summarizing many studies of earthquake rupture properties, Somerville et al. (1999) showed that asperities (regions of high slip velocity) typically have low aspect ratios (are roughly circular) and diameters of several km to < 10 km (diameters slowly increase with magnitude). They found that the distribution of slip on a fault was approximately self-similar, consistent with theoretical predictions of Andrews (1981) and Frankel (1991) that slip-velocity distributions on faults follow a k_r^{-1} scaling law.

Thrust-faulting high-isochrone-velocity regions tend to have the same shapes and dimensions as asperities (roughly circular or elliptical with small aspect ratios; see Figure 7, see also O'Connell, 1999a). When high-slip-velocity asperities and high-isochrone-velocity regions coincide updip of hypocenters of thrust faults, extreme peak ground motions are produced (Figure 5, O'Connell, 1999a). The high-isochrone-velocity regions of strike-slip faults are long and thin (> 20 km), which exceed the dimensions of single asperities. Consequently, a strike-slip fault must find a way to intersect multiple asperities along strike distances of > 20 km to match the source contribution to directivity associated with dip-slip faults. Thus, the self-similar characteristics of fault slip reduce the probabilities of a strike-slip fault experiencing coinciding high slip-velocity and high-isochron-velocity regions comparable to dip slip faults. However, since Mai and Beroza (2000) showed that self-similar slip relations may break down for large strike-slip earthquakes.

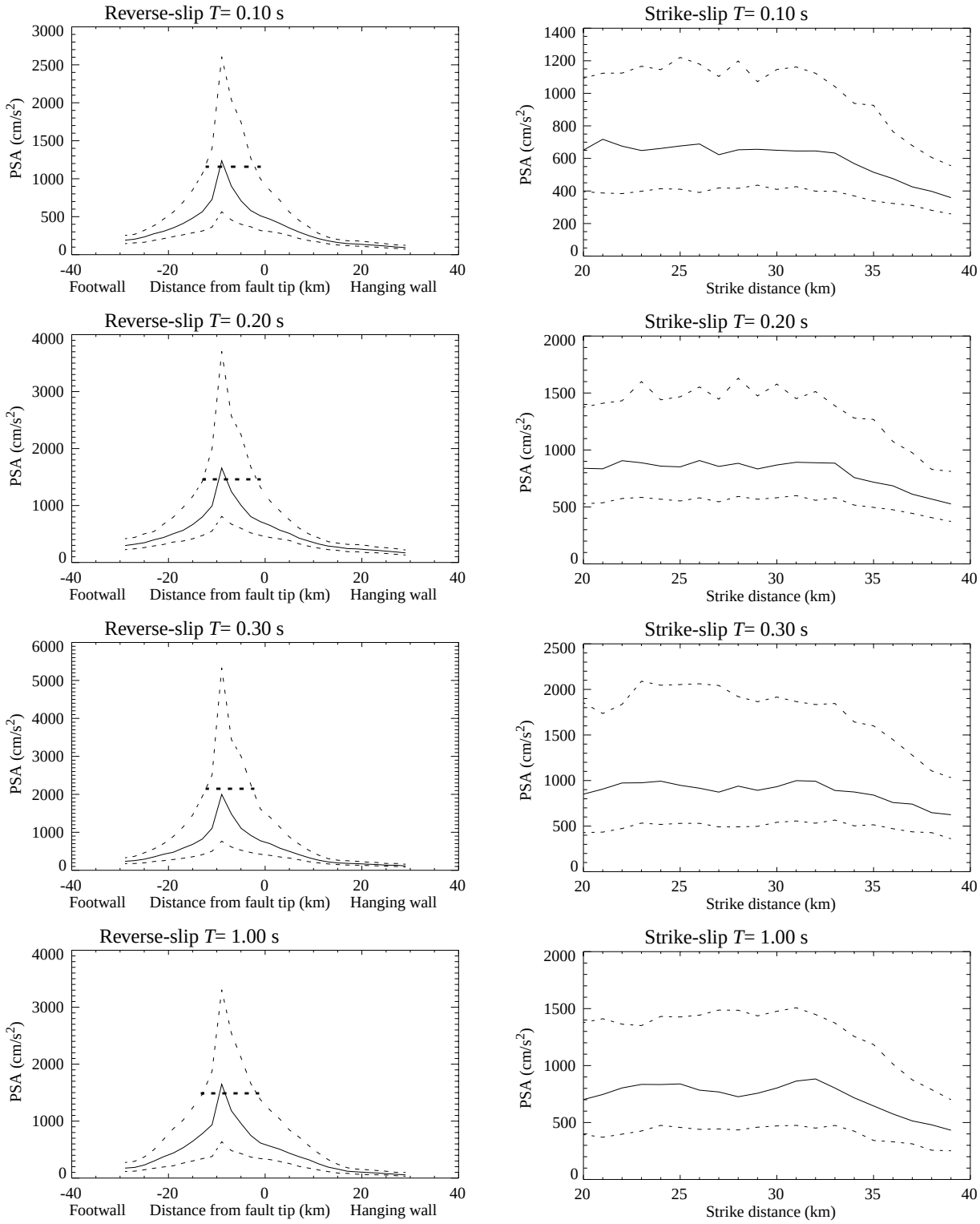

Figure 8. PSA responses for four periods as labeled are shown at the left for thrust fault site profiles orthogonal to strike (dotted horizontal lines show region where sub 84% quantile thrust-faulting amplitudes exceed strike-slip 84% quantile amplitudes) and on the right for strike-slip fault profiles for sites located above the fault at the far end of the fault from the hypocenter. Solid curves are median responses and dashed curves show 16% and 84% simulation quantiles.

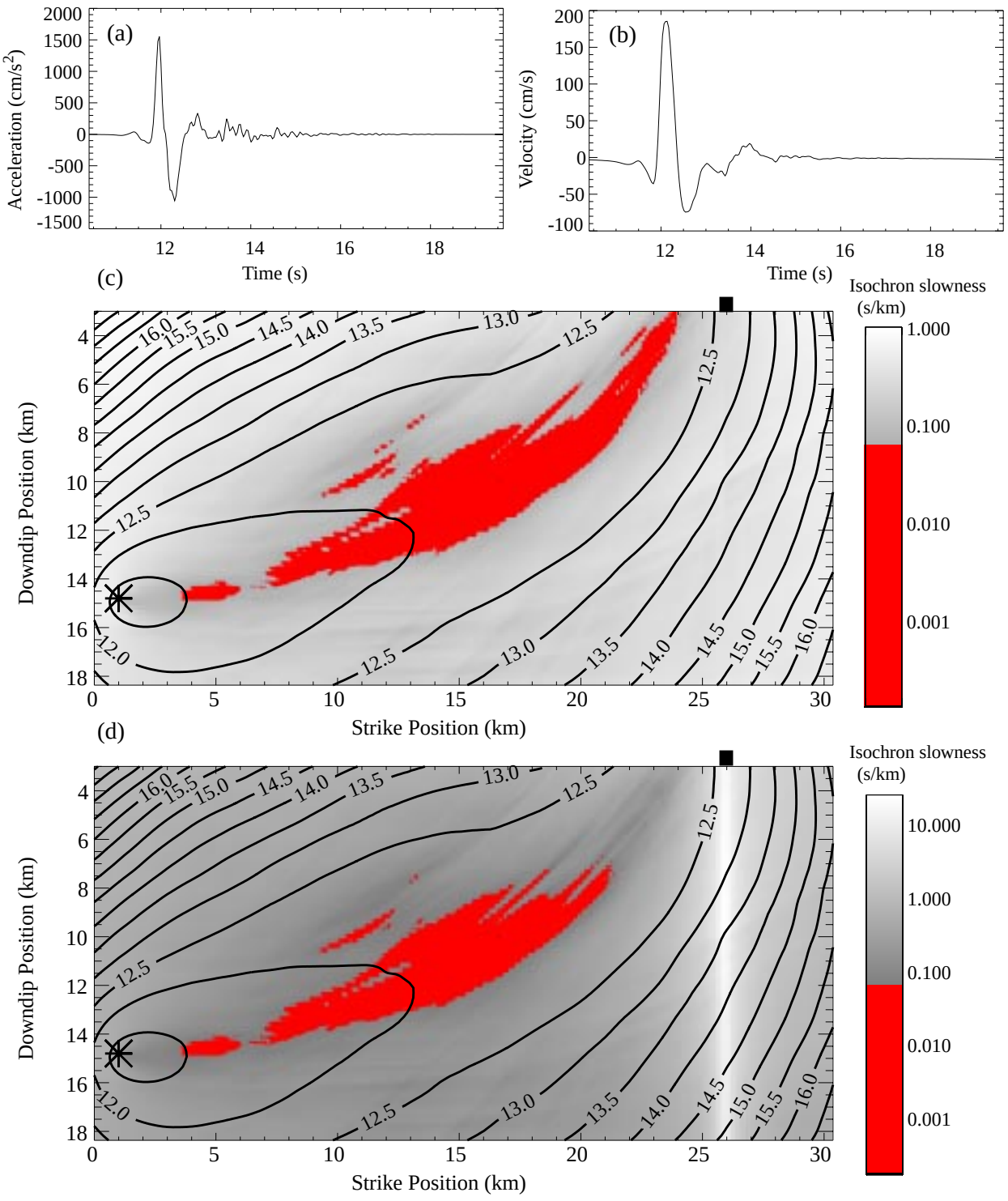

Figure 9. Strike-slip maximum horizontal acceleration (a) and velocity (b) time histories, and rupture isochrones (labeled contours) and gray-shaded isochrone slowness (c) for a site located at a strike position of 26 km (filled square). The hypocenter is the star in (c) and (d). Isochrone slownesses are corrected for the *SH* radiation pattern in (d). Isochrone slownesses < 0.07 s/km are shaded red to highlight the maximum isochrone velocity regions.

the probability that long high-isochrone-velocity regions would overlap high-slip velocities may increase with magnitude for strike-slip earthquakes.

Crustal velocity heterogeneity also reduces strike-slip directivity relative to dip-slip directivity, particularly at short periods. O'Connell (1999a) showed that the interaction between asperity shapes and correlated-random upper-crustal velocity variations allow wave propagation to influence the scaling of peak ground motions. As asperity dimensions increase, the cross-sectional area of shear-wave paths through the upper crust to a particular site that originate from the asperity increases. As shear-wave path separations increase, they begin to exceed the correlation lengths of crustal velocity variations. Summation of direct shear-waves from increasingly separated shear-wave paths becomes progressively less constructive, reducing peak ground motions as frequencies increase for fixed correlation lengths (O'Connell, 1999a). Hutchings and Wu (1990) showed that high phase coherence was only preserved for small earthquakes separated by no more than several kilometers. Consequently, strike-slip high-frequency directivity is reduced relative to dip-slip faults because shear-waves in high-isochrone-velocity regions must sum over shear-wave cross sectional dimensions that exceed crustal velocity correlations lengths of 5-10 km (Frankel and Clayton, 1986) and the dimensions of maximum phase coherence between Green's functions (Hutchings and Wu, 1990).

These results suggest that strike-slip directivity is muted by correlated-random earthquake rupture and wave propagation processes relative to dip-slip directivity. Oglesby et al. (1998; 2000) showed that fault dip and rake fundamentally change the dynamic of earthquake rupture relative to vertical-strike-slip faulting. The broken symmetry of non-vertical faults results in dynamic interactions of normal and shear stresses that are a function of rake. Dynamic earthquake rupture simulations suggest that thrust-faulting slip-velocities are systematically larger than normal-faulting slip velocities. These effects were not included in the simulations of ground motions presented here, but point to another factor that would tend to systematically increase directivity associated with thrust-faulting. Although the ground motion simulations presented here only account for correlated-random kinematic rupture variations and correlated-random wave propagation processes in a limited statistical fashion, they demonstrate that strike-slip directivity is systematically low than dip-slip directivity, that dip-slip directivity is much larger than strike-slip directivity for frequencies exceeding 1 Hz, and that dip-slip directivity can strongly amplify peak ground motions in the 1-10 Hz frequency band. The results obtained here suggest, that the directivity corrections of Somerville et al. (1997) may substantially underpredict short period directivity associated with dip-slip faulting.

Influence of Phase Assumptions on High-Frequency Directivity

The maximum frequency that directivity amplifies ground motions is dependent on the phase assumptions at short periods and the potential for nonlinear responses of near-surface materials at a site. For this discussion we only consider linear site responses representative of rock sites. For sites located sufficiently far from the source, scattering by velocity heterogeneity is the crust randomizes the phase of body wave arrivals. The difficulty is rigorously quantifying "sufficiently distance" for the frequencies of interest.

When scatterers are considered uncorrelated and randomly distributed, the scattered waves are incoherent, so the phase is neglected, and the scattered wave power is obtained as a sum of power from individual scattered waves (Sato and Fehler, 1998). The phase cannot be neglected in correlated random media because such media generate caustics (White et al., 1988; Spetzler and Snieder, 2001). Amplification associated with triplications are lagged relative to the ballistic wavefield due to causality (Brown and Tappert, 1986; Spetzler and Snieder, 2001). For 3D Gaussian random media, Brown and Tappert (1986) and Spetzler and Snieder (2001) showed that caustics will not develop until the propagation distance, L, exceeds the correlation length; i.e. $L/a >> 1$. The relationship to determine the minimum distance require for caustics to develop from Spetzler and Snieder (2001) is

$$\frac{L}{a} \geq 1.12\varepsilon^{-2/3} \tag{15}$$

where ε is the root-mean-square value of the relative slowness perturbations. The situation for self-similar random media is more complicated because the self-similar random media is rich in short wavelength components compared to a Gaussian random media. Consequently, in self-similar random media caustics can develop at increasingly shorter propagation distances as frequency increases. As L becomes large, the phase perturbations associated with propagation in the vicinity of an increasingly large number of caustics, will tend to randomize the phase of shear waves.

For correlated-random media shear-wave caustics begin to form after propagation distances of 2-4 km for frequencies of 1 to 10 Hz (O'Connell, 1999a, cover figure). The point is that for distances not substantially larger than L, the random phase assumption could be a big mistake since in reality, direct shear-waves may be strongly phase coherent at relatively high frequencies. Random phase assumption may produce significant ground motion prediction errors close to faults. O'Connell (1999a) showed that upper crustal random velocity variations can substantially influence the scaling and dispersion of peak ground motions using n=2 in (10), with peak ground motions amplification decreasing for frequencies > 1 Hz as rupture dimension increased. Thus, scattering could produce an apparent nonlinear effect on high-frequency ground motions. Subsequent investigations using n=3 in (10) produced similar results to O'Connell (1999a).

Deterministic 1D and 3D crustal velocity models used to generate $g_{kij}(t)$ do not contain the influences of random 3D velocity heterogeneity known to exist throughout the crust. Completely stochastic phase methods do not account for phase coherence of direct shear-waves. For all media $L \sim 1/\varepsilon$, but as n decreases, L decreases with increasing frequency. This means that as n decreases, the random phase assumption improves at decreasing distances. However, if your earthquake and site happen to be located in a region where n is larger and the site is located close to a dip-slip fault, random phase may be a catastrophic assumption for near-source ground motion estimation.

The ground motion simulations for **M** 6.7 blind thrust and strike-slip earthquakes are repeated with modifications to the rock response Green's functions to increase the randomization of phase at high frequencies to ascertain the potential impacts of phase assumptions on estimated amplifications associated with directivity as a function of frequency. The original Green's

function contained the frequency-dependent phase distortion produced by vertical shear-wave propagation through ~9 km of crust containing self-similar random velocity heterogeneities with a=2.5 km, ε = 5% and n=3 in (10). Phase distortion or randomization at high frequencies may be stronger for lower-velocity sites than the rock site velocity profile in Figure 4c because the mean free path becomes progressively longer for high frequencies. For the purposes of illustration, the Green's function used to calculate ground motions in the previous sections were randomized for frequencies > 3 Hz using the following approach to investigate the influence of increasing high-frequency phase randomization on peak ground motions. A phase shift scaling factor was selected at random for each Green's function. Positive and negative Hilbert transforms of the Green's function were used to represent -90° to +90° phase shifts with the phase shifts progressively applied in the frequency domain between 1 Hz and 3 Hz using a Hanning taper; frequencies < 1 Hz had maximum phase shifts of ±4.5° and frequencies > 3 Hz had maximum phase shifts of ±90°. In these simulations, the phase assumptions are independent of distance. This is obviously not what we expect in the real world, based on this discussion above, but it provides a means to compare and contrast ground motion predictions based on fixed phase assumptions. Ground motions were calculated at the site positions subjected to maximum subshear rupture velocity directivity for each style of faulting.

Simulation results are essentially independent of focal mechanism (Figure 10). Peak accelerations and velocities were reduced by about a factor of two using the phase randomized Green's function relative to the rock site Green's functions for all periods < 1 s (Figure 10). This does not reflect the total amplitude variation associated with all plausible phase assumptions. The rock site Green's functions contain random variations associated with self-similar crustal velocity heterogeneity (n=3 in 10). Rock site responses when n > 3 in (10) will produce less phase randomization at particular distances, and produce larger peak ground motions than shown in Figure 10.

Zeng (1995) added scattered waves into Green's function by shaping the wavetrain of scattered wavelets produced by randomly distributed heterogeneities with an energy envelope function calculated using the scattering energy equation of Zeng et al. (1991). This method does not account for the phase effects of correlated velocity heterogeneity. Since the largest peak ground motions are produced by minimizing phase dispersion as a function of frequency, the scattering approximation of Zeng (1995) does not provide a means to quantify peak ground motions associated with directivity. This problem is not unique to the approach of Zeng (1995), but is universal. Ground motion prediction at sites with critical points (strong directivity) is highly uncertain because the phase variations associated with scattering, attenuation (dispersion), and potential diffraction at the source (Madariaga, 1977; Boatwright, 1982; Fukuyama and Madariaga, 1995) determine peak ground motion amplitudes. However, as r becomes large, the influence of scattering reduces to a well-behaved statistical process (Sato and Fehler, 1998).

Boore and Joyner (1978) and Joyner (1991) showed that variable rupture velocities do not substantially reduce directivity. Spudich and Frazer (1984) and Spudich and Oppenheimer (1986) showed that completely homogenous rupture produces no accelerations. The fractal slip models of Herrero and Bernard (1994) and Somerville et al. (1999) are intrinsically heterogeneous and thus predict that accelerations will be nonzero. The results in Figures 5 and 10 show that directivity can strongly amplify high-frequency ground motions. High-frequency directivity is muted by the assumption of band-limited white noise as a cumulative propagation model.

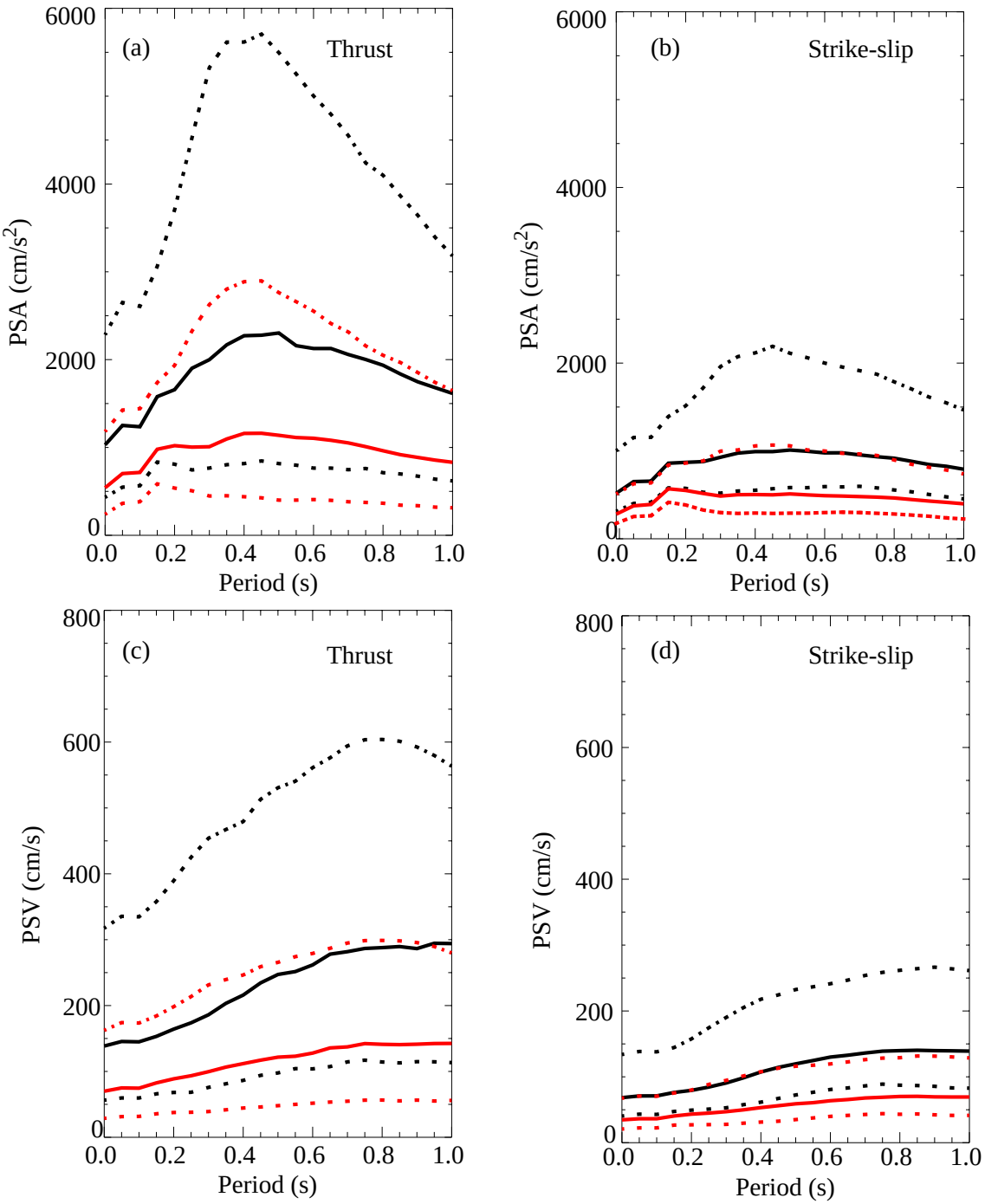

Figure 10. PSA for thrust (a) and strike-slip (b) maximum directivity sites for using 3D fractal media Green's functions (black curves; 16th and 84th quantiles are dashed) and the same Green's functions with phase randomized for frequencies of 3 Hz (0.33 s) and higher (red curves; 16th and 84th quantiles are dashed). Corresponding pseudo-velocity responses (PSV) are shown in (c) and (d).

Schneider et al. (1993) invoke *a priori* assumptions of random phase (BLWN-RVT) to account for phase dispersion associated with wave propagation. However, the random phase assumptions may be inappropriate at rock sites. Peak horizontal accelerations > 1400 cm/s^2 were observed at the Cape Mendocino rock site from the 1992 M 7.0 Petrolia earthquake (Oglesby and Archuleta, 1997) and > 2000 cm/s^2 at Site 1 from the 1985 Nahanni earthquake (Weichert et al., 1986), both thrust faulting earthquakes.

The high-frequency phase characteristics of crustal wave propagation are dependent on the characteristics of correlated-random velocity variations. For instance, Obara and Sato (1995) found profound regional differences in scattering behavior in Japan and showed that regional differences in random velocity characteristics could produce observed shear-wave envelope duration variations. They showed that for exponential media with rough short-wavelength velocity variations, shear-wave time dispersion increases with increasing frequency. In contrast, for smoother Gaussian media shear-wave envelope broadening is independent of frequency. Gaussian media would produce less shear-wave dispersion that considered here. Although the results presented in Figure 10 are based on rather simply assumptions, they show that without knowledge of the influence of crustal scattering on shear wave dispersion, it is not possible to make strong statements about the scaling of peak ground motions for sites close to faults; uncertainties in absolute scaling for rock sites can be a factor of two or more. The common practice of using band-limited white noise to approximate high-frequency Green's function may be inappropriate for sites close to faults, because for moderately heterogeneous crustal velocity structures, high-frequency shear-wave phases may not be significantly randomized in the 1 to 10 Hz frequency band for short propagation paths.

Directivity Biases in 3D Velocity Structures: Strike-Slip Faulting Adjacent to a Basin

Strike-slip faults can juxtapose high-velocity terrains and low-velocity terrains, such as sedimentary basins. In fault-bounded basins, rupture directivity can constructively interact with basin-edge waves to produce extended zones of extreme ground motions that extend away from the fault (Kawase, 1996; Pitarka et al., 1998). Basin-edge waves can be composed of both body and surface waves (Spudich and Iada, 1993; Frankel et al., 2001) which provides a rich wavefield for constructive interference phenomena over a broad frequency range. For instance, the interaction of basin-edge waves and direct shear waves propagating through a low-velocity shallow basin (< 2 km thick) probably produced the nearly linear, strike-parallel zone of severe damage located about 1 km away from the fault in the 1995 **M** 6.9 Hyogo-Nanbu (Kobe), Japan, earthquake (Kawase, 1996; Pitarka et al., 1998). Amplification associated with basin-edge-induced waves can complicate site responses and produce substantial amplification for frequencies < 5 Hz (Field, 1996). It is important to determine if a sites located on the lower velocity side of a strike-slip fault are susceptible to interactions of rupture directivity with 3D velocity structure that could produce ground motion amplification.

Basins come in a variety of scales. Low-velocity basin sediments can extend to depths exceeding 5 to 8 km (Godfrey et al., 1997; Magistrale et al., 2000; Fuis et al., 2001). The distance from a strike-slip fault where basin-edge waves will constructively interfere with direct shear waves is proportional to the basin thickness and inversely proportional to the basin shear-wave velocities. Thus, the largest peak ground motions on the basin side of a strike-slip fault may be located

several km from the fault. To illustrate this effect for a deep and elongated basin, ground motions were calculated for a **M** 7.0 strike-slip earthquake on the Ortigalita fault in central California (Figure 11a) using 3D elastic finite differences (Graves, 1996). This vertical fault is the contact between low-velocity sediments of the Great Valley ancient fore-arc syncline, which extend to depths of ~7 km beneath the Central Valley of California, and higher-velocity Franciscan Diablo range rocks to the west (Zoback and Wentworth, 1986). The Great Valley sedimentary rocks are uplifted and tilted, producing strong horizontal and vertical velocity gradients to the east of the fault (Figures 11b and 11c). A fairly simple rupture model was used with uniform rise times of 1s and smooth variations of slip on the fault. Ground motions were simulated to a maximum frequency of 1 Hz.

Although the faulting scenario is fairly simplistic, it illustrates systematic spatial biases of peak horizontal velocities relative to the fault. Unilateral rupture to the south produces a zone of peak horizontal velocity associated with rupture directivity that extends progressively further east from the fault toward the southern end of the fault, with maximum peak horizontal velocities occurring > 5 km from the fault near the southern end of the fault (Figures 11a and 11d). Fault parallel peak horizontal velocities were small on the fast (west) side of the fault as expected in an isotropic 1D velocity structure, but became large on the slow (east) side of the fault (Figure 11d). It is important to note that these large fault-parallel peak velocities are produced using a purely isotropic velocity model. This simulation shows that complicated shear-wave polarizations can be produced in 3D velocity structures which contain strong horizontal and vertical velocity gradients. This is one type of situation where the directivity corrections of Somerville et al. (1997) for periods of 0.6 s and longer, particularly for the proportion of fault-normal versus fault-parallel ground motions, are unlikely to provide realistic ground motion estimates. Recent experience, and the simulation presented here, clearly shows that knowledge of first-order larger-scale 3D crustal velocity is necessary to ascertain the potential for systematic amplification of ground motions in ground motion investigations.

Long-Duration Large Amplitude Interface Modes In Low-Velocity Sedimentary Basins

Lomnitz et al. (1999) showed that long duration monochromatic ground motions may be produced in basin that have low shear-wave velocities (0.1 to 0.2 km/s) and saturated sediments. To test the ability of such a mode to persist in a basin with strong intrinsic attenuation, a model of a small (0.3 km wide and 0.1 km deep), glacial scour is embedded in a 2D model with slightly higher shallow velocities outside the basin and higher velocities at depth (Figure 12a). Values of Q=10 were used to simulate high-intrinsic attenuation in the near-surface, low-velocity materials. Compressional wave velocities were set to water velocities for the lowest velocity materials. The 2D version of the elastic finite-difference program E3D (Larsen and Grieger, 1998), which includes viscoelastic capabilities implemented using the approach of Robertsson et al. (1994), was used to calculate the seismic response of a *SV* plane-wave incident at 5° from vertical upon the basin with a total moment of 10^{20} dyne-cm. The numerical model was 8 km long and 5 km deep with attenuating boundaries to minimize spurious internal reflections. The source-time function was a differentiated 0.75s-duration Gaussian pulse. The incident horizontal velocity response is shown at the bottom of Figure 12b.

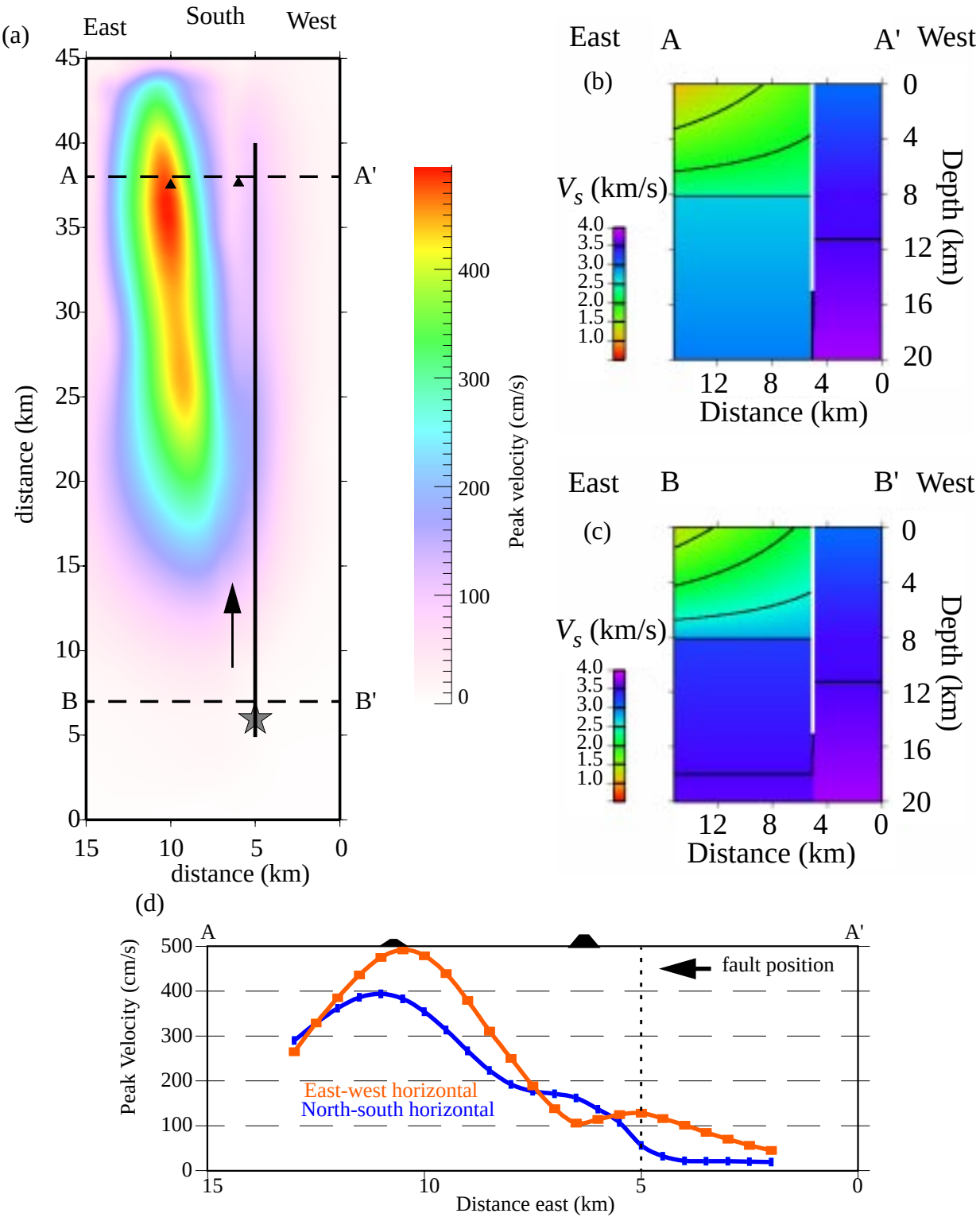

Figure 11. Plan view of fault geometry (a), the shaded-star is the epicenter, the arrow shows the direction of rupture propagation, the solid line is the surface location of the Ortigalita fault, dashed-lines are positions of shear velocity-depth cross sections shown in (b) and (c). Triangles are dam sites. Peak horizontal velocity is color-shaded in (a) and for both horizontal component for profile A-A' in (d).

Constructive interference at the center of the basin produces maximum amplitudes that persist for ~7 s and a slow amplitude decay lasting about 20 s (Figure 12b). Sites offset from the center of the basin experienced long-duration monochromatic horizontal motions with slowly decaying amplitudes that persisted to the maximum calculation time of 60 s. The long duration response are produced by the interface modes propagating horizontally back and forth across the basin as they reflect off the vertical boundaries at the basin edges (Figure 12c). Ground motion responses similar to the top time history in Figure 12b were observed for a **M** 3.7 earthquake recorded in very low-shear wave velocity sites near Jackson Lake, Wyoming. This mode can persist for long durations with little attenuation, even though intrinsic attenuation is high.

A difficult problem is determining how nonlinear soil responses would complicate the response shown in Figures 12b and 12c. Nonlinear soil responses may significantly alter and reduce surface responses when modulus degradation and damping are the dominant modes of nonlinear soil responses (Zhang and Papageorgiou, 1996). When, dynamic pore-pressure-coupled dilative-contractive mechanisms dominate nonlinear soil responses (Bonilla, 2000), interface modes may indeed produce a recipe for disaster by extending the durations over which energy is pumped into near-surface low-velocity basin materials. Lomnitz et al. (1999) show several observations of monochromatic wavetrains persisting for several minutes at sites located in Mexico City. The range of behaviors that can be produced by the interactions of various types of nonlinear soil responses with long-duration large amplitude interface modes is yet to be discovered.

BALANCED ROCKS, ROCK SITE RESPONSES, AND THE HAZARDS OF PEAK GROUND MOTION UNCERTAINTY BIASES

Rodriguez-Marek et al. (2001) expanded site classification to include both a stiffness (shear-velocity) classification and depth to bedrock rating system. They found that peak ground motions and ground motion uncertainties are significantly lower (~30%) for unweathered California rock cases where shear-wave velocities exceeded 760 m/s or depth of soil above 760 m/s material was < 6 m relative to the most-commonly used attenuation-relations (e.g. Abrahamson and Silva, 1997; Sadigh et al., 1997). They also found that deep, stiff-soil site peak ground motions uncertainties are substantially lower than those from the most-commonly used attenuation-relations (e.g. Abrahamson and Silva, 1997; Sadigh et al., 1997) that lump all deep soil sites into a single site class. However, weathered/soft rock and shallow and intermediate depth sites had spectra peak amplitudes and standard errors comparable to the relations of Abrahamson and Silva (1997) and Sadigh et al. (1997).

These results have several implications. Anderson and Brune (1999) suggest that the existence of balanced rocks in the vicinity of faults in the western U.S. indicates that probabilistic seismic hazard assessments overestimate ground motions. Abbott and Louie (2000) showed that 30-meter-averaged shear-wave velocities at balanced rock sites average 1000 m/s to 1500 m/s. The results of Rodriguez-Marek et al. (2001) show that not only are peak motions likely to bias substantially lower at such sites, but that the expected variation of peak ground motions is much lower also. LaForge et al. (1999) showed that by simply accounting for deamplification at rock sites, but retaining the large empirical ground motion uncertainties associated with stiff soil sites,

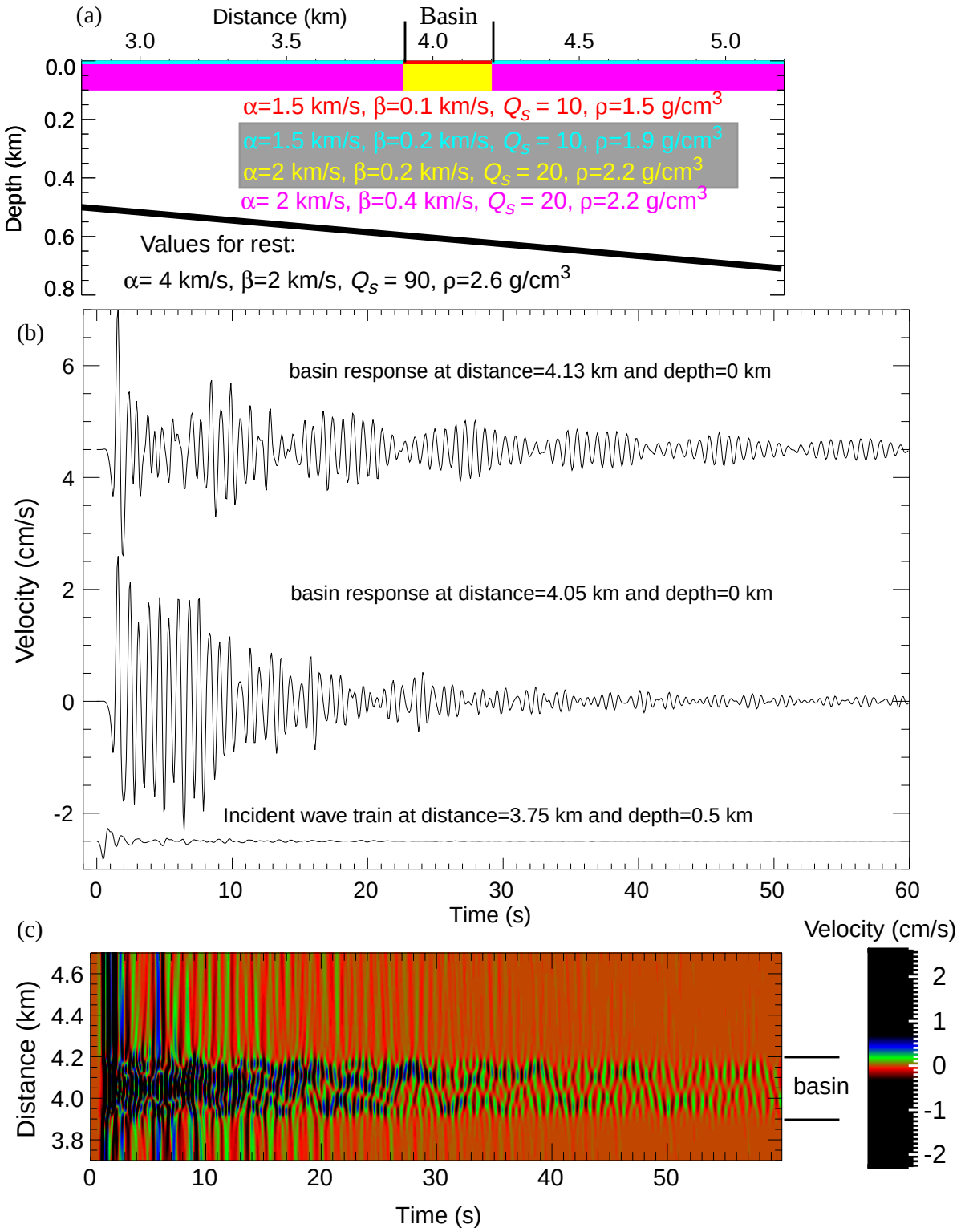

Figure 12. Color-coded velocity structure (a) with the thick line showing the incident *SV* plane wave. The incident waveform at a depth of 0.5 km modified by internal reverberations is shown at the bottom of (b) along with two surface waveforms from sites located within the basin as labeled. Color-coded horizontal velocity time histories for surface sites located at distances from 3.7 km to 4.7 km (c).

probabilistic peak ground motion estimates for rock sites were substantially reduced, even for small annual exceedence probabilities. Incorporating the reduced peak ground motion uncertainties at rock sites found by Rodriguez-Marek et al. (2001) may show that there are no discrepancies between probabilistic seismic hazard estimates for typical (non rock) sites and the existence of balanced rocks at rock sites in the vicinity of faults. Shallow stiff soil/weathered rock sites are most prevalent in California urban environments and Rodriguez-Marek et al. (2001) indicate that these sites have the maximum ground motion uncertainties. In contrast, deep soil sites have lower ground motion uncertainties, and it is possible that probabilistic seismic hazard analyses that use peak motion attenuation relationships such as Abrahamson and Silva (1997) and Sadigh et al. (1997) may overstate probabilistic seismic hazards for deep soil sites because the ground motion uncertainties for deep soil sites may be overestimated in these relationships by 25% to 50% (Rodriguez-Marek et al., 2001).

Balanced rocks are located on the high-velocity side of faults in Brune (1999, 2000). The northeast side of the San Andreas fault, where the balanced rocks are located (Brune, 1999), is the high velocity side of the fault (Lutter et al., 1999; Fuis et al., 2001). Strongly asymmetric velocity structures adjacent to faults may decrease the relevance of balanced rock ground motion inferences for sites not located in locally high-velocity terrains. The balanced rocks in Brune (1999) are located > 14 km from the trace of the San Andreas fault. In the strike-slip ground motion simulation, the peak velocities decay rapidly on the high-velocity side of the strike slip fault over a distance of < 5 km (Figure 11c). Consequently, ground motion inferences from the northeast side of the San Andreas fault may dramatically underestimate ground motion hazards on the southwest side of the fault. For dipping dip-slip faults, the region of maximum ground motion amplification moves progressively away from the fault trace onto the hanging wall as fault dip increases when vertical velocity gradients are present (Figure 5 and O'Connell, 1998). As noted in Brune (2000), the hanging wall of normal faults typically consists of sedimentary fill (low-velocity material) and the footwall typically consists of high-velocity rocks that provide a source of balanced rocks. This type of 3D velocity asymmetry between hanging wall and footwall sides of normal faults is likely to increase amplification on the hanging wall (basin) side of the fault and deamplify ground motions on the footwall (rock) side of the fault. It is premature to draw conclusions about normal faulting ground motions based on observations that may be substantially biased toward small peak ground motions by systematic 3D velocity variations typical of normal faulting environments.

Balanced rocks are associated with the stiffest (most erosion-resistant) rocks in their neighborhoods. O'Connell (2000) showed that correlated-random 3D velocity heterogeneity averaged over the top 0.1 km strongly influence peak accelerations for rock sites. Rock sites with 0.1 km average velocities 10% higher than the mean velocity had median peak accelerations 1.7 times less than rock sites with 0.1 km average velocities 10% lower than mean rock velocities. Given the substantial influence 3D velocity structure can have on directivity and site response, to understand the relevance of balanced rock observations to ground motion estimation at non rock sites, it will be necessary to quantitatively evaluate the influence of 3D velocity structure on rock site responses and to measure the 3D velocity structure in the vicinity of balanced rocks. There are also the difficult issues of not knowing the prior population of balanced rocks and the strongly nonlinear aspects of toppling behavior for earthquake ground motions (Yim et al., 1980; Makris et al., 1999).

VALIDATION OF GROUND MOTION ESTIMATES

The confidence that can be placed in any ground motion estimation model is proportional to the physical realism and observational support for the components of the model. Research into earthquake rupture dynamics, wave propagation, and nonlinear soil response suggests that our knowledge of the physics associated with these processes is substantially incomplete. Current ground motion estimation models rely on phenomenological assumptions to overcome gaps in knowledge. The confidence in these models tends to scale as r/f. That is, far enough from the earthquake source, high-frequency peak ground motions mostly conform to the behavior predicted by Hanks and McGuire (1981) and Boore (1983) using random vibration theory with point source approximations. As discussed previously, there are physical factors that can undermine these far-field assumptions like critical Moho reflections, line sources, and regions with low crustal scattering. Thus, it is essential to form a physical understanding of the physics supporting simplified approaches to understand when they don't apply at a particular site.

There are two types of uncertainty in site-specific ground motion estimation: epistemic and aleatory (Toro et al., 1997). Epistemic uncertainties describe incomplete knowledge and observations of the earthquake source and wave propagation physics. Aleatory uncertainties are the inherently unpredictable aspects of earthquakes, such as the specific pattern of stress release that will occur during a future earthquake. In principle, additional data and physical understanding can reduce epistemic uncertainties, but there is generally a coupling between epistemic and aleatory uncertainties. For instance, recent studies have reduced epistemic uncertainties about how 3D velocity structure may strongly influence peak ground motions, but limited 3D velocity information in most regions of the world produce unchanging aleatory uncertainties. The discovery and/or recognition of new physics facilitates sensitivity testing and reduces susceptibity to underestimating epistemic uncertainties, but unchanging aleatory uncertainties place limits on the quantitative predictive value of ground motion simulations. Identification of ground motion uncertainties in terms of epistemic and aleatory factors is useful, but clearly, recent experience suggests that it is probable that there are epistemic uncertainties yet to be discovered.

The fact that many seismic source and propagation factors can never been entirely known produce an open system; any ground motion model is necessarily non-unique (Oreskes, et al., 1994). Thus, precise quantitative site-specific ground motion estimation is not possible. Synthetic ground motion modeling approaches can be constructed that confirm past experience, but the ability of any model to predict future behavior is necessarily limited (Oreskes, et al., 1994). However, ground motion modeling does have substantial heuristic value. Ground motion modeling provides the only means to discern if a site is susceptible to first-order factors that are likely to strongly bias peak ground motions and durations to large or small values relative to experience to date.

"Validation" exercises that require ground motion simulation models to exclusively produce results consistent with observations to-date, are imposing an explicit prior stating that current ground motion observations encompass all possible physical behaviors. Such exercises are not validation. Rather, they simply confirm the ability of a model to reproduce experience, whether or not the model is physically correct (Oreskes et al., 1994). Such "validation" constraints place ground motion estimation models in a limited role as experience interpolation schemes. This is a

counter-productive requirement for site-specific ground motion estimation, particularly for sites close to active faults; a critical role of modeling is to discover potentially significant new behavior beyond the limits of current ground motion experience. Any requirement to exclusively use empirical ground motion information in site-specific ground motion estimation is an exercise in denial, or a spectacular assertion that the future holds no surprises.

Upon consideration of all these source and propagation factors it is clear site-specific ground motion estimation uncertainties can be quite large, particularly, when little is known about seismic sources, crustal velocity structure, and/or local site conditions. While deterministic estimation of site-specific ground motions is not a realistic goal, site-specific ground motion estimation couples naturally with probabilistic seismic hazard assessment (PSHA). A PSHA analysis can incorporate uncertainties and sensitivity analysis results to account for the potentially wide range of source and propagation uncertainties in site-specific ground motion investigations. Ground motion simulations for near-source sites can be used to modify ground motion relations for specific sources in PSHA analyses to account for site-specific biases or tendencies identified in the simulations. One of the most difficult practical and philosophical aspects of the problem is finding a means to incorporate the influences of model unknowns and unanticipated earthquake behavior into a probabilistic description of ground motions without resorting to specifying end-member models as solely representative of site-specific seismic hazards, as suggested by Anderson (2001).

FUTURE DIRECTIONS IN STRONG GROUND MOTION ESTIMATION

Ground motion simulations have relied on simplified assumption and phenomenological statistical descriptions of source and wave propagation processes. That is, statistical descriptions of the seismic outputs of earthquake rupture and wave propagation are frequently used in place of forward modeling with differential equations corresponding to the physics of earthquake rupture and elastic wave propagation. This has been necessary because knowledge to formulate the appropriate differential equations has been sketchy, strong ground motions observations are sparse, knowledge of 3D crustal velocity structure is limited, extreme computation demands have limited sophisticated computational investigations to rare, exotic, and expensive computers, and simplified statistical approaches to specify source and wave propagation for ground motion estimation work well as r/f increases. The development of BLWN-RVT approaches dramatically improved ground motion estimation capabilities for sites not located “too close” to faults. Unfortunately, we don’t know what “too close” is yet in terms of r/f and this issue remains a critical ground motion estimation problem to be solved.

Strong motion estimation will improve as phenomenological approaches are replaced with understanding and observations of source properties, crustal velocity structure, and soil responses in coupled observations-physics based approaches. It will be a significant advance to introduce statistical characterizations of physical parameters, based on observations and understanding, as inputs into differential equations that represent the physics of earthquake sources and linear and nonlinear wave propagation, instead of specifying the outputs of such systems, *a priori*. From a Bayesian perspective, significant progress in ground motion estimation will be represented by an evolution from *a priori* assumptions to *posterior* assurance. Recent advances in inexpensive computer technology (cheap fast microprocessors, inexpensive memory, and parallel processing) make complex calculation computationally possible. Unfortunately, strong ground motion

seismology is now extremely data and knowledge poor relative to current computational capabilities. Improvements in ground motion estimation capabilities are contingent on progress in source characterization, rupture dynamics, wave propagation, nonlinear soil responses, and acquisition of new observations as outlined below in five topics below

Topic 1: Source Characterization

Improved understanding of tectonics, kinematics, distribution of stress, and localization of strain is necessary to quantify faults properties for ground motion estimation. Physical understanding of the factors that promote and inhibit rupture across fault segments and the dynamic interactions between fault segments (Harris and Day, 1993, 1999; Magistrale and Day, 1999) is necessary to estimate earthquake magnitudes and recurrence behaviors. A particularly urgent need are improved methods to detect buried faults.

Topic 2: Dynamic Constraints on Fault Rupture

It is important to note, that the spatial correlations between the source factors listed in Tables 1 and 2 are poorly understood. Currently ground motion estimation methodologies either assume correlation relationships and/or assume that various faulting factors are completely uncorrelated. It is important to develop a physical understanding of the correlations between source factors in Tables 1 and 2.

As summarized in Ben-Zion (2001), theoretical studies have shown that sharp velocity contrasts across faults can produce systematic biases in rupture direction and asymmetries in slip velocities, with amplified slip velocities radiated on the more compliant side of a fault. There may be preferred directions of rupture which will bias probabilities of strong directivity to sites located at a particular end of a fault. Oglesby et al. (1998, 2000) showed that dipping faults also experience asymmetric slip velocities as a function of focal mechanism. These results suggest fundamental problems with symmetric kinematic specification of slip velocities for wide classes of faults and fault zone velocity conditions. For instance, the typical 3D velocity configuration for normal faults of low-velocity sediments on the hanging wall, slip is in the direction of the compliant material for updip ruptures, which would systematically increase slip velocities on the hanging wall and would tend to counteract the systematic reduction of slip velocities on the hanging wall reported for normal faults for homogeneous crustal velocities (Oglesby et al., 1998; 2000). For typical thrust fault velocity structures, where the hanging wall consists of higher velocity rocks than the footwall, updip rupture produces slip in the direction of the stiff material. Rupture dynamics associated with velocity heterogeneity may systematically reduce slip velocities on the hanging wall, which would counteract the tendency for slip velocities to increase on the hanging wall for homogenous crustal velocities reported by Oglesby et al. (1998, 2000). The case when hanging wall velocities are lower than footwall velocities may be catastrophic for sites on the hanging wall: Updip rupture then produces slip in the direction of movement of the compliant material, which increases slip velocities on the hanging wall, and may produce supershear rupture velocities. Combined with the tendency for hanging wall slip velocities to be amplified for dipping thrust faulting (Oglesby et al., 1998, 2000), this these conditions could produce peak ground motions larger than experience to date. These scenarios suggest that it may not be appropriate to use ground motion observations associated with particular styles of faulting as

proxies for other faults with similar styles of faulting when crustal velocity structures in the vicinities of the faults differ.

The fault configurations and fault zone velocity structures investigated to date have been relatively simple (Ben-Zion, 2001). Theoretical rupture investigations to examine the dynamic influences of more general and complex velocity, stress heterogeneities, and segmentation geometries associated with real faults (Harris and Day, 1983; Magistrale and Day, 1999) on slip velocities, rupture velocities, rise times, and stress drops are urgently needed to reduce the potential for substantial ground motion prediction biases and errors associated with epistemic uncertainties. These studies will need to address the coherence of seismic radiation as a function of frequency.

It is vital to determine the physical factors that control rupture velocities. Can supershear rupture velocities persist over asperity dimensions of several km for dip-slip faults? Can supershear rupture velocities persist over large portions of dip-slip faults? Answers to these questions are necessary to estimate the locations and amplitudes of strong ground motions close to faults.

Topic 3: Wave Propagation

A vital area of investigation is to determine the influences of 3D velocity structure on 1 to 10 Hz strong ground motion responses as Davis et al. (2000) have demonstrated. This will require incorporating realistic attenuation in 3D finite-difference schemes, a topic with significant recent progress (Day, 1998). The influences of realistic 3D topography and anisotropy for frequencies > 1 Hz on peak ground motions and polarizations as a function of frequency are not well known and warrant investigation. An urgent need is to determine amplification-frequency responses of basin-edge waves and the spatial locations and extends of amplified ground motion regions in high-population density basins. Similarly, the susceptibility of saturated, low-velocity basins to very-long-duration monochromatic ground motions associated with interface modes is a serious concern.

Quantifying the influence of random velocity heterogeneity on the amplification and phase coherence of shear-waves and surface waves is necessary to determine appropriate Green's function assumptions close to faults. Investigations similar to Hutchings and Wu (1990) are needed in diverse geologic environments to provide empirical constraints on Green's function coherence as a function of source separation distances and propagation distances.

Topic 4: Nonlinear Site Responses

It is important to determine the limits of application of equivalent linear methods that use time-independent nonlinear soil parameters as a function site soil properties. For instance, the number of cycles of motion required to achieve significant modulus degradation is variable. Thus, directivity that produces maximum amplitudes in the initial stages of strong ground shaking may amplify the peak strong motion responses at soil sites in the first several cycles of motion before significant modulus degradation occurs. For structures with saturated foundations, particularly, embankment dams, it is critical to determine the influences of nonlinear effects such as anelasticity, hysteretic behavior, and cyclic degradation due to pore water pressure on the peak ground motions, durations, and frequency responses Soil nonlinearity tends to reduce

high-frequency peak motions, but consideration of pore water pressure influences (Bonilla, 2000) shows that soil nonlinearity can substantially increase durations of shaking and increase peak motions at lower frequencies.

Topic 5: Essential Future Observations

Significant advances in ground motion estimation will require new geologic, geodetic, geotechnical, and geophysical observations. We present a summary of the important data collection activities necessary to produce advances in source characterization, dynamic rupture constraints on fault rupture, crustal wave propagations, and nonlinear site responses. Short-period and broadband seismographic networks, seismic refraction and reflection data, and geologic mapping all provide vital information for characterizing source properties, crustal velocity structure, and site responses. Quantification of ground motion estimation uncertainties for sites in regions lacking such information is difficult (Frankel et al., 1997). The ability to conduct site-specific ground motion investigations is one of the long-term payoffs of investments in seismic monitoring, regional geological and geophysical investigations, and geotechnical engineering.

a) Surface and downhole strong motion instruments and arrays are essential to resolve several issues. Downhole strong motion arrays are needed to understand source dynamics (2) to eliminate the severe signal distortion associated with the top several kilometers of the crust (Ellsworth et al, 2001). Downhole strong motion arrays are required to understand the physics of wave propagation through the top several kilometers of the crust including the influences of complex velocity structure and scattering (3), attenuation (3), and nonlinear soil responses (4) on surface strong ground motions. Surface strong motion arrays are required to understand spatial ground motion variability which has important applications to the engineering analyses of large-scale structures (Harichandran, 1999; Santa-Cruz et al., 2000).

b) Surface and downhole broadband weak motions networks and arrays are required for progress in topics 1-4 above. Small earthquakes occur much more frequently than large earthquakes and provide data essential for investigations into topics 1-3. The seismotectonic problem of source characterization (topic 1) is coupled to the problems of wave propagation (topic 3) and ground motion estimation. The earthquake location and focal mechanism estimation problems of seismotectonics requires recursive estimation of crustal velocity structure based on weak-motion recordings of earthquakes and explosions. Ground motion estimation requires estimate of crustal velocity structure. It is impossible to discern crustal wave propagation properties and velocity structure relevant to the frequency band of engineering interest without network and array broadband recordings of earthquakes and explosions. Small earthquake recordings also provide empirical Green's functions for ground motion estimation.

c) Geologic and geodetic measurements of crustal deformation, deformation rates, and fault slip-rates are required to estimate probabilities of ground motion occurrence.

d) Direct imaging of seismic source and crustal velocity, scattering, and attenuation structure using artificial and earthquake sources with 2D and 3D seismic refraction, reflection, array, and fault zone recording geometries are needed to reveal near-fault velocity structure.

e) Absolute trigger times are often not available for strong motion recordings. Wald et al. (1996) note that the primary factor limiting ultimate resolution of their rupture model for the 1994 **M** 6.7 Northridge earthquake was the lack of absolute timing for many of the strong-motion recordings. The lack of absolute trigger times for the closest stations west of the 1989 **M** 7.0 Loma Prieta earthquake also limited resolution of rupture times (Wald et al., 1991). This persistent characteristic of strong motion recordings impedes efforts to resolve spatial variations of rupture velocities on faults. Deployment of strong motion recorders equipped to record absolute time will substantially advance abilities to infer the dynamic rupture properties of earthquake faulting.

Substantial progress has been made in the past several decades in ground motion estimation capabilities, particular for sites located > 20 km from faults. Ground motion estimation uncertainties will remain difficult to quantify for sites located in the vicinity of faults without significant progress in physical understanding and ground motion observations represented in topics 1-5 above. Difficulties in ground motion uncertainty estimation hamper efforts to develop probabilistic estimates of ground motion hazards and efforts to reduce earthquake risks.

ACKNOWLEDGMENTS

This paper is dedicated to the memory of William Joyner, who generously participated in discussions of directivity, wave propagation, site response, and nonlinear soil response, and who encouraged us to pursue many of the investigations presented here. The authors benefited from helpful discussions with David Boore, Joe Andrews, Paul Spudich, Art Frankel, Dave Perkins, Roland Laforge, Chris Wood, Ralph Archuleta, Fabian Bonilla, David Oglesby, Steve Day, Bruce Bolt, Rob Graves, Roger Denlinger, Bill Foxall, Larry Hutchings, Ned Field, Hiro Kanamori, Dave Wald, and Walt Silva. Rob Graves provided the emod3d finite difference software, Shawn Larson provided the e3d software, and Paul Spudich provided isochrone software. Rob Graves performed most of the calculations shown in Figure 11. Supported by U.S. Bureau of Reclamation Dam Safety Research projects SPVGM and SEIGM.

References

Abbott, R. E., and J. N. Louie, 2000. High shear-wave velocities under precarious rocks might explain their proximity to the San Andreas fault, *EOS* **81**, F821.

Abrahamson, N. A., and R. R. Youngs, 1992. A stable algorithm for regression analysis using the random effects model, *Bull. Seism. Soc. Am.* **82**, 505-510.

Abrahamson, N. A., and K. M. Shedlock, 1997. Overview, *Seism. Res. Lett.* **68**, no. 1, 9-23.

Abrahamson, N. A. and W. J. Silva, 1997. Empirical response spectral attenuation relations for shallow crustal earthquakes, *Seismol. Res. Lett.* **68**, 94-127.

Aki, K., 1968. Seismic displacements near a fault, *J. Geophys. Res.* **78**, 1334-1346.

Aki, K., 1983. Strong-motion seismology, *in* "Earthquakes: Observation, Theory, and Interpretation", H. Kanamori and E. Boschi, eds., Proc. of the Int. School of Physics., Enrico Fermi, North-Holland Pub. Co., Amsterdam, pp.

223-250.

Alex, C. M., and K. B. Olsen, 1998. Lens-effect in Santa Monica?, *Geophys. Res. Lett.* **25**, 3441-3444.

Anderson, J. G., 2001. Precautionary principle: Applications to seismic hazard analysis, *Seism. Res. Lett.* **72**, 319-322.

Anderson, J. G. and P. G. Richards, 1975. Comparison of strong ground motion from several dislocation models, *Geophys. J. R. Astron. Soc.* **42**, 347-373.

Anderson, J. G. and S. E. Hough, 1984. A model for the shape of the Fourier amplitude spectrum of acceleration at high frequencies, *Bull. Seism. Soc. Am.* **74,** 1969-1994

Anderson, J. G., and J. N. Brune, 1999. Probabilistic seismic hazard analysis without the ergodic assumption, *Seism. Res. Lett.* **70**, no. 1, 19-28.

Andrews, D. J., 1981. A stochastic fault model, 2, Time-dependent case, *J. Geophys. Res.* **86**, 10,821-10,834.

Andrews, D. J. and J. Boatwright, 1998. Dynamic simulation of spontaneous rupture with heterogeneous stress drop, *Seism. Res. Lett.* **69**, 143.

Archuleta, R. J., 1984. A faulting model for the 1979 Imperial Valley earthquake, *J. Geophys. Res.* **89**, 4559-4585.

Archuleta, R.J., L. F., Bonilla, and D. Lavallée, 2000. Nonlinearity in observed and computed accelerograms, in *Proceeding of the 12 th World Conference on Earthquake Engineering*, Aston Koedyk Ltd (pub). Paper reference number 0338.

Ashford, S. A., N. Sitar, J. Lysmer, and N. Deng, 1997. Topographic effects on the seimic response of steep slopes, *Bull. Seism. Soc. Am.* **87**, 701-709.

Atkinson, G. M., 1993. Source spectra for earthquakes in eastern North America, *Bull. Seism. Soc. Am.* **83**, 1778-1798.

Belardinelli, M. E., M. Cocco, O. Coutant, and F. Cotton, 1999. Redistribution of dynamic stress during coseismic ruptures: Evidence for fault interaction and earthquake triggering, *J Geophys. Res.* **104**, 14,925-14945.

Bent, A. L., and D. V. Helmberger, 1989. Source complexity of the October 1, 1987, Whittier Narrows earthquake, *J. Geophys. Res.* **94**, 9548-9556.

Ben-Zion, Y., 2001. Dynamic ruptures in recent models of earthquake faults, *J. Mech. Phys. Solids* **49**, 2209-2244.

Beresnev, I. A., and G. M. Atkinson, 1997. Modeling finite-fault radiation from the ω^n spectrum, *Bull. Seism. Soc. Am.* **87**, 67-84.

Bernard, P. and R. Madariaga, 1984. A new asymptotic method for the modeling of near-field accelerograms, *Bull. Seism. Soc. Am.* **74**, 539-558.

Bernard, P., A. Herrero, and C. Berge, 1996. Modeling directivity of heterogeneous earthquake ruptures, *Bull. Seism. Soc. Am.* **86**, 1149-1160.

Beroza, G. C., and Spudich, P., 1988. Linearized inversion for fault rupture behavior: Application to the 1984 Morgan Hill, California, earthquake, *J. Geophys. Res.* **93**, 6275-6296.

Beroza, G. C., 1991. Near-source modeling of the Loma Prieta earthquake: Evidence for heterogeneous slip and implications for the earthquake hazard, *Bull. Seism. Soc. Am.* **81**, 1603-1621.

Boatwright, J., 1982. A dynamic model for far-field acceleration, *Bull. Seism. Soc. Am.* **72**, 1049-1068.

Boatwright, J. and D. M. Boore, 1982. Analysis of ground accelerations radiated by the 1980 Livermore Valley earthquakes for directivity and dynamic source characteristics, *Bull. Seism. Soc. Am.* **72**, 1843-1865.

Bonilla, L. F., J. H. Steidl, G. T. Lindley, A. G. Tumarkin, and R. J. Archuleta, 1997. Site amplification in the San Fernando Valley, California: Variability of site-effect estimation using the *S*-wave, coda, and *H/V* methods, *Bull. Seism. Soc. Am.* **87**, 710-730.

Bonilla, L. F., 2000. Computation of linear and nonlinear response for near field ground motion, Ph.D. Dissertation, University of California, Santa Barbara.

Boore, D. M., 1983. Stochastic simulation of high-frequency ground motions based on seismological models of the radiated spectra, *Bull. Seism. Soc. Am.* **73**, 1865-1884.

Boore, D. M., and W. B. Joyner, 1978. The influence of rupture incoherence on seismic directivity, *Bull. Seism. Soc. Am.* **68**, 283-300.

Boore, D. M. L. Seekins, and W. B. Joyner, 1989. Peak accelerations from the 17 October 1989 Loma Prieta earthquake, *Geophs. Res. Lett.* **60**, 151-156.

Boore, D. M. and W. B. Joyner, 1997. Site amplifications for generic rock sites, *Bull. Seism. Soc. Am.* **87**, 327-341.

Boore, D. M., W. B. Joyner, and T. E. Fumal, 1997. Equations for estimating horizontal response spectra and peak acceleration from western North America earthquakes: a summary of recent work, *Seism. Res. Lett.* **68**, No. 1, 128-153.

Boore, D. M. and L. T. Bown, 1998. Comparing shear-wave velocity profiles from inversion of surface-wave phase velocities with downhole measurements: Systematic differences between the CXW method and downhole measurments at six USC strong-motion sites, *Seism. Res. Lett.* **69**, 222-229

Borcherdt, R. D., J. F. Gibbs, and T. E. Fumal, 1979. Progress on ground motion predictions for the San Francisco Bay region, California, in *Progress on Seismic Zonation in the San Francisco Bay Region*, E. E. Brabb (Editor), *U. S. Geol. Surv. Circular* 807, 13-25.

Bouchon, M. C. A. Schultz, and M. N. Toksoz, 1996. Effect of three-dimensional topography on seismic motion, *J. Geophys. Res.* **101**, 5835-5846.

Bouchon, M., M. Campillo, and F. Cotton, 1998. Stress field associated with the rupture of the 1992 Landers, California, earthquake and its implications concerning the fault strenght at the onset of the earthquake, *J. Geophys. Res.* **103**, 21091-21097.

Bouchon, M., M. P. Bouin, H. Karabulut, M. N. ToksÎz, M. Dietrich, A. Rosakis, 2001. How Fast is Rupture during

an Earthquake? New Insights from the 1999 Turkey Earthquakes, *Geophys. Res. Lett.* **28** , 2723-2726.

Brown, M. and F. D. Tappert, 1986. Causality, caustics, and the structure of transient wave fields, *J. acoust. Soc. Am.* **80**, 251-255.

Brune, J. N., 1970. Tectonic stress and the spectra of seismic shear waves from earthquakes, *J. Geophys. Res.* **75**, 4997-5009.

Brune, J. N., 1971. Correction, *J. Geophys. Res.*, **76**, 5002.

Brune, J. N., 1999. Precarious rocks along the Mojave section of the San Andreas fault, California: Constraints on ground motion from great earthquakes, *Seism. Res. Lett.* **70**, 29-33.

Brune, J. N., 2000. Precarious rock evidence for low ground shaking on the footwall of major normal faults, *Bull. Seism. Soc. Am.* **90**, 1107-1112.

Campbell, K.W., 1997. Empirical near-source attenuation relationships for horizontal and vertical components of peak ground acceleration, peak ground velocity, and pseudo-absolute acceleration response spectra, *Seism. Res. Lett.* **68**, 154-179.

Castro, R. R., M. Mucciarelli, F. Pacor, and C. Petrungaro, 1997. S-wave site-response estimates using horizontal-to-vertical spectra ratios, *Bull. Seism. Soc. Am.* **87**, 256-260.

Catchings, R. D., and W. D. Mooney, 1992. New Madrid and central California apparent Q values as determined from seismic refraction data, *Seism. Res. Lett.* **63**, 49.

Catchings, R. D., and W. M. Kohler, 1996. Reflected seismic waves and their effect on strong shaking during the 1989 Loma Prieta, California, earthquake, *Bull. Seism. Soc. Am.* **86**, 1401-1416.

Chang, C. Y., C. M. Mok, M. S. Pwer, Y. K. Tang, H. T. Tang, and J. C. Stepp, 1991. Development of shear modulus reduction curves based on Lotung downhole ground motion data, in *Proc. of the 2nd Internation Conf. on Recent Advances in Geotechnical Earthquake Engineering and Soil Dynamics*, St. Louis, Missouri, 111-118.

Chapman, C. H., and P. M. Shearer, 1989. Ray tracing in azimuthally anisotropic media-II. Quasi-shear wave coupling, *Geophys. J.* **96**, 65-83.

Chavez-Garcia, F. J., W. R. Stephenson, M. Rodriguez, 1999. Lateral propagation effects observed at Parkway, New Zealand. A case history to compare 1D versus 2D site effects, *Bull. Seism. Soc. Am.* **89**, 718-372.

Coutant, O., 1996. Observations of shallow anisotropy on local earthquake records at the Garner Valley, Southern California, downhole array, *Bull. Seism. Soc. Am.* **86**, 477-488.

Culterra, G. C., D. M. Boore, W. B. Joyner, and C. M. Dietel, 1999. Nonlinear soil response in the vicinity of the Van Norman Complex following the 1994 Northridge, California, earthquake, *Bull. Seism. Soc. Am.* **89**, 1214-1231.

Das, S. and K. Aki, 1977. A numerical study of two-dimensional spontaneous rupture propagation, *Geophys. J. Roy. astr. Soc.* **50**, 643-668.

Das, S. and D. Kostrov, 1983. Breaking of a single asperity: Rupture process and seismic radiation. *J. Geophys. Res.*

88, 4277-4288.

Davis, P. M., J. L. Rubinstein, K. H. Liu, S. S. Gao, L. Knopoff, 2000. Northridge earthquake damage caused by geologic focusing of seismic waves, *Science* **289**, 1746-1750.

Day, S. M., 1982. Three-dimensional simulation of spontaneous rupture: The effect of nonuniform prestress, *Bull. Seism. Soc. Am.* **72**, 1881-1902.

Day, S. M., 1998. Efficient simulation of constant Q using coarse-grained memory variables, *Bull. Seism. Soc. Am.* **88,** 1051-1062.

Earthquake Engineering Reserach Institute, 1994. EERI Special Earthquake report, August 1994, *EERI Newsletter* **26**, 1-12.

Ellsworth, B., H. Ito, P. Malin, R. Abercrombie, 2001. In Jules Verne's footsteps: Seismology in the source, *EOS* **82**, 333-339.

Farra, V., P. Bernard, and R. Madariaga, 1986. Fast near source evaluation of strong ground motion for complex source models, *in* "Fifth Maurice Ewing Symposium on Earthquake Source Mechanics," Series 6 (S. Das, J. Boatwright, and C. Scholz, eds.), *Am. Geophys. Union*, pp. 121-130.

Fehler, M., H. Sato, and L.-J. Huang, 2000. Envelope broading of outgoing waves in 2D random media: A comparison between the Markov approximation and numerical simulations, *Bull. Seism. Soc. Am.* **90**, 914-928.

Field, E. H. and K. H. Jacob, 1995. A comparison and test of various site response estimation techniques including threee that are not reference site dependent, *Bull. Seism. Soc. Am.* **85**, 1127-1143.

Field, E. H., 1996. Spectral amplification in a sediment-filled valley exhibiting clear basin-edge-induced waves, *Bull. Seism. Soc. Am.* **86**, 991-1005.

Field, E. H., P. A. Johnson, I. A. Beresnev, and Y. Zeng, 1997. Nonlinear ground-motion amplification by sediments during the 1994 Northridge earthquake, *Nature*, **390**, 599-602.

Field, E. H., 2000. A modified ground-motion attenaution relationship for southern California that accounts for detailed site classification and a basin-depth effect, *Bull. Seism. Soc. Am.* **90**, S209-S221.

Frankel, A., 1991. High-frequency spectral falloff of earthquakes, fractal dimension of complex rupture, b value, and the scaling strength on faults, *J. Geophys. Res.* **96**, 6291-6302.

Frankel, A., 1993. Three-dimensional simulations of ground motions in the San Bernardino Valley, California, for hypothetical earthquakes on the San Andreas fault, *Bull. Seism. Soc. Am.* **83**, 1020-1041.

Frankel, A., 1999. How does the ground shake, *Science* **283**, 2032-2033.

Frankel, A. and R. W. Clayton, 1986, Finite difference simulations of seismic scattering: implications for the propagation of short-period seismic waves in the crust and models of crustal heterogeneity, *J. Geophys. Res. 91*, 6465-6489.

Frankel, A., S. Hough, P. Friberg, and R Busby, 1991. Observations of Loma Prieta aftershocks from a dense array in

Sunnyvale, California, *Bull. Seism. Soc. Am.* **81**, 1900-1922.

Frankel, A., and J. Vidale, 1992. A three-dimensional simulation of seimic waves in the Santa Clara Valley, California, from a Loma Prieta aftershock, *Bull. Seism. Soc. Am.* **82**, 2045-2074.

Frankel, A., S. Harmsen, C. Mueller, T. Barnhard, E.V. Leyendecker, D. Perkins, S. Hanson, N. Dickman, and M. Hopper, 1997. USGS National Seismic Hazard Maps: Uniform Hazard Spectra, De-aggregation, and Uncertainty, in *Proceedings of FHWA/NCEER Workshop on the National Representation of Seismic Ground Motion for New and Existing Highway Facilities*, NCEER Technical Report 97-0010, pp. 39-73.

Frankel, A., and W. Stephenson, 2000. Three-dimensional simulations of ground motins in the Seattle region for earthquakes in the Seattle fault zone, *Bull. Seism. Soc. Am.* **90**, 1251-1267.

Frankel, A., D. Carver, E. Cranswick, T. Bice, R. Sell, and S. Hanson, 2001. Observations of basin ground motions from a dense seismic array in San Jose, California, *Bull. Seism. Soc. Am.* **91**, 1-12.

Fueund, L. B., 1979. The mechanics of dynamic shear crack propagation, *J. Geophys. Res.* **84**, 2199-2209.

Fuis, G. S., T. Ryberg, N. J. Godfrey, D. A. Okaya, and J. M. Murphy, 2001. Crustal structure and tectonics from the Los Angeles basin to the Mojave desert, southern California, *Geology* **29**, 15-18.

Fukuyama, E. and R. Madariaga, 1995. Integral equation method for plane crack with arbitary shape in 3D elastic medium, *Bull. Seism. Soc. Am.* **85**, 614-628.

Gao, H., Y. Huang, and A. J. Rosakis, 1999. On radiation-free transonic motion of cracks and dislocations, *J. Mech. Phys. Sol.* 47, 1893-1961.

Ghayamghamain, M. R., and H. Kawakami, 1996. On the characteristics of non-linear soil response and dynamic soil properties using vertical array data in Japan, *Earthquake Eng. Struct. Dyn.* **25**, 857-870.

Godfrey, N. J., B. C. Beaudoin, S. L. Klemperer, A. Levander, J. Luetgert, A. Meltzer, W. Mooney, and A. Tréhu, 1997. Ophiolitic basement to the Great Valley forearc basin, California, from seismic and gravity data: Implications for crustal growth at the North American continental margin, *Geol. Soc. Am. Bull.* **108**, 1536–1562.

Graves, R. W., 1996. Simulating seismic wave propagation in 3D elastic media using staggered-grid finite differences, *Bull. Seism. Soc. Am.* **86**, 1091-1106.

Graves, R. W., A. Pitarka, and P. G. Somerville, 1998. Ground motion amplification in the Santa Monica area: Effects of shallow basin structure, *Bull. Seism. Soc. Am.* **88**, 1224-1242.

Guatteri, M., and P. Spudich, 1998. Coseismic temporal changes of slip direction: The effect of absolute stress on dynamic rupture, *Bull. Seism. Soc. Am.* **88**, 777-789.

Haddon, R. A. W., 1995. Modeling of source rupture characteristics for the Saguenay earthquake of November 1988, *Bull. Seism. Soc. Am.* **85**, 525-551.

Haddon, R. A. W., 1996. Earthquake source spectra in eastern North America, *Bull. Seism. Soc. Am.* **86**, 1300-1313.

Hanks, T. C., 1982. f_{max}, *Bull. Seism. Soc. Am.* **72**, 1867-1879.

Hanks, T.C. and H. Kanamori, 1979. A moment magnitude scale, *J. Geophys. Res.* **84**, 2348-2350.

Hanks, T. C., and R. K. McGuire, 1981. The character of high-frequency strong ground motion, *Bull. Seism. Soc. Am.* **71**, 2071-2095.

Hanks, T. C., and K. Krawinkler, 1991. The 1989 Loma Prieta, California, earthquake and its effects: Introduction to the Special Issue, *Bull. Seism. Soc. Am.* **81**, 1415-1423.

Harichandran, R. S., 1999. Spatial variation of earthquake ground motion: What is it, how do we model it, and what are its engineering implications?, http://www.egr.msu.edu/~harichan/papers/present/svegm.pdf.

Harris, R. A. and S. M. Day, 1993. Dynamics of fault interaction: Parallel strike-slip faults, *J. Geophys. Res.* **98**, 4461-4472.

Harris, R. A., and S. M. Day, 1997. Effects of a low-velocity zone on dynamic rupture, *Bull. Seism. Soc. Am.* **87**, 1267-1280.

Harris, R.A. and S. M. Day, 1999. Dynamic 3D simulations of earthquakes on en echelon faults, *Geophys.Res. Lett.* **26**, 2089-2092.

Hartzell, S. H., 1978. Earthquake aftershocks as Green's functions, *Geophys. Res. Lett.* **5**, 1-4.

Hartzell, S., D. Carver, E. Cranswick, and A. Frankel, 2000. Variability of site response in Seattle, Washington, *Bull. Seism. Soc. Am.* **90**, 1237-1250.

Haskell, N. A., 1969. Elastic displacements in the near-field of a propagating fault, *Bull. Seism. Soc. Am.* **59**, 865-908.

Hernandez, B., F. Cotton, and M. Campillo, 1999. Contribution of radar interfermetry to a two-step inversion of the kinematic process of the 1992 Landers earthquake, *J. Geophys. Res.* **104**, 13,082-13,099.

Herrero A. and P. Bernard, 1994. A kinematic self similar rupture process for earthquakes, *Bull. Seism. Soc. Am.* **84**, 1216-1228.

Hough, S. E., and J. G. Anderson, 1988. High-frequency spectra observed at Anza, California: Implications for Q structure, *Bull. Seism. Soc. Am.* **78**, 692-707.

Hough, S. E., J. G. Anderson, J. Brune, F. Vernon, J. Berger, J. Fletcher, L. Haar, T. Hanks, and L. Baker, 1988. Attenuation near Anza, California, *Bull. Seism. Soc. Am.* **78**, 672-691.

Hutchings, L., 1994. Kinematic earthquake models and synthesized ground motions using empirical Green's functions, *Bull. Seism. Soc. Am.* **84**, 1028-1050.

Hutchings, L. and F. Wu, 1990. Empirical Green's functions from small earthquakes - A waveform study of locally recorded aftershocks of the San Fernando earthquakes, *J. Geophys. Res.* **95**, 1187-1214.

Hutchings, L., and S. Jarpe, 1996. Ground-motion variability at the Highway 14 and I-5 interchange in the northern San Fernando Valley, *Bull. Seism. Soc. Am.* **86**, S289-S299.

Hutchings, L.J., F.T. Wu, R.-J. Rau, S.P. Jarpe, P.W. Kasameyer, W. Foxall, 1997. Strong Ground Motion Synthesis Along the Sanyi-Tungshih-Puli Seismic Zone Using Empirical Green's Functions, in *Proceedings 1997 Central*

Weather Bureau 100th Anniversary International Conference on Weather Analysis and Forecasting, Taipei, Taiwan, pp 22-33, March 3-5, 1997.

Heaton, T. H., J. F. Hall, D. J. Wald, and M. W. Halling, 1995. Response of high-rise and base-isolated buildings to a hypothetical Mw 7.0 blind thrust earthquake, *Science* **267**, 206-211.

Idriss, I. M., 1993. Selection of earthquake ground motions at rock sites: Report Prepared for the Structures Div., Building and Fire Reseach Lab., NIST, Gathersburg, Maryland, no.93-625.

Idriss, I. M., and Seed, H. B., 1968a. Seismic response of horizontal soil layers, Proc. Am. Soc. Civil Eng. J. soil Mech. Found. Div. 94, SM4, 1003-1031.

Idriss, I. M., and Seed, H. B., 1968b. An analysis of ground motions during the 1957 San Francisco earthquake, *Bull. Seism. Soc. Am.* **58**, 2013-2032.

Irikura, K., 1983. Semi-empirical estimation of strong ground motions during large earthquakes, Bull. Disaster Prevention Res. Inst. (Koyoto Univ.) **33**, 63-104.

Ishihara, K., 1996. *Soil Behavior in Earthquake Geotechnics*, Oxford Univ. Press, New York.

Jarpe, S. P. and P. W. Kasameyer, 1996. Validation of a procedure for calculating broadband strong-motion time histories with empirical Green's functions, *Bull. Seism. Soc. Am.* **86**, 1116-1129.

Joyner, W. B., 1991. Directivity for nonuniform ruptures, *Bull. Seism. Soc. Am.* **81**, 1391-1395.

Joyner, W. B., and A. T. F. Chen, 1975. Calculation of nonlinear ground response in earthquakes, *Bull. Seism. Soc. Am.* **65**, 1315-1336.

Joyner, W. B., R. E. Warrick, and T. E. Funal, 1981. The effect of Quaternary alluvium on strong ground motion in the Coyote Lake, California earthquake of 1979, *Bull. Seism. Soc. Am.* **71**, 1333-1349.

Joyner, W.B. and D. M. Boore, 1988. Measurement, characteristics and prediction of strong ground motion: *in* "Proceedings, Specialty Conference on Earthquake Engineering and Soil Dynamics II", ASCE, Park City, Utah, p. 43-102.

Joyner, W. B. and D. M. Boore, 1993. Methods for regression analysis of strong-motion data, *Bull. Seism. Soc. Am.,* **83**, 469-487.

Kanamori, H. and E. E. Brodsky, The physics of earthquakes, *Phyics Today* 54, 34-41: http://physicstoday.org/pt/vol-54/iss-6/p34.html

Kawasaki, I., and T. Tanimoto, 1981. Radiation pattern of body waves due to the seismic dislocation occurring in an anisotropic source medium, *Bull. Seism. Soc. Am.* **71**, 37-50.

Kawase, H., 1996. The cause of the damage belt in Kobe: "The basin-edge effect," constructive interference of the direct *S*-wave with the basin-induced diffracted/Rayleigh waves, *Seism. Res. Lett.* **67**, no. 5, 25-34.

Koketsu, K., and M. Kikuchi, 2000. Propagation of seismic ground motion in the Kanto Basin, Japan, *Science* **288**, 1237-1239.

Laforge, R. C., O'Connell, D. R. H., and Unruh, J., 2000. The effect of local site conditions and fault geometry on a proabilistic seismic hazard assessment for Monticello Dam, California, *Seism. Res. Lett.* **71**, no. 1, 245.

Langston, C. A., 1979. Structure under Mount Ranier, Washington, inferred from teleseismic body waves, *J. Geophys. Res.* **84**, 4749-4762.

Larsen, S., and J. Grieger, 1998. Elastic modeling initiative, part III: 3-D computational modeling, Expanded Abstracts, 68th Annual SEG meeting, 1803-1806.

Lermo, J. and F. Chavez-Garcia, 1993. Site effect evaluation using spectral ratios with only one station, *Bull. Seism. Soc. Am.* **83**, 1574-1594.

Lettis, W. R., D. L. Wells, and J. N. Baldwin, Empirical observations regarding reverse earthquakes, blind thrust faults, and Quaternary deformation: Are blind thrust faults truly blind, *Bull. Seism. Soc. Am.* **87**, 1171-1198.

Li, Y. G., J. E. Vidale, K. Aki, C. J. Marone, W. H. K. Lee, 1994. Fine structure of the Landers fault zone; segmentation and the rupture process, *Science* **256**, 367-370.

Liu, H.-L., and T. Heaton, 1984. Array analysis of the ground velocities and accelerations from the 1971 San Fernando, California, earthquake, *Bull. Seism. Soc. Am.* **74**, 1951-1968.

Liu, H. L., and D. V. Helmberger, 1985. The 23:19 aftershock of the 15 October 1979 Imperial Valley earthquake: More evidence for an asperity, *Bull. Seism. Soc. Am.* **75**, 689-709.

Lomnitz, C., J. Flores, O. Novaro, T. H. Seligman, and R. Esquivel, 1999. Seismic coupling of interface modes in sedimentary bains: A recipe for distaster, *Bull. Seism. Soc. Am.* **89**, 14-21.

Lutter, W. J., G. S. Fuis, C. Thurber, and J. Murphy, Tomographic images of the upper crust from the Los Angeles basin to the Mojave Desert, California: Results from the Los Angeles Region Seismic Experiment, *J. Geophys. Res.* **104,** 25,543-24565.

Madariaga, R., 1977. High-frequency radiation from crack (stress-drop) models of earthquake faulting, *Geophys. J.* **51**, 625-652.

Magistrale, H. and S. Day, 1999. 3D simulations of multi-segment thrust fault rupture, *Geophys. Res. Lett.* **26**, 2093-2096.

Magistrale, H., S. Day, R. W. Clayton, and R. Graves, 2000. The SCEC Southern California reference three-dimensional seismic velocity model version 2, *Bull. Seism. Soc. Am.* **90**, S65-S76.

Mai, P. M., and G. C. Beroza, 2000. Source scaling properties from finite-fault-rupture models, *Bull. Seism. Soc. Am.* **90**, 604-615.

Makris, N. , Y. Roussos, and J. Zhang, 1999. Rocking response of rigid blocks under near-source motions, Proceedings 13th ASCE Engineering Mechanics Division Conference, June 13-16, 1999, Baltimore, MD, http://rongo.ce.jhu.edu/emd99/sessions/sessions/papers/makris1.pdf.

Margerin, L., Campillo, M., and B. Van Tiggelen, 2000. Monte Carlo simulation of multiple scattering of elastic waves, *Bull. Seism. Soc. Am.* **90**, 7873-7892.

Marshall, G. A., R. S. Stein, and W. Thatcher, 1991. Faulting geometry and slip from co-seismic elevation changes: The 18 October 1989, Loma Prieta, California, earthquake, *Bull. Seism. Soc. Am.* **75**, 1660-1693.

Moczo, P. , J. Kristek, L. Halada, 2000. 3D fourth-order staggered-grid finite-difference schemes: Stability and grid dispersion, *Bull. Seism. Soc. Am.* **90**, 587-603.

Obara, K. and H. Sato, 1995. Regional differences of random inhomogeneities aroudn the volcanic front in the Kanto-Tokai area, Japan, revealed from the broadening of *S* wave seismogram envelopes, *J. Geophys. Res.* **100**, 2103-2121.

O'Connell, D. R. H., 1998. Synthesizing site-specific near-field ground motinos from reverse faults: New perspectives on peak velocity hazards using broadband site responses, *Proceedings CDROM of the Sixth U.S. National Conference on Earthquake Engineering*, Earthquake Engineering Research Institude, paper 362, animation located at.ftp::/ftp.seismo.usbr.gov/pub/outgoing/geomagic/movies/pap362_gm.mpg.

O'Connell, D. R. H., 1999a. Replication of apparent nonlinear seismic response with linear wave propagation models, *Science* **283**, 2045-2050.

O'Connell, D. R. H., 1999b. Possible super-shear rupture velocities during the 1994 Northridge earthquake, *EOS* **80**, F941.

O'Connell, D. R. H., 1999c. Ground motion evaluation for Casitas Dam, Ventura River Project, California, U. S. Bureau of Reclamation Seismotectonic Report 99-4, Denver, CO.

O'Connell, D. R. H., 2000. Do you live in a bad neighborhood? May site-specific PSHA is an oxymoron, *Seism. Res. Lett.* **71**, 246.

O'Connell, D. R. H., J. R. Unruh, and L. V. Block, in press. Source characterization and ground motion modeling of the 1892 Vacaville-Winters earthquake sequence, California, *Bull. Seism. Soc. Am.*

Oglesby, D. D. and R. J. Archuleta, 1997. A faulting model for the 1992 Petrolia earthquake: Can extreme ground acceleration be a source effect?, *J. Geophys. Res.* **102**, 11,877-11,897.

Oglesby, D. D., R. J. Archuleta, and S. B. Nielsen, 1998. Earthquakes on dipping faults:The effects of broken symmetry, *Science* **280**, 1055-1059.

Oglesby, D. D., R. J. Archuleta, and S. B. Nielsen, 2000. The three-dimensional dynamics of dipping faults, *Bull. Seism. Soc. Am.* **901**, 616-628.

Olsen, A. H. and R. J. Apsel, 1982. Finite faults and inverse theory with applications to the 1979 Imperial Valley earthquake, *Bull. Seism. Soc. Am.* **72**, 1969-2001.

Olsen, K. B. and R. J. Archuleta, 1996. Three-dimensional simulation of earthquakes on the Los Angeles fault system, *Bull. Seism. Soc. Am.* **86**, 575-596.

Olsen, K.B., R. Madariaga, R.J. Archuleta, 1997. Three-dimensional dynamic simulation of the 1992 Landers earthquake, *Science* **278**, 834-838.

Oreskes, N., K. Shrader-Frechette, and K. Belitz, 1994. Verification, validation, and confirmation of numerical mod-

els in the Earth sciences, *Science*, **264**, 641-646.

Phillips, W. S., S. Kinoshita, and H. Fujiwara, 1993. Basin-induced Love waves observed using the strong motion array at Fuchu, Japan, *Bull. Seism. Soc. Am.* **83**, 65-84.

Pitarka, A., K. Irikura, T. Iwata, H. Sekiguchi, 1998. Three-dimensional simulation of the near-fault ground motions for the 1995 Hyogo-Nanbu (Kobe), Japan, earthquake, *Bull. Seism. Soc. Am.* **88**, 428-440.

Pitarka, A., P. Somerville, Y. Fukushima, T. Uetake, K. Irikura, 2000. Simulation of near-fault strong-ground motion using hybrid Green's functions, *Bull. Seism. Soc. Am.* **90**, 566-586.

Robertsson, J. 0. A., J. 0. Blanch, and W. W. Symes, 1994. Viscoelastic finite-difference modcling, *Geophysics* **59**, 1444-1456.

Rodriguez, A., J. D. Bray, and N. A. Abrahamson, 2001. An empirical geotechnical seismic site response procedure, *Earthquake Spectra* **65**, 65-87.

Rosakis, A. J., O. Samudrala, and D. Coker, 1999. Cracks faster than the shear wave speed, *Science* **284**, 1337-1340.

Rubin, A. M. and D. Gillard, 2000. Aftershock asymmetry/rupture directivity among central San Andreas fault microearthquakes, *J. Geophys. Res.* **105**, 19,095-19,109.

Sadigh, K., C.-Y. Chang, J. A. Egan, F. Makdisi, and R. R. Youngs, 1997. Atenuation relationships for shallow crustal earthquakes based on California strong motion data, *Seism. Res. Lett.* **68**, no. 1, 180-189.

Santa-Cruz, S., E. Heredia-Zavoni, and R. S. Harichandran, 2000. Low-frequency behavior of coherency for strong ground motions in Mexico City and Japan, Proceedings (CD-ROM), 12th World Conference on Earthquake Engineering, Auckland, New Zealand, Paper No. 0076, 8 pp.

Sato, H., and M. C. Fehler, 1998. *Seismic Wave Propagation and Scattering in the Heterogenous Earth*, Springer-Verlag, New York, 308 pp.

Sato, K., T. Kokusho, M. Matsumoto, and E. Yamada, 1996. Nonlinear seismic response and soil property during strong motion, Special Issue on Geotechnical Aspects of the January 17, 1995 Hyogoken-Nambu Earthquake, *Soils and Foundations*, 41-52.

Satoh, T., H. Kawase, and T. Sato, 1995. Nonlinear behavior of soil sediments identified by using borehole records observed at the Ashigara Valley, Japan, *Bull. Seism. Soc. Am.* **85**, 1821-1834.

Satoh, T., M. Horike, Y. Takeuchi, T. Uetake, and H. Suzuki, 1997. Nonlinear behavior of scoria evaluated from borehole records in eastern Shizuoka prefecture, Japan, *Earthquake Eng. Struc. Dyn.* **26**, 781-795.

Satoh, T., M. Fushimi, and Y. Tatsumi, 2001. Inversion of strain-dependent nonlinear characteristics of soils using weak and strong motions observed by borehole sites in Japan, *Bull. Seism. Soc. Am.* **91**, 365-380.

Schneider, J. F., W. J. Silva, and C. Stark, 1993. Ground motion model for the 1989 M 6.9 Loma Prieta earthquake including effects of source, path, and site, *Earthquake Spectra*, **9**, 251-287.

Seed, H. B., M. P. Romo, J. I. Sun, A. Jaime, and J. Lysmer, 1988. The Mexico earthquake of September 19, 1985 -

relationships between soil conditions and earthquake ground motions, *Earthquake Spectra*, **4**, 687-729.

Schultz, C. A., 1994. Enhanced backscattering of seismic waves from irregular interfaces, *Ph.D. Thesis*, Massachusetts Institue of Technology, Cambridge.

Shaw, J. H. and P. M. Shearer, 1999. An elusive blind-thrust fault beneath metropolitan Los Angeles, *Science* **283**, 1516-1518.

Shin, T. C., K. W. Kuo, W. H. K. Lee, T. L. Teng, and Y. B. Tsai, 2000. A preliminary report of the 1999 Chi-Chi (Taiwan) earthquake, *Seism. Res. Lett.*, **71**, 24-30.

Silva, W. J. and K. Lee, 1987. WES RASCAL code for synthesizing earthquake ground motions: State-of-the-Art for Assessing Earthquake Hazards in the United States, Report 24, U.S. Army Corps of Engineers Waterways Experiment Station, Miscellaneous Paper S-73-1, 120 pp.

Silva, W. J., I. G. Wong, and R. B. Darragh, 1992. Engineering characterization of earthquake strong ground motion with applications to the Pacific Northwest, *in* A. M. Rogers and others [**eds.**], "Assessing Earthquake Hazards and Reducing Risk in the Pacific Northwest", U. S. Geol. Surv. Professional Paper 1560.

Silva, W. J. and R. B. Darragh, 1995. Engineering characterization of strong ground motion recorded at rock sites: unpublished draft report submitted to Electric Power Research Institute, Research Project Rep. 2556-48.

Somerville, P. G., 1998. Emerging art: earthquake ground motion: *in* P. Dakolas and others [**eds.**], "Proceedings-Geotechnical Earthquake Engineering and Soil Dynamics III", ASCE Speciality Conf. Special Pub.75, Seattle, WA, 1-38.

Somerville, P., and J. Yoshimura, 1990. The influence of critical Moho reflections on strong ground motions recorded in San Francisco and Oakland during the 1989 Loma Prieta earthquake, *Geophys. Res. Lett.* **17**, 1203-1206.

Somerville, P., M. Sen, and B. Cohee, 1991. Simulations of strong ground motions recorded during the 1985 Michoacan, Mexico and Valparaiso, Chile, earthquakes, *Bull. Seism. Soc. Am.* **81**, 1-27.

Somerville, P. G., N. F. Smith, and R. W. Graves, 1994. The effect of critical Moho reflections on the attenuation of strong motion from the 1989 Loma Prieta earthquake: *in* "The Loma Prieta, California Earthquake of October 17, 1989-Strong Ground Motion", U. S. Geol. Surv. Prof. Paper 1551-A, p. A67-A69.

Somerville, P. G., N. F. Smith, R. W. Graves, and N. A. Abrahamson, 1997. Modification of empirical strong ground motion attenuation relations to include the amplitude and duration effects of rupture directivity, *Seism. Res. Lett.*, **68**, 199-222.

Somerville, P., K. Irikura, R. Graves, S. Sawada, D. Wald, N. Abrahamson, Y. Iwasaki, T. Kagawa, N. Smith, and A. Kowada, 1999. Characterizing crustal earthquake slip models for the prediction of strong ground motion, *Seism. Res. Lett.* **70**, 59-80.

Spetzler, J., and R. Snieder, 2001. The formation of caustics in two- and three-dimensional media, *Geophys. J. Int.*, **144**, 175-182.

Steidl, J. H., R. J. Archuleta, S. H. Hartzell, 1991. Rupture history of the 1989 Loma Prieta, California, earthquake, *Bull. Seism. Soc. Am.* **81**, 1573-1602.

Spudich, P., and E. Cranswick, 1984. Direct observation of rupture propagation during the 1979 Imperial Valley earthquake using a short baseline accelerometer array, *Bull. Seism. Soc. Am.* **74**, 2083-2114.

Spudich, P., and L. N. Frazer, 1984. Use of ray theory to calculate high-frequency radiation from earthquake sources having spatially variable rupture velocity and stress drop, *Bull. Seism. Soc. Am.* **74**, 2061-2082.

Spudich, P., and L. N. Frazer, 1987. Errata for "Use of ray theory to calculate high-frequency radiation from earthquake sources having spatially variable rupture velocity and stress drop", *Bull. Seism. Soc. Am.* **77**, 2245-2246.

Spudich, P., and D. Oppenheimer, 1986. Dense seismograph array observations of earthquake rupture dynamics, *in* "Fifth Maurice Ewing Symposium on Earthquake Source Mechanics," Series 6 (S. Das, J. Boatwright, and C. Scholz, eds.), Am. Geophys. Union, Washington, DC, pp. 285-296.

Spudich, P., and R. J. Archuleta, 1987. Techniques for earthquake ground-motion calculation with applicatins to source parameterization to finite faults, *in* "Seismic Strong Motion Synthesis," (B. A. Bolt, ed.), Academic Press, Orlando, Florida, pp. 205-265.

Spudich, P., and M. Iida, 1993. The seismic coda, site effects, and scattering in alluvial basins studied using aftershocks of the 1986 North Palm Springs, California, earthquakes as source arrays, *Bull. Seism. Soc. Am.* **83**, 1721-1743.

Spudich, P., M. Hellweg, and W. H. K. Lee, 1996. Directional topographic site response at Tarzana observed in aftershocks of the 1994 Northrige, Calfornia, earthquake: Implications for mainshock motions, *Bull. Seism. Soc. Am.* **86**, S193-S208.

Spudich, P., J. B. Fletcher, M. Hellweg, J. Boatwright, C. Sullivan, W. B. Joyner, T. C. Hanks, D. M. Boore, A. McGarr, L. M. Baker, and A. G. Lindh, SEA96 - A new predictive relation for earthquake ground motions in extensional tectonic regimes, *Seism. Res. Lett.* **68**, no. 1, 190-198.

Spudich, P., M. Guatteri, K. Otsuki, and J. Minagawa, 1998. Use of fault striations and dislocation models to infer tectonic shear stress during the 1995 Hyogo-ken Nanbu (Kobe) earthquake, *Bull. Seism. Soc. Am.* **88**, 413-427.

Stein, R.S. and G. Ekström, 1992. Seismicity and geometry of a 110-km-long blind thrust fault: 2. Synthesis of the 1982-1985 California earthquake sequence, *J. Geophys. Res.* **97**, 4865-4883.

Stephenson, W. J. and A. D. Frankel, 2000. Preliminary simulation of a M 6.5 earthquake on the Seattle fault using 3D finite-difference modeling, U.S. Geological Survey Open-File Report 00-339, http://geology.cr.usgs.gov/pub/open-file-reports/ofr-00-0339/.

Stephenson, W. J., R. A. Williams, J. K. Odum, and D. M. Worley, 2000. High-resolution seismic reflection surveys and modeling across an area of high damage from the 1994 Northridge earthquake, Sherman Oaks, California, *Bull. Seism. Soc. Am.* **90**, 643-654.

Toro, G. R., N. A. Abrahamson, and J. F. Schneider, 1997. Model of strong ground motions from earthquakes in Central and Eastern North America: Best estimates of uncertainties, *Seism. Res. Lett.* **68**, 41-57.

Tumarkin, A. G., R. J. Archuleta, and R. Madariaga, 1994. Scaling relations for composite earthquake models, *Bull. Seism. Soc. Am.* **84**, 1279-1283.

Tsubio, S., M. Saito, and Y. Ishihara, 2001. Verification of horizontal-to-vertical spectral-ratio technique for estimate of site response using borehole seismographs, *Bull. Seism. Soc. Am.* **91**, 499-510.

Vidale, J. E., 1989. Influence of focal mechanism on peak accelerations of strong motions of the Whittier Narrows, California, earthquake and an aftershock, *J. Geophys. Res.* **94**, 9607-9613.

Wald, D. J, D. V. Helmberger, and T. H. Heaton, 1991. Rupture model of the 1989 Loma Prieta earthquake from the inversion of strong-motions and broadband teleseismic data, *Bull. Seism. Soc. Am.* **81**, 1540-1572.

Wald, D. J, T. H. Heaton, and K. W. Hudnut, 1996. The slip history of the 1994 Northridge, California, earthquake determined from strong-motion, teleseismic, GPS, and leveling, *Bull. Seism. Soc. Am.* **86**, S49-S70.

Wald, D. J., and R. W. Graves, 1998. The seismic response of the Los Angeles Basin, California, *Bull. Seism. Soc. Am.* **88**, 337-356.

Wells, D.L. and K. J. Coppersmith, 1994. New empirical relationships amoung magnitude, rupture length, rupture width, rupture area, and surface displacement, *Bull. Seism. Soc. Am.* **84**, 974-1002.

Wen, K. L., I. A. Beresnev, and Y. T. Yeh, 1995. Investigation of nonlinear site amplification at two downhole strong ground motion arrays in Taiwan, *Earthquake Eng. Struct. Dyn.* **24**, 313-324.

White, B., B. Nair, and A. Baylies, 1988. Random rays and seismic amplitude anomalies, *Geophysics* **53**, 903-907.

Williams, R. A., W. J. Stephenson, A. D. Frankel, and J. K. Odum, 1999. Surface seismic measurements of near-surface P- and S-wave seismic velocities at earthquake recording stations, *Earthquake Spectra* **15**, 565-584.

Yim, C.-Y., A. K. Chopra, and J. Penzien. 1980. Rocking response of rigid blocks to earthquakes., *Earthquake Eng. Struct. Dynamics* **8**,565-87.

Zeng, Y., J. G. Anderson, and G. Yu, 1994. A composite source model for computing realistic strong ground motions, *Geophys. Res. Lett.* **21**, 725-728.

Zeng, Y., 1995. A realistic synthetic Green's function calculation using a combined deterministic and stochastic modeling approach, *EOS*, **76**, F370.

Zeng, Y., and J. Anderson, 2000. Evaluation of numerical procedures for simulating near-fault long-period ground motions using the Zeng method, Pacific Earthquake Engineering Res. Center Utilities Program Report 2000/01.

Zhang, B. and A. S. Papgeorgiou, 1996. Simulation of the response of the Marina District basin, San Francisco, California, to the 1989 Loma Prieta earthquake, *Bull. Seism. Soc. Am.* **86**, 1382-1400.

Zoback, M. D. and C. M. Wentworth, 1986. Crustal studies in central California, using an 800-channel seismic reflection recording system, *in* Reflection Seismology: A Global Perspective, M. Barazangi and L. Brown, *eds.*, Am. Geophys. Union, Washington, D.C., pp. 183-196.

.

Table 1: $\dot{S}_{ij}(\omega)$ Source Amplitude Factors

Factor	Influence
Moment, $\dot{S}_{ij}^{M_0}(\omega)$	Moment directly scales peak velocities and accelerations since moment determines the average slip for a fixed fault area.
Stress drop, $\dot{S}_{ij}^{\Delta\sigma}(\omega)$	Since $\dot{S}_{ij}(\omega) \propto \Delta\sigma$, $\Delta\sigma$ directly scales peak velocities. Spatial variations of stress drop introduce frequency dependent amplitude variations.
Rupture velocity $\dot{S}_{ij}^{V_r}(\omega)$	High rupture velocities increase amplification associated with directivity. Rupture velocities interact with stress drops and rise times to modify the amplitude spectrum.
Healing velocity $\dot{S}_{ij}^{V_h}(\omega)$	High healing velocities increase amplification associated with directivity. Healing velocities interact with stress drop and rise time variations to modify the amplitude spectrum, although to a smaller degree than rupture velocities, since rupture slip velocities are typically several times larger than healing slip velocities.
Rake and radiation pattern, $\dot{S}_{ij}^{A}(\omega)$	Rake and spatial and temporal rake variations directly scale amplitudes as a function of azimuth and take-off angle. Rake spatial and temporal variations over a fault increase the spatial complexity of radiation pattern amplitude variations and produce frequency-dependent amplitude variability.
Rise time, $\dot{S}_{ij}^{t_\Delta}(\omega)$	Since $\omega_c \propto \frac{1}{t_\Delta}$, spatially variable rise times produce a frequency dependence of the amplitude spectrum.
Crack diffraction, $\dot{S}_{ij}^{C}(\omega)$	Diffraction at the crack tip introduces a frequency dependent amplitude to the radiation pattern (Madariaga, 1977; Boatwright, 1982; Fukuyama and Madariaga, 1995).
Dynamics, $\dot{S}_{ij}^{D}(\omega)$	Fault rupture is heterogeneous velocity structure can produce anisotropic slip velocities relative to rupture direction (Harris and Day, 1997) and slip-velocities are a function of rake and dip for dipping dip-slip faults (Oglesby et al., 1998; 2000). Frictional heating, fault zone fluids, and melting may also influence radiated energy (Kanamori and Brodsky, 2001).
Hypocentral depth $\dot{S}_{ij}^{H_z}(\omega)$	For crustal earthquakes, deeper hypocenters tend to increase peak ground motions by increasing isochrone velocities (O'Connell, 1999c).

Table 2: $\tau_{ij}(\omega)$ Source Phase Factors

Factor	Influence
Rupture velocity, $\tau_{ij}^{V_r}(\omega)$	Produces phase delays, $\tau_{ij}^{V_r}(\omega) = e^{i\omega t_r}$, where t_r is the rupture travel time from the hypocenter to element *ij*. Abrupt changes in rupture velocity can produce discontinues phase delays between adjacent elements of the fault.
Healing velocity, $\tau_{ij}^{V_h}(\omega)$	Produces phase delays, $\tau_{ij}^{V_h}(\omega) = e^{i\omega t_h}$, where t_h is the healing travel time from the hypocenter to element *ij*. Abrupt changes in healing velocity can produce discontinues phase delays between adjacent elements of the fault.
Rise time, $\tau_{ij}^{t_A}(\omega)$	Spatially and temporally varying rise times produce frequency dependent phase variations.
Rake, $\tau_{ij}^{A}(\omega)$	Changes initial phase or polarization of various seismic body and surface waves.
Crack diffraction, $\tau_{ij}^{C}(\omega)$	Diffraction at the crack tip introduces frequency dependent phase variations (Madariaga, 1977; Boatwright, 1982; Fukuyama and Madariaga, 1995).
Dynamics, $\tau_{ij}^{D}(\omega)$	Fault rupture is heterogeneous velocity structure can produce anisotropic slip velocities relative to rupture direction (Harris and Day, 1997) and slip-velocities are a function of rake and dip for dipping dip-slip faults (Oglesby et al., 1998; 2000). Frictional heating, fault zone fluids, and melting may also influence radiated energy (Kanamori and Brodsky, 2001).

Table 3: $G_{kij}(\omega)$ Propagation Amplitude Factors

Factor	Influence
Geometric spreading, $G^{r}{}_{kij}(\omega)$	Amplitudes decrease with distance at $1/r$, $1/r^2$, and $1/r^4$ for body waves and $1/(\sqrt{r})$ for surface waves. The $1/r$ term has the strongest influence on high-frequency ground motions. The $1/(\sqrt{r})$ term can be significant for locally generated surface waves.
Large-scale velocity structure, $G^{V_{3D}}{}_{kij}(\omega)$	Horizontal and vertical velocity gradients and velocity discontinuities can increase or decrease amplitudes and durations. Low-velocity basins can amplify and extend ground motion durations. Abrupt changes in lateral velocity structure can induce basin-edge-waves in the lower velocity material that amplify ground motions.
Near-surface resonant responses, $G^{L}{}_{kij}(\omega)$	Low-velocity materials near the surface amplify ground motions for frequencies > $f = \frac{\beta}{4h}$, where h is the thickness of near-surface low velocity materials. Coupled interface modes can amplify and extend durations of ground motions.
Nonlinear soil responses, $G^{N}{}_{kij}(\omega)$	Depending on the dynamic soil properties and pore pressure responses, nonlinear soil responses can decrease intermediate- and high-frequency amplitudes, amplify low- and high-frequency amplitudes, and extend or reduce duration of large amplitudes.
Frequency independent attenuation, $G^{Q}{}_{kij}(\omega)$	Linear hysteretic behavior that reduces amplitudes of the form $e^{\frac{-\pi \cdot f \cdot r}{\beta \cdot Q(f)}}$.
High-frequency attenuation, $G^{\kappa}{}_{kij}(\omega)$	Strong attenuation of high-frequencies in the shallow crust of the form $e^{-\pi \cdot \kappa(r) \cdot f}$.
Scattering, $G^{S}{}_{kij}(\omega)$	Scattering tends to reduce amplitudes on average, but introduces high amplitude caustics and low-amplitude shadow zones and produces nearly log-normal distributions of amplitudes (O'Connell, 1999a).
Anisotropy, $G^{A}{}_{kij}(\omega)$	Complicates shear-wave amplitudes and modifies radiation pattern amplitudes and can introduce frequency-dependent amplification based on direction of polarization.
Topography, $G^{T}{}_{kij}(\omega)$	Can produce amplification near topographic highs and introduces an additional sources of scattering.

Table 4: $\phi_{kij}(\omega)$ Propagation Phase Factors

Factor	Influence
Geometric spreading, $\phi^{r}{}_{kij}(\omega)$	Introduces frequency dependent propagation delays.
Large-scale velocity structure, $\phi^{V_{3D}}{}_{kij}(\omega)$	Horizontal and vertical velocity and density gradients and velocity and density discontinuities produce frequency dependent phase shifts.
Near-surface resonant responses, $\phi^{L}{}_{kij}(\omega)$	Interactions of shear-wave arrivals of varying angles of incidence and directions produce frequency dependent phase shifts.
Nonlinear soil responses, $\phi^{N}{}_{kij}(\omega)$	Depending on the dynamic soil properties and pore pressure responses, nonlinear responses can increase or reduce phase dispersion. In the case of coupled pore-pressure with dilatant materials can collapse phase producing intermittent amplification caustics.
Frequency independent attenuation, $\phi^{Q}{}_{kij}(\omega)$	Linear hysteretic behavior produces frequency-dependent velocity dispersion that produces frequency dependent phase variations.
Scattering, $\phi^{S}{}_{kij}(\omega)$	The scattering strength and scattering characteristics determine propagation distances required to randomize the phase of shear waves as a function of frequency.
Anisotropy, $\phi^{A}{}_{kij}(\omega)$	Complicates shear-wave polarizations and modifies radiation pattern polarizations.
Topography, $\phi^{T}{}_{kij}(\omega)$	Complicates phase as a function of topographic length scale and near-surface velocities.